Alma Mater Studiorum — Università di Bologna

Dipartimento di Fisica e Astronomia "Augusto Righi"
Laurea Magistrale in Fisica del Sistema Terra

Half-space solutions for deformation fields generated by thermo-poro-elastic inclusions with spherical symmetry

Presentata da:
Samuel Battolini

Relatore:
Prof.ssa Maria Elina Belardinelli

Correlatore:
Dott. Massimo Nespoli

Anno Accademico 2024 - 2025
Appello II

Sommario

Questa tesi si concentra su un modello di sorgente costituito da un'inclusione termo-poro-elastica (TPE) immersa in un mezzo elastico, omogeneo e limitato. Sono stati analizzati casi in cui la sorgente ha una geometria sferica o a guscio sferico, e subisce variazioni di temperatura e pressione di poro. Si forniscono soluzioni analitiche per le componenti di spostamento, deformazione e stress, sia all'interno della sorgente che nel mezzo circostante. Sono inoltre effettuati confronti con soluzioni preesistenti ottenute in un mezzo illimitato.

Lo studio mostra anche che gli effetti superficiali di una sorgente TPE a simmetria sferica sono, per una scelta adeguata dei parametri, equivalenti a quelli di una sorgente di Mogi. Questo tipo di soluzioni è rilevante per spiegare le deformazioni e la sismicità osservate in regioni geotermiche e vulcaniche, come alternativa ai modelli di sorgenti magmatiche. Per la sfera, le soluzioni sono completamente validate, mentre per il guscio sferico viene presentato un primo passo verso soluzioni complete. Il modello a guscio qui proposto risulta affidabile quando la sorgente si trova a una profondità paragonabile al suo diametro esterno, poiché l'errore nel soddisfare la condizione al contorno sulla sua superficie sferica interna rimane entro il 15%.

È stato analizzato il massimo sforzo di taglio sul piano mediano del guscio in funzione del raggio interno, mostrando che gusci più sottili presentano un massimo sforzo di taglio maggiore all'interno e minore all'esterno, con la conseguente possibilità di favorire la sismicità all'interno della sorgente. Il regime tettonico all'interno dell'inclusione risulta essere compressivo nel caso della sfera e trascorrente nel caso del guscio sferico.

Abstract

This thesis focuses on a source model consisting of a thermo-poro-elastic (TPE) inclusion embedded within a homogeneous, bounded elastic medium. I investigate cases where the source region has either a spherical or spherical shell geometry and undergoes variations in temperature and pore pressure. Analytical solutions are provided for displacement, strain, and stress components both within the source and in the surrounding medium. Comparisons are also made with pre-existing solutions obtained in an unbounded medium. The study also shows that the surface effects of a spherically symmetric TPE source are equivalent to those of a Mogi source for a suitable choice of parameters. This kind of solutions are relevant to explain deformation and seismicity observed in geothermal and volcanic regions, as alternatives to magmatic-source models.

For the sphere, the solutions are fully validated, while for the shell, an initial step toward complete solutions is presented. The present shell model proves reliable when the source lies at a depth comparable to its outer diameter, as the error in satisfying the boundary condition at the shell's inner surface remains within 15%.

The maximum shear stress on the shell's equatorial plane was analyzed as a function of the inner radius, showing that thinner shells have higher maximum shear stress inside and lower outside, potentially promoting seismicity within the source. The tectonic regime inside the source is compressive for the sphere and strike-slip for the shell.

Contents

Chapter 1

Introduction

Thermo-poro-elastic (TPE) inclusions represent deformation sources suitable to model deformation observed in volcanic and hydrothermal regions.
This chapter provides a general overview of the possible applications of the thermo-poro-elasticity theory, with a particular focus on volcanic regions, hence, the theoretical and methodological framework required to develop these results. In particular, the applicability of this theory to recent phenomena observed on Vulcano Island is summarized.
Subsequently, a portion of the TPE framework is presented, leading to the constitutive relation for TPE media and to Eshelby (1957) method, which allows for the solution of problems involving an inclusion of arbitrary shape undergoing inelastic transformations within an elastic space.
The main objective of this thesis is to extend the model proposed by Belardinelli et al. (2019) for TPE inclusions with spherical symmetry to include the presence of a free surface resembling the Earth surface. For this reason, the analytical solutions developed by Belardinelli et al. (2019) are presented at the end of this chapter, as they will serve as the theoretical foundation for the present work.
The other parts of the thesis are briefly described as follows:

- Chapter 2 presents the methodology used to derive the analytical solutions for the displacement, strain, and stress fields discussed previously, together with their explicit expressions. These solutions are obtained by following the method adopted by Bonafede (1990) for a spherical magmatic chamber (i.e., a Mogi source), which full-space solutions were originally derived by Mogi (1958). In particular, the employed methods include the image source technique and the approach described in section (2.1). I also present the equivalence of the TPE sources here considered with a Mogi source, for a suitable parameter choice, as far as deformation fields at the free surface are concerned.

- Chapter 3 presents the results obtained in chapter 2 through color maps of each field component on vertical sections for two configurations: one where the source center is closer to the free surface, and another where it is positioned farther away. To highlight the differences caused by the presence of the free surface, the difference between the solutions for the bounded and unbounded media is also shown. Furthermore, the field components and the maximum shear stress are visualized both in the median plane and at the surface. Finally, tectonic regime considerations are discussed based on the deviatoric stress state observed in the median plane and at the surface.

- Chapter 4 discusses the main results expressed in previous chapters and examines how the maximum shear stress generated by the shell varies with its inner radius. While the solutions obtained for the spherical TPE source are exacts, a notable challenge encountered with the shell inclusion concerns the boundary condition requiring continuity of the radial stress component across the internal spherical surface. This chapter provides a quantitative analysis of the magnitude of the boundary condition error (compared to the correct value) along the median plane and the axis of the shell. To address this error, corrections similar to those proposed by McTigue (1986) for a Mogi source would be appropriate. Therefore, the work presented in this thesis represents a preliminary step toward obtaining fully consistent analytical solutions.
  Finally, possible applications and future developments are discussed.

- Chapter 5 summarizes the work carried out and the results obtained throughout the thesis. It also includes some concluding remarks.

- The appendix contains the procedure for converting a vector or tensor from spherical to cylindrical coordinates (and vice versa), the displacement and stress components derived by Belardinelli et al. (2019) expressed in cylindrical coordinates, the complete calculations leading to the solutions presented in chapter 2, and a series of plots auxiliary to the discussion presented in chapter 4.

1.1 Applications of thermo-poro-elasticity theory

Fluids are naturally present throughout the Earth's crust, from the shallow subsurface to several kilometers of depth. Their presence significantly influences the mechanical behavior of rocks, challenging the view of the crust as a purely elastic medium. The interaction between fluids and the solid matrix, governed by pore pressure, modifies stress distribution, deformation, and, in some cases, seismic activity. To capture these effects, poro-elasticity theory provides a framework that incorporates the influence of fluid pressure within porous rocks. When temperature differences between fluids and the surrounding medium are significant, poro-elasticity extends to thermo-poro-elasticity, accounting for thermal expansion and additional coupling mechanisms. Understanding the role of fluids in geophysical processes requires an interdisciplinary approach, combining observational data, analytical models, and numerical simulations. As summarized by Nespoli et al. (2025), the Earth's crust contains a variety of fluids, primarily water, carbon dioxide (CO_2), and hydrocarbons such as methane (CH_4) (Fyfe, 2012). Water (H_2O), the most abundant, originates mainly from atmospheric sources and infiltrates the crust through recharge processes. It accumulates in permeable rock layers, forming aquifers that serve as crucial groundwater reservoirs (Wang and Manga, 2021). Recharge can occur via direct infiltration from the surface or through lateral water flow from mountain regions (Markovich et al., 2019). However, water is not confined to shallow depths, subduction processes transport it deep into the mantle, potentially reaching the core-mantle boundary (Karato et al., 2020; Walter, 2021). CO_2 in the crust mainly originates from metamorphic processes and mantle degassing, with volcanic and hydrothermal systems acting as major emission sources (Chiodini et al., 2021; Piombo et al., 2005). Magmatic reservoirs store volatile components, including water (H_2O), carbon dioxide (CO_2), hydrogen disulfide (H_2S), sulphur dioxide

(SO_2), halogen compounds (HCl, HF), and trace of other elements (Edmonds and Woods, 2018). Methane, predominantly of biogenic origin, forms through bacterial or thermogenic degradation of organic matter (Schoell, 1988). These fluids not only participate in natural geological cycles, but also play a central role in anthropogenic activities such as energy extraction and carbon storage.
The role of thermo-poro-elasticity is widely acknowledged as critical in understanding seismic events triggered by anthropogenic activities. A notable example is geothermal exploitation, where the presence of both permeable and fractured rock formations allows for the extraction of heat from hot underground fluids. In many geo-technical applications, processes such as fluid injection or extraction take place in soft, permeable reservoirs that are susceptible to significant deformation, whether through compaction during production or uplift during injection. These deformations, coupled with changes in pore pressure, may alter the stress field contributing to fault failure.
Fluid-earthquake interaction effects are typically categorized into static and dynamic mechanisms (e.g., Rice and Cleary 1976; Manga and Wang 2015). Static mechanisms are generally dominant in regions close to the earthquake source, within approximately one fault length (near field), while dynamic mechanisms are invoked to explain far field effects. Static effects are associated with permanent modifications to the surrounding deformation field, caused by the earthquake. These can be approximated by modeling static dislocations within an elastic half-space framework. During the coseismic phase, which often occurs under undrained conditions, static stress changes can raise pore pressure, potentially reducing the effective normal stress on a nearby fault and facilitating slip. Nevertheless, this increase in pore pressure can be mitigated by dilatancy, as fault movement might generate additional fractures, promoting fluid flow and thereby decreasing pore pressure. In contrast, dynamic effects arise from the transient passage of seismic waves, inducing short-lived variations in stress and strain. These wave-induced disturbances can cause abrupt pore pressure fluctuations, possibly triggering fault slip earlier than static stress models would predict. Although such effects are often temporary and poro-elastic in nature, they may still result in irreversible alterations in porosity and permeability, significantly impacting the hydro-mechanical properties of the medium. Observable manifestations of dynamic effects include shifts in groundwater levels, fluctuations in stream discharge, changes in water temperature, and occurrences of soil liquefaction. The lack of detailed descriptions of fault zones in many studies makes it challenging to precisely determine the mechanical impacts involved.
Volcanic regions demand the development of models to represent the mechanical effects induced by hot and pressurized fluids within the Earth's crust, and this work will primarily focus on this topic.

1.1.1 Volcanic regions and TPE inclusion model

Hydrothermal systems are dynamic environments resulting from igneous activity at depth, typically linked to the presence of a magma reservoir or a crystallizing intrusion. These systems are often classified as expressions of secondary volcanism, as the fluids involved can either be derived from magmatic degassing or from external sources such as meteoric groundwater, which infiltrates the surrounding rocks and becomes heated in proximity to the intrusive body.
The interaction between hot, pressurized fluids and the surrounding rock occurs through a network of fractures, faults, and porous zones, often leading to increased permeability

in certain regions, while others remain sealed by impermeable layers. This heterogeneous structure allows for a variety of phenomena to develop over relatively short timescales, many of which are observable at the surface in the form of gas emissions, hydrothermal alterations, or ground deformation. Hydrothermal regions are widespread, occurring both in continental and oceanic settings. In several cases, they are associated with large volcanic depressions such as calderas, which are typically formed by the collapse of a magma chamber following major eruptive episodes. Calderas are among the most hazardous volcanic environments on Earth, capable of producing highly explosive eruptions with potentially global consequences. From a geophysical perspective, these regions represent key areas for the study and application of fluid diffusion models within the Earth's crust. Volcanic regions often show deformation patterns that may reflect the interplay between magmatic activity and hydrothermal circulation. Traditional models describe such deformation using elastic representations of magma-filled sources (e.g., dikes, sills, reservoirs), while more recent approaches incorporate the effects of temperature and pore pressure variations through TPE formulations (e.g., Rinaldi et al. 2010; Todesco 2021). The recent development of TPE inclusion models allows such effects to be modeled using analytical or semi-analytical formulations that are sufficiently fast and accurate to be employed in real-time applications or in data inversion processes, enabling the simultaneous modeling of stress (and thus seismicity), displacement, and deformation.

TPE inclusion models allow us to simulate the mechanical effects induced by the arrival of hot and pressurized fluids, even in the absence of new magma emplacement. This modeling framework is particularly useful for interpreting episodes of volcanic unrest, during which increased seismicity, gas emissions, or ground deformation may occur. Accurately capturing the role of hydrothermal processes is essential not only for advancing the scientific understanding of these systems but also for improving volcanic hazard assessment and early warning capabilities. Although many geothermal areas are located in volcanic systems that have remained dormant for millennia or are considered extinct, they still pose potential risks to nearby populations. The development of robust and realistic models that include hydrothermal dynamics is therefore a key objective in both scientific research and risk mitigation efforts related to volcanic environments.

The inclusion method introduced by Eshelby (1957), described in section (1.3.1), is the starting point for modeling the mechanical response of a finite region, commonly referred to as an inclusion, undergoing changes in temperature and pore pressure, while embedded in an elastic medium. This approach has been extensively adopted in the literature, particularly in the context of geothermal reservoir deformation and the assessment of induced seismicity (Segall, 1992). Following the foundational studies by Segall and Fitzgerald (1998), TPE inclusions have proved effective in explaining the variety of fault mechanisms observed in hydrocarbon extraction zones. Initially developed for geothermal contexts involving anthropogenic fluid injection and withdrawal, they have since been applied to model stress and deformation in volcanic regions where such variations arise instead from the natural exsolution of magmatic volatiles (Belardinelli et al., 2019).

Physically, hydrothermal areas are characterized by mass and energy transport driven by the convection of heated fluids. These processes are commonly triggered by the emplacement of shallow magmatic intrusions, which release volatiles, especially water and carbon dioxide, into the surrounding porous rocks, resulting in increases in temperature (T) and pore pressure (p) (Belardinelli et al., 2019). The TPE inclusion

model captures such phenomena by representing a limited porous and permeable region where T and p variations occur (highlighted in yellow in Fig. 1.1), enclosed in a poro-elastic matrix assumed to be isothermal and drained (gray area). The degassing magmatic source (orange area) acts as the driver of these changes. According to the constitutive equations and physical laws of thermo-poro-elasticity, one can calculate the displacement, strain, and stress induced in the surrounding medium by the TPE inclusion, which thus behaves as a deformation source, contributing to the observed deformation field together with the magmatic source.

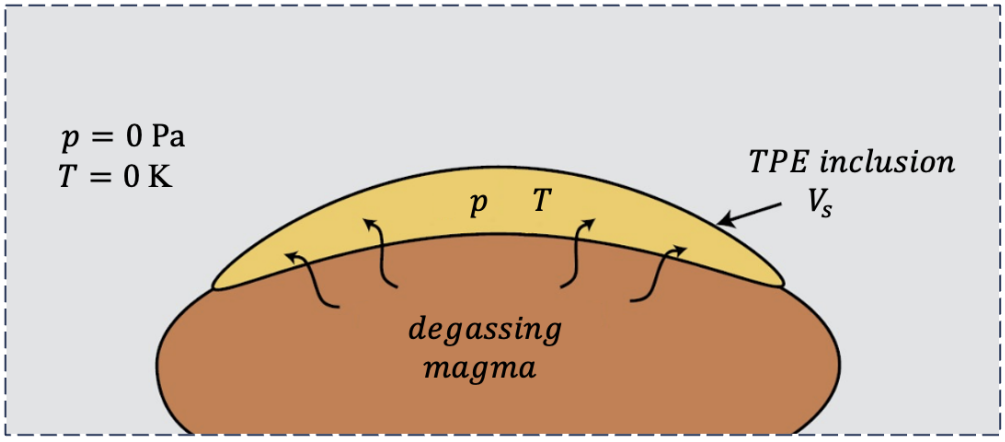

Figure 1.1: *Conceptual model, modified from Belardinelli et al. (2019), of the Thermo-Poro-Elastic source (yellow), surrounded by an embedding matrix (gray) in isothermal and undrained conditions, subject to changes in pore pressure, p, and temperature, T. In orange, a hypothetical deeper magma chamber is shown, from which the fluids originate.*

The theoretical framework underpinning TPE inclusion models is the linear theory of thermo-poro-elasticity (McTigue, 1986), which has been employed to derive both analytical and semi-analytical solutions. These include spherical and spherical shell inclusions (Belardinelli et al., 2019), thin disk geometries (Mantiloni et al., 2020), and thick cylindrical inclusions obtained by the stacking of two or more thin disks (Nespoli et al., 2021). The numerical code EFGRN/EFCMP (Nespoli et al., 2022) allows for the incorporation of geometric complexity, non-uniform distributions of pressure and temperature, and vertically stratified elastic properties.
In particular, unlike pressurized magma chamber models that typically neglect internal shear stress, TPE inclusions can produce significant deviatoric stress fields even within them (Nespoli et al., 2023a). This makes them suitable to explain seismicity occurring within the inclusion itself, even in volcanic systems lacking clear evidence of shallow magmatic bodies (Nespoli et al., 2021). To model transient effects induced by the fluid flow inside a TPE inclusion, analytical solutions were proposed by Belardinelli et al. (2022), Nespoli et al. (2021) and Nespoli et al. (2023b).
Recent applications of TPE inclusion models include the persistent deformation observed at Campi Flegrei. Uplift up to 1.8 m was recorded between 1982 and 1984, followed by a two-decade period of subsidence, and again uplift since 2005. Uplift episodes correlate with increased seismicity and fumarolic activity (Del Gaudio et al., 2010; Tramelli et al., 2021). Disk-shaped TPE models were shown to reproduce both the surface displacement patterns and the spatial-temporal evolution of seismicity during these episodes (Mantiloni

et al., 2020; Nespoli et al., 2021).
A similar modeling strategy was also applied at Vulcano Island, where spherical and cylindrical TPE sources were used to reproduce the inflation pattern observed in 2021 (Stissi et al., 2023).

1.1.2 Thermo-poro-elastic deformations at Vulcano Island during the 2021 unrest

Vulcano Island, the southernmost of the Aeolian Islands, is a small but active volcanic edifice with a surface area of approximately 21 km^2 (Selva et al., 2020). Despite its limited size and low number of permanent residents, it experiences a significant seasonal increase in population due to its popularity as a tourist destination, mainly related to volcanic features such as fumaroles and thermal muds (Galderisi et al., 2013). The last eruption occurred between 1888 and 1890 and led to the definition of the "Vulcanian" eruptive style.
Since then, the island has shown persistent fumarolic activity, primarily along major structural alignments (Selva et al., 2020). Several episodes of volcanic unrest have been recorded, particularly during the 1970s, 1990s, and 2000s. These phases were characterized by increased fumarole temperatures, expansion of degassing zones, and a rise in local seismicity, although without significant ground deformation or tectonic activity.
The observed phenomena are associated with an active hydrothermal system located beneath the La Fossa caldera, where fluid circulation occurs between 500 and 1500 meters below sea level. This interpretation is supported by both geophysical and geochemical investigations (Stissi et al., 2023). Although no eruptive activity has taken place in recent decades, the combination of persistent surface manifestations, the presence of residential areas, and high tourist exposure contributes to a significant volcanic risk (Galderisi et al., 2013).
The most recent unrest episode began in September 2021 and was characterized by an anomalous increase in gas emissions. Carbon dioxide fluxes reached values up to 34,000 $g \cdot m^{-2} \cdot day^{-1}$, approximately twenty times higher than average values measured in previous decades, and sulfur dioxide emissions peaked at 2.7 kg/s, which is one order of magnitude greater than the mean value of the previous thirteen years (Aiuppa et al., 2022; Inguaggiato et al., 2022). The persistence of such anomalies suggests the possibility of escalating hazard levels, particularly concerning the occurrence of phreatic explosions, which are among the most hazardous events in volcanic systems with active shallow hydrothermal circulation (Barbano et al., 2017; Kobayashi et al., 2018; Selva et al., 2020).
Stissi et al. (2023) inverted data measured by GPS monitoring stations, by combining the thermo-poro-elastic equations with a genetic algorithm. The steady radial expansion of the volcanic edifice, observed until mid-October 2021 and most prominent at stations near the summit crater with displacement rapidly decreasing with distance, points to a shallow deformation source. The geometry of both horizontal and vertical ground movements is consistent with an almost isotropic deformation source, which could be associated with either a pressurized spherical magmatic body (as described by the Mogi model) or with deformation related to thermo-poro-elastic processes. According to Stissi et al. (2023), it appears more plausible that the observed deformation is primarily driven by thermo-poro-elastic effects rather than by the emplacement or pressurization

of a shallow magmatic intrusion.
Stissi et al. (2023) suggested that a spherical source could represent a confined zone within the porous medium where local variations in porosity or permeability hinder fluid migration, resulting in an increase in pore pressure. However, a vertically extended cylindrical source, approximately 1 km in height, may reflect the pressurization of a narrow fluid pathway connecting deeper regions of the hydrothermal system to the surface. They came to the conclusion that, due to the similarly good fit of both geometries to the observed deformation data, it is not possible to definitively prefer one model over the other. This is also because the available data come from only a few GPS stations, which is not sufficient to justify the choice of one source geometry over another. The resulting increase in pore pressure may vary between 0.01 and 7 MPa. The deformation source is located at an approximate depth of 800 m from the surface, which falls within the depth range between 0 and 1.5 km below sea level, commonly associated with the hydrothermal system as proposed in earlier investigations.

1.2 Constitutive relation of a thermo-poro-elastic medium

1.2.1 Strain Tensor

In continuum mechanics, bodies are considered deformable: the distances between their volume elements are not fixed. To describe the position of a body at a given time t, it is necessary to know the coordinates of each point. Considering a material point initially at position $\mathbf{x} = (x_1, x_2, x_3)$ at time $t = 0$, which undergoes a displacement $\mathbf{u}(\mathbf{x}, t) = (u_1, u_2, u_3)$, its final position is $\mathbf{x} + \mathbf{u}$.
The vector $\mathbf{u}(\mathbf{x}, t)$ is defined as the "*displacement vector*", which represents the movement of the point over time. It is a continuous and differentiable function of spatial and temporal coordinates in the absence of dislocations.
Now, let us consider another material point initially located at $\mathbf{x} + d\mathbf{x}$, meaning that it is close to the first one. At time t, when deformation occurs, this point is displaced by the vector $\mathbf{u}(\mathbf{x} + d\mathbf{x}, t) = \mathbf{u}(\mathbf{x}, t) + d\mathbf{u}(\mathbf{x}, t)$, where $d\mathbf{u}(\mathbf{x}, t)$ has components expressible using Einstein notation:

$$\frac{\partial u_i}{\partial x_j} dx_j. \tag{1.1}$$

Taking into account the initial distance ds_0 at time $t = 0$ and the distance ds at time t, we obtain:

$$ds_0^2 = dx_i dx_i, \tag{1.2}$$

whereas at time t:

$$ds^2 = (dx_i + du_i)(dx_i + du_i) \simeq dx_i dx_i + 2\frac{\partial u_i}{\partial x_j} dx_i dx_j, \tag{1.3}$$

where second-order terms are neglected by assuming small deformations ($|d\mathbf{u}| \ll |d\mathbf{x}|$). Thus, we obtain the following:

$$ds^2 - ds_0^2 \simeq 2\frac{\partial u_i}{\partial x_j} dx_i dx_j. \tag{1.4}$$

The displacement gradient $\frac{\partial u_i}{\partial x_j}$, being a second-rank tensor, can be decomposed into a symmetric and an antisymmetric part:

$$\frac{\partial u_i}{\partial x_j} = \frac{1}{2}\left(\frac{\partial u_i}{\partial x_j} + \frac{\partial u_j}{\partial x_i}\right) + \frac{1}{2}\left(\frac{\partial u_i}{\partial x_j} - \frac{\partial u_j}{\partial x_i}\right). \tag{1.5}$$

Contracting with $dx_i dx_j$ in eq. (1.4), the antisymmetric component is eliminated, leading to $ds^2 - ds_0^2 \simeq 2\epsilon_{ij} dx_i dx_j$, where

$$\epsilon_{ij} \doteq \frac{1}{2}\left(\frac{\partial u_i}{\partial x_j} + \frac{\partial u_j}{\partial x_i}\right) \tag{1.6}$$

is called the "*infinitesimal strain tensor*".
This tensor is symmetric, which means its matrix representation with respect to any basis admits three real eigenvalues, known as the "*principal strain values*", and an orthonormal basis of eigenvectors, called the "*principal strain axis*".
A first-order approximation of the relative change in distance between two points can be determined as:

$$\frac{ds - ds_0}{ds_0} = \epsilon_{ij} \frac{dx_i}{ds_0} \frac{dx_j}{ds_0}. \tag{1.7}$$

The diagonal components of ϵ_{ij} represent the relative change in length of a vector aligned with a Cartesian axis. A negative component value corresponds to a contraction, while a positive value corresponds to an elongation.
The trace ϵ_{kk}, corresponding to the divergence of the displacement vector $\mathbf{u}(\mathbf{x}, t)$, represents the relative volume change of an infinitesimal volume V_0 of the body:

$$\epsilon_{kk} = \frac{\partial u_k}{\partial x_k} = \nabla \cdot \mathbf{u} = \frac{\delta V}{V_0}. \tag{1.8}$$

The infinitesimal strain tensor can be decomposed into a component whose elements are equal to the mean of the diagonal elements, known as the "*isotropic*" component, which describes the relative volume change, and a component that describes shape change at constant volume, known as the "*deviatoric*" component.
The isotropic component is given by:

$$\epsilon_{ij}^0 = \frac{1}{3}\epsilon_{kk}\delta_{ij}, \tag{1.9}$$

whereas the deviatoric component is:

$$\epsilon'_{ij} = \epsilon_{ij} - \frac{1}{3}\epsilon_{kk}\delta_{ij}. \tag{1.10}$$

1.2.2 Stress Tensor

To define the concept of traction, it is necessary to consider a body characterized by a certain spatial configuration at a given time t. Within this body, one can imagine a closed surface S, on which a small portion ΔS can be considered. Thanks to the direction of the unit normal vector $\hat{\mathbf{n}}$, it is possible to distinguish a "positive" face, facing the normal,

and a "negative" one. The material adjacent to the positive face exerts a force $\Delta\mathbf{F}$ on the material adjacent to the negative face, and this force depends on the position, orientation, and area of the surface. We assume that the ratio between $\Delta\mathbf{F}$ and ΔS tends to a finite limit $\frac{d\mathbf{F}}{dS}$ as ΔS approaches zero, and that the moment of the forces on ΔS is zero (Euler and Cauchy's principle). The limiting vector is called "*traction*" and is defined as follows:

$$\mathbf{T}(\hat{\mathbf{n}}, \mathbf{x}, t) \doteq \frac{d\mathbf{F}}{dS}(\hat{\mathbf{n}}, \mathbf{x}, t), \tag{1.11}$$

where $\mathbf{x}$ represents the point to which ΔS tends and t is the time.
Considering a Cartesian coordinate system with an orthonormal basis ($\mathbf{e}^{(1)}$, $\mathbf{e}^{(2)}$, $\mathbf{e}^{(3)}$), and a surface dS_i with a normal vector $\mathbf{e}^{(i)}$ directed along the positive semi-axis of x_i ($i = 1, 2, 3$), the component along the x_j axis ($j = 1, 2, 3$) of the traction acting on the surface dS_i is called "*stress*" and is defined as follows:

$$\tau_{ij} \doteq \mathbf{T}(\mathbf{e}_i) \cdot \mathbf{e}_j. \tag{1.12}$$

The diagonal components of the tensor are called "*normal stresses*", as they act perpendicularly to the plane, while the other elements are called "*shear stresses*", acting tangentially to the plane.
Knowing the components τ_{ij}, the traction $T_i(\hat{\mathbf{n}})$ on a generic surface dS with normal $\hat{\mathbf{n}}$ is given by "*Cauchy's Formula*":

$$T_i(\hat{\mathbf{n}}) = \tau_{ji} n_j. \tag{1.13}$$

The stress tensor is symmetric; therefore, its matrix representation in any basis has three real eigenvalues, called "*principal stress values*", and an orthonormal basis of eigenvectors, called "*principal stress axis*". The principal axis define three planes, called "*principal planes*", where only normal stresses are present. This tensor can be decomposed into an "*isotropic*" component, which has elements equal to the average of the diagonal elements, and a "*deviatoric*" component. The isotropic component is:

$$\tau^0_{ij} \doteq \frac{1}{3}\tau_{kk}\delta_{ij}, \tag{1.14}$$

while the deviatoric component is:

$$\tau'_{ij} \doteq \tau_{ij} - \frac{1}{3}\tau_{kk}\delta_{ij}. \tag{1.15}$$

The isotropic component generates normal tractions on the application surface, with a constant magnitude regardless of its orientation:

$$T_i(\hat{\mathbf{n}}) = \tau^0_{ij} n_j = \frac{1}{3}\tau_{kk}\delta_{ij} n_j = \frac{1}{3}\tau_{kk} n_i. \tag{1.16}$$

Thus, a "*mean pressure*" can be defined as the negative of the average of the normal stresses:

$$\bar{p} \doteq -\frac{1}{3}\tau_{kk}. \tag{1.17}$$

From eq. (1.15), it follows that the trace of the deviatoric stress τ'_{ij} is zero. Eq. (1.14) shows that the isotropic stress is a multiple of the identity tensor and is therefore diagonal in any reference system. These facts imply that the principal axis of τ_{ij} coincide with

those of τ'_{ij}, while the eigenvalues of the deviatoric stress σ'_1, σ'_2, and σ'_3 differ from those of τ_{ij} by an additive scalar term $\frac{1}{3}\tau_{kk}$. The deviatoric stress components are important because they can give us information about the stress regime. In particular, if $\sigma'_1 \leq \sigma'_2 \leq \sigma'_3$, then $\sigma'_1 \leq 0$ and $\sigma'_3 \geq 0$, which means that σ'_1 is the most compressive deviatoric stress and σ'_3 is the most tensile deviatoric stress. In general, motion along a fracture surface in the depths of the lithosphere is tangential to the surface itself. Therefore, the stresses that generate such motion must be shear stresses. In the Earth's lithosphere, tectonic movements produce stresses that increase over time, particularly concentrated along plate boundaries. Based on equilibrium considerations, we expect the one principal axis of the deviatoric stress is vertical and the basic classification of the different tectonic regimes in the Earth's crust:

- **extensional regime**: $\tau'_{33} = \sigma'_1$, where the vertical axis corresponds to the compressive deviatoric stress. At least one horizontal direction experiences a positive deviatoric stress (i.e., a principal stress smaller in absolute value than the mean pressure). Normal faults are typical of this setting;
- **compressional regime**: $\tau'_{33} = \sigma'_3$, where the vertical axis corresponds to the tensile deviatoric stress. At least one horizontal direction experiences a negative deviatoric stress (i.e., a principal stress greater in absolute value than the mean pressure). Reverse (or thrust) faults are typical of this setting;
- **strike-slip regime**: $\tau'_{33} = \sigma'_2$, where the vertical axis corresponds to the intermediate stress. In the principal horizontal directions, one deviatoric stress is negative and the other is positive; hence, one principal horizontal stress is greater and the other is smaller (in absolute value) than the mean pressure. Strike-slip faults are typical of this setting.

The minimum and maximum normal stresses are applied to the principal surfaces relative to the minimum σ_{min} and maximum σ_{max} eigenvalues, and on each principal surface, the shear tractions are zero. The surfaces where maximum shear stresses are present are thus intermediate between the principal surfaces. The plane on which the maximum shear traction acts forms a 45° angle between the minimum and maximum principal axis and contains the intermediate axis. The magnitude of this traction is:

$$S_{\max} = \frac{1}{2}\left(\sigma_{max} - \sigma_{min}\right). \tag{1.18}$$

The analysis of the maximum shear stress is crucial for understanding earthquake generation. Indeed, it allows to identify the planes most susceptible to failure. The "*Coulomb failure criterion*" is a fundamental law used to describe the conditions under which rocks or materials fail (fracture or slip) due to applied stress. It is especially important in earthquake mechanics, faulting, and rock mechanics. The law states that failure occurs when the absolute value of the shear stress $|\tau|$ on a potential failure plane exceeds a critical value, which depends on the normal stress acting on that plane σ_n and the material's properties (friction f and cohesion C):

$$|\tau| \geq -f\sigma_n + C. \tag{1.19}$$

At this point, it is important to state that the axis x_1, x_2, and x_3 mentioned in this chapter will sometimes be denoted as x, y, and z, respectively, to simplify the notation.

1.2.3 Constitutive Relation for elastic media

The term "*constitutive relation*" refers to a relation that provides the stress components as a function of other variables characterizing a system. In general, the stress tensor τ_{ij} depends on the strain tensor ϵ_{ij} and its time derivatives $\dot{\epsilon_{ij}}$, so a general constitutive relation is:

$$F(\epsilon_{ij}, \dot{\epsilon_{ij}}, \tau_{ij}, \dot{\tau_{ij}}) = 0. \tag{1.20}$$

For an elastic material, τ_{ij} depends only on ϵ_{ij} through a one-to-one relation, expressible via the "*generalized Hooke's law*":

$$\tau_{ij} = C_{ijkl}\epsilon_{kl}, \tag{1.21}$$

where C_{ijkl} is a fourth-rank tensor representing the elastic constants of the material. In the case of a linear, isotropic elastic material, its constitutive relation can be written through a proportionality relation between stress and isotropic strain and between stress and deviatoric strain, given by:

$$\frac{1}{3}\tau_{kk} = K\epsilon_{kk}, \quad \tau'_{ij} = 2\mu\epsilon'_{ij}. \tag{1.22}$$

In the previous equation, K is the "*bulk modulus*", and μ is called "*shear modulus*", which can be measured in a shear deformation experiment where the only nonzero stress tensor components are $\tau_{12} = \tau_{21}$. In this case, we have $\mu = \frac{\tau_{12}}{2\epsilon_{12}}$.
Using eqq. (1.22), (1.10), and (1.15), the constitutive relation and its inverse can be derived, respectively expressed as:

$$\tau_{ij} = \lambda\epsilon_{kk}\delta_{ij} + 2\mu\epsilon_{ij}, \quad \epsilon_{ij} = \frac{1}{2\mu}\left(\tau_{ij} - \frac{\lambda}{3\lambda + 2\mu}\tau_{kk}\delta_{ij}\right), \tag{1.23}$$

where $\lambda \doteq K - \frac{2}{3}\mu$. The parameters λ and μ are called "*Lamé constants*".
The constitutive relation can also be expressed in terms of the shear modulus and "*Poisson's ratio*", denoted by ν and defined as the ratio between transverse contraction and longitudinal extension following the application of a uniaxial stress state (at constant temperature). If x_1 is the traction direction and x_2 is an orthogonal direction, we have $\nu = -\frac{\epsilon_{22}}{\epsilon_{11}}$. Since the only nonzero component of τ_{ij} is τ_{11}, using the inverse constitutive relation from eq. (1.23) and the definition of ν, we obtain $\nu = \frac{\lambda}{2(\lambda+\mu)}$. Substituting this relation into eq. (1.23), we obtain an expression for the inverse constitutive relation in terms of μ and ν:

$$\epsilon_{ij} = \frac{1}{2\mu}\left(\tau_{ij} - \frac{\nu}{1+\nu}\tau_{kk}\delta_{ij}\right). \tag{1.24}$$

1.2.4 Constitutive Relation of a TPE medium

A poro-elastic medium is a material composed of a solid "matrix" (or "frame") with elastic behavior, containing interconnected cavities, known as "pores", filled with fluid. Such a medium is described in terms of pointwise-defined properties, which are referred to a representative "*elementary volume*": a volume element small enough for the properties to be considered constant within it, yet large enough compared to the size of the pores, grains, or solid matrix components to ensure that these properties vary smoothly in space and satisfy continuity requirements. Some quantities used to describe a porous medium are as follows:

- the "porosity" Φ, defined as the volume of empty space per unit volume of the medium. It can refer to all types of pores, called "total porosity", or it may refer only to pores that can transfer fluid between them, in which case it is called "effective porosity";
- the "fluid quantity" v_i, defined as the volume of the i-th type of fluid contained within the pores per unit volume of the material. If only one type of fluid is present, this quantity coincides with the porosity;
- the "pore pressure" p, defined as the pressure of the fluid filling the pores. This quantity can be considered uniform within the elementary volume, assuming that the fluid flows sufficiently slowly through the pores or that the volume is sufficiently small;
- the "confining pressure" P_C, defined when a stress state is applied to the porous medium and coincides with the isotropic component of the stress tensor, hence $P_C \doteq -\frac{1}{3}\tau_{kk}$.

It is assumed that the poro-elastic medium is isotropic and that the deformations from one equilibrium state to another are reversible. The constitutive relation for a poro-elastic medium was described in the works of Biot (1941) and Rice and Cleary (1976), where a cubic-shaped element is considered. The volume of this element is assumed to have dimensions pertinent to the elementary volume of the poroelastic material. If we consider that the element undergoes reversible deformations, the macroscopic variables $\epsilon_{ij}, \tau_{ij}, p, v$ must be state functions. Given these assumptions, suppose the element is initially in an equilibrium state, described by the variables $\epsilon^0_{ij}, \tau^0_{ij}, p_0, v_0$, and since there is no deformation initially, we have $\epsilon^0_{ij} = 0$. After the deformation process, a change in these quantities can be expressed as $\Delta\epsilon_{ij} \doteq \epsilon_{ij}$, $\Delta\tau_{ij} \doteq \tau_{ij}$, $\Delta p \doteq p$, $\Delta v \doteq v$, where the equalities marked with '$\doteq$' are used for notational convenience.

Constant Pore Pressure (Drained Conditions)

If the medium is subjected only to external pressure, no variation in the pore pressure would occur, so $p = 0$. In this case, the constitutive relation is given by eq. (1.24), since the material is purely elastic. In this type of transformation, the fluid quantity must vary in such a way that the pore pressure remains constant, so a linear relation between v and τ_{ij} is assumed:

$$v = a_{ij}\tau_{ij}, \tag{1.25}$$

where $a_{ij} \doteq a\delta_{ij}$ is an isotropic rank-2 tensor. We define the quantity $H_1 \doteq \frac{1}{3a}$, so that:

$$v = \frac{1}{3H_1}\tau_{kk} = -\frac{1}{H_1}P_C. \tag{1.26}$$

H_1 represents the reciprocal of the fluid volume that flows out from a unit volume of material per unit confining pressure applied to the surface of the medium while the pore pressure remains constant.

Constant Stress

Consider the case where the medium is not subjected to any additional stress at the surface, and thus $\tau_{ij} = 0$, and suppose it is surrounded by an impermeable, flexible membrane completely sealed except for a tube through which fluid flows inward. As long as the material is free to expand, the injection of new fluid causes a change in volume v and pressure p. In this case, we expect the deformation to be:

$$\epsilon_{ij} = b_{ij}p = \frac{1}{3H_2}p\delta_{ij}, \tag{1.27}$$

where b_{ij} is an isotropic rank-2 tensor, and H_2 is the "Biot constant", which represents the reciprocal of the volume change per unit volume for a unit pore pressure increment while the stresses remain constant. The relation between p and v is also linear:

$$v = \frac{1}{R}p, \tag{1.28}$$

where $\frac{1}{R}$ represents the volume increment of fluid in the pores per unit material volume for an increment of p; R has the dimensions of stress.

Constitutive Equations

Consider the case of a general thermo-poro-elastic transformation, where both the stress and the pore pressure vary. The process can be divided into two distinct transformations: the first involves the application of stress at constant pressure ($p = 0$), and the second involves a variation in pressure at constant stress ($\tau_{ij} = 0$). Using eqq. (1.24) and (1.27), we obtain an expression for the deformation:

$$\epsilon_{ij} = \frac{1}{2\mu}\left(\tau_{ij} - \frac{\nu}{1+\nu}\tau_{kk}\delta_{ij}\right) + \frac{1}{3H_2}p\delta_{ij}. \tag{1.29}$$

Using eqq. (1.26) and (1.27), we obtain an equation for the fluid quantity:

$$v = \frac{1}{3H_1}\tau_{kk} + \frac{1}{R}p, \tag{1.30}$$

and it can be shown that $H_1 = H_2 = H$ (Biot, 1941). The constant H can be determined from the incompressibility K of the poro-elastic medium under drained and isothermal conditions, and K_s', which can be interpreted as the incompressibility of the solid phase (Wang and Manga, 2021):

$$\frac{1}{H} = \frac{1}{K} - \frac{1}{K_s'}. \tag{1.31}$$

The eq. (1.29) can be generalized for the case of a thermo-poro-elastic medium, where both temperature T and pore pressure p change:

$$\epsilon_{ij} = \frac{1}{2\mu}\left(\tau_{ij} - \frac{\nu}{1+\nu}\tau_{kk}\delta_{ij}\right) + \frac{1}{3H}p\delta_{ij} + \frac{1}{3}\alpha T\delta_{ij}, \tag{1.32}$$

where α is the "thermal expansion coefficient". It is also possible to derive the inverse constitutive relation of eq. (1.32):

$$\tau_{ij} = 2\mu\epsilon_{ij} + \lambda\epsilon_{kk}\delta_{ij} - K\left(\frac{1}{H}p\delta_{ij} + \alpha T\delta_{ij}\right). \tag{1.33}$$

The eq. (1.32) can be rewritten using the "stress-free strain tensor" $\epsilon_0\delta_{ij}$, which is an isotropic tensor representing the strain produced by p and T in the absence of stress:

$$\epsilon_{ij} = \frac{1}{2\mu}\left(\tau_{ij} - \frac{\nu}{1+\nu}\tau_{kk}\delta_{ij}\right) + \epsilon_0\delta_{ij}, \tag{1.34}$$

so that:

$$\epsilon_0\delta_{ij} \doteq \left(\frac{1}{3H}p + \frac{1}{3}\alpha T\right)\delta_{ij}. \tag{1.35}$$

It can be observed that ϵ_0 (also called "potency") depends linearly on the variations of pressure and temperature. It is possible to observe that eq. (1.34) reduces to eq. (1.24) in the case where temperature and pressure changes are zero. Hence, in isothermal and drained conditions, the TPE medium is equivalent to an elastic medium.

Undrained Conditions

"Undrained deformations" refer to processes that occur on a timescale too short to allow the gain or loss of pore fluid mass in a material element through diffusive transport from or to nearby elements. Under these conditions, the variation in fluid mass per unit volume of material is zero. Applying a stress τ_{ij} to the material in a short time generates a pressure:

$$p = -\frac{B}{3}\tau_{kk}, \tag{1.36}$$

where B is the "Skempton parameter". Under these conditions, since the pressure can be expressed through the Skempton parameter, the eq. (1.29) can be rewritten as an undrained elastic constitutive relation:

$$\epsilon_{ij} = \frac{1}{2\mu}\left(\tau_{ij} - \frac{\nu_u}{1+\nu_u}\tau_{kk}\delta_{ij}\right), \tag{1.37}$$

where ν_u is the "undrained Poisson's ratio", given by the relation:

$$\nu_u = \frac{3\nu + B(1-2\nu)\frac{K}{H}}{3 - B(1-2\nu)\frac{K}{H}}. \tag{1.38}$$

1.3 TPE inclusion model in an unbounded space

1.3.1 Eshelby's Method

Eshelby (1957) provided a solution to certain problems in continuum mechanics in which the uniformity of an elastic medium is disturbed by the presence of a region undergoing volume and shape changes or possessing elastic parameters different from those of the surrounding medium. Specifically, Eshelby determined the deformation and stress within a region, called the "*inclusion*", enclosed by a closed surface S in a homogeneous and elastic material, referred to as the "*matrix*", which undergoes a spontaneous change in volume and shape. Before describing these steps, it is necessary to introduce the assumptions made by Eshelby:

I. The inclusion and the matrix remain bonded during the transformation. Thus, considering any pair of adjacent points immediately inside and outside the region, there is no relative displacement between them at the end of the process.

II. Before the transformation, both the inclusion and the matrix are stress-free and share the same elastic parameters.

The conceptual steps formulated by Eshelby are as follows:

1. A cut is made along S, and the inclusion is removed from the matrix, leaving a cavity with the same volume and shape as the inclusion. At the end of this step, both the inclusion and the matrix remain stress-free, and their original shapes are preserved due to the "*Kirchhoff's Uniqueness Theorem*".

2. The inclusion undergoes its volume and shape change, which in the case of TPE is generated by increments in pore pressure and temperature, resulting in a uniform stress-free strain ϵ^*_{ij}.

3. To reintegrate the inclusion into the cavity, it is restored to its original volume and shape by applying surface tractions T_j on S. These tractions can be expressed as $T_j = \tau^*_{ij} n_i$, where n_i is the i-th normal component of the inclusion's surface S, and $\tau^*_{ij} = -(\lambda \epsilon^*_{kk} \delta_{ij} + 2\mu \epsilon^*_{ij})$ is the stress tensor derived from ϵ^*_{ij}, resulting in a strain of $-\epsilon^*_{ij}$. The negative sign in τ^*_{ij} is due to the necessity of removing the previous strain ϵ^*_{ij} to restore the inclusion to its original shape and volume.

4. The inclusion is then reinserted into the cavity, and the material is bonded back together along S, maintaining the applied surface tractions, which now become an infinitesimal layer of distributed forces over the entire surface S. Each point of the matrix and inclusion occupies the same position as it did initially. Thus, the displacement field is zero everywhere, and the matrix remains stress-free, while within the inclusion, the stress is given by τ^*_{ij}.

5. The previously introduced force layer on each infinitesimal surface element dS is given by $dF_i = \tau^*_{ij} n_j dS$. To eliminate it and impose traction continuity on the surface, an additional force distribution $-dF_i = -\tau^*_{ij} n_j dS$ must be applied on S. This is equivalent to allowing the body forces that kept the inclusion in its previous shape to relax, enabling the matrix to constrain the inclusion. This new opposite force layer results in a nonzero displacement field, u^c_i, both within the matrix and the inclusion.

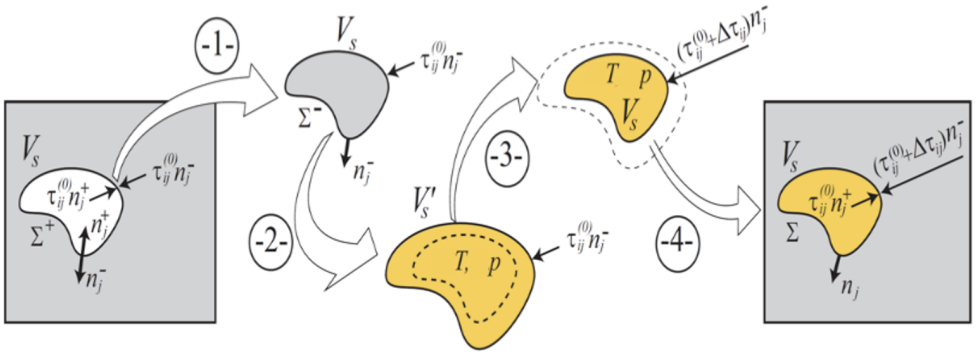

Figure 1.2: *Illustration of the conceptual steps of Eshelby's method (modified from Belardinelli et al. 2019), where assumption II is not made, but an initial stress field $\tau_{ij}^{(0)}$ is considered, and the tractions required to restore the inclusion's shape are indicated as $\Delta\tau_{ij}n_j^-$.*

As stated in Belardinelli et al. (2019), we can consider a bounded TPE region V_s, undergoing a change of temperature T and pore pressure p, surrounded by an unbounded elastic medium in drained and isothermal condition.
The first step is to evaluate the stress-free strain ϵ_{ij}^* inside the inclusion once it has been removed from the matrix and allowed to undergo a change in temperature T and pore pressure p. In stress-free condition, eq. (1.34) can be written as follow:

$$\epsilon_{ij}^* = \frac{1}{3H}p\delta_{ij} + \frac{1}{3}\alpha T\delta_{ij} = \epsilon_0\delta_{ij}. \tag{1.39}$$

The inclusion volume of course changes from V_s to V_s'; if pore pressure and temperature are constant within the inclusion (drained and isothermal conditions), the thermo-poro-elastic medium can be treated as purely elastic; hence, we can consider the inclusion and the matrix as both elastic. The stress field due to the restoration of the inclusion to its original shape is

$$\tau_{ij}^* = -(\lambda\epsilon_{kk}^*\delta_{ij} + 2\mu\epsilon_{ij}^*), \tag{1.40}$$

and by inserting eq. (1.39) we obtain

$$\tau_{ij}^* = -3K\epsilon_0\delta_{ij}, \tag{1.41}$$

where $K = \lambda + \frac{2}{3}\mu$ is the drained isothermal bulk modulus in an isotropic medium.
In order to relax the body forces spread over the surface separating the inclusion and the matrix S, it is necessary to apply a further distribution $-\tau_{ij}^*n_j$ over S. Now, the body is free of external forces, but it is in a self-state stress due to the transformation of the inclusion. In the following sections we will show displacement, strain and stress field, u_i^c, ϵ_{ij}^c, τ_{ij}^c, caused by the application of the traction $-\tau_{ij}^*n_j = 3K\epsilon_0 n_i$. Outside the source region V_s, the medium is assumed to be in isothermal free drainage conditions; its constitutive relation is then perfectly elastic, employing drained and isothermal elastic parameters.
Once we have u_i^c, we can compute $\epsilon_{ij}^c \doteq \frac{1}{2}\left(\frac{\partial u_i^c}{\partial x_j} + \frac{\partial u_j^c}{\partial x_i}\right)$ and $\tau_{ij}^c \doteq \lambda\epsilon_{kk}^c\delta_{ij} + 2\mu\epsilon_{ij}^c$.
The total stress inside the inclusion will be $\tau_{ij} = \tau_{ij}^c + \tau_{ij}^*$ Due to previous considerations, expression of the stress field is given by:

$$\tau_{ij} = \begin{cases} 2\mu\{\epsilon_{ij}^c + \frac{1}{1-2\nu}\left[\nu\epsilon_{kk}^c - (1+\nu)\epsilon_0\right]\delta_{ij}\} & \text{if } \mathbf{x} \in V_s \\ 2\mu\left(\epsilon_{ij}^c + \frac{\nu}{1-2\nu}\epsilon_{kk}^c\delta_{ij}\right) & \text{otherwise} \end{cases}. \tag{1.42}$$

1.3.2 Deformation field provided by a change in pore pressure p and temperature T

As outlined in various textbooks (e.g., Aki and Richards, 2002), a fundamental objective of elasticity theory is to express the displacement field generated by complex sources in terms of the response to the simplest possible source a unit impulse force applied in a single direction, precisely localized in both space and time (i.e., a delta-function body force). In the static case, such as the one considered here, the displacement field caused

by a unit force applied in a point of the medium is described by the elastic Green's function.
The general equation of elastostatics states that:

$$\frac{\partial \tau_{ij}}{\partial x_i} + f_j = 0, \tag{1.43}$$

where τ_{ij} is the stress tensor and f_j is the $j-$th component of the body force acting on it.
If we insert eq. (1.21), we obtain eq. (1.44) in terms of the displacement field:

$$C_{ijkl}\frac{\partial^2 u_k}{\partial x_l \partial x_i} + f_j = 0. \tag{1.44}$$

When the body force is a unit point force in the $n-$th direction, $f_j(\mathbf{x}) = \delta\left(|\mathbf{x} - \mathbf{x'}|\right)\delta_{jn}$, centered at the point $\mathbf{x'}$, the solution at a point $\mathbf{x}$ is the elastic Green's function $G_{kn}(\mathbf{x}, \mathbf{x'})$:

$$u_k(\mathbf{x}) = G_{kn}(\mathbf{x}, \mathbf{x'}) f_n(\mathbf{x'}). \tag{1.45}$$

Hence, $G_{kn}(\mathbf{x}, \mathbf{x'})$ represents the $k-$th component of displacement at point $\mathbf{x}$ due to the $n-$th component of a point force at $\mathbf{x'}$.
Thanks to the linearity of the equations of elastostatics, we are then able to write the displacement due to a distribution of volume forces $f_n(\mathbf{x'})$ in the form:

$$u_k(\mathbf{x}) = \int_V G_{kn}(\mathbf{x}, \mathbf{x'}) f_n(\mathbf{x'}) dV', \tag{1.46}$$

where dV' denotes an elementary volume in the surroundings of the point $\mathbf{x'}$.
In the case where the medium is unbounded, homogeneous, isotropic and elastic, the constitutive relation in eq. (1.23) can be inserted into eq. (1.44), and after a few algebraic steps and by writing $\frac{\lambda+\mu}{\mu} = \frac{1}{1-2\nu}$ the following expression of the Green function is obtained:

$$G_{kn}(\mathbf{x}, \mathbf{x'}) = \frac{1}{16\pi\mu(1-\nu)}\left[(3-4\nu)\frac{\delta_{kn}}{r} + \frac{(x_k - x'_k)(x_n - x'_n)}{r^3}\right], \tag{1.47}$$

where $r = |\mathbf{x} - \mathbf{x'}|$ is the distance between $\mathbf{x}$ and $\mathbf{x'}$.
The displacement u_i is exactly the displacement u_i^c in the previous paragraph (section 1.3.1). From now on, we will not use the superscript 'c' to lighten the notation.
By considering what we stated in section (1.3.1), the displacement field originated by the layer of body force $dF_i = -\tau_{ij}^* n_j dS$ can be obtained by integrating over the infinitesimal volume V where the forces are present:

$$u_i(\mathbf{x}) = \int_V G_{ij}(\mathbf{x}, \mathbf{x'}) dF_j(\mathbf{x'}) = -\int_S G_{ik}(\mathbf{x}, \mathbf{x'}) \tau_{kj}^* n_j(\mathbf{x'}) dS(\mathbf{x'}). \tag{1.48}$$

And, by applying the Gauss' theorem, eq. (1.48) becomes:

$$u_i(\mathbf{x}) = -\int_{V_s} \frac{\partial G_{ik}(\mathbf{x}, \mathbf{x'})}{\partial x'_j} \tau_{kj}^* dV(\mathbf{x'}) - \int_{V_s} G_{ik}(\mathbf{x}, \mathbf{x'}) \frac{\partial \tau_{kj}^*}{\partial x'_j} dV(\mathbf{x'}), \tag{1.49}$$

and the last term is identically null, as τ_{kj}^* is constant and V_s is the volume of the inclusion. Hence, substituting in eq. (1.49) τ_{ij}^* from eq. (1.41), the expression of the displacement field produced by the traction $\Delta T_k = 3K\epsilon_0 n_k$ is:

$$u_i(\mathbf{x}) = 3K\epsilon_0 \int_{V_s} \frac{\partial G_{ik}(\mathbf{x}, \mathbf{x'})}{\partial x'_k} dV', \tag{1.50}$$

where $\frac{\partial G_{ik}(\mathbf{x},\mathbf{x'})}{\partial x'_k}$ may be interpreted as the displacement in $\mathbf{x}$ produced by three orthogonal force dipoles with unit moment centered in $\mathbf{x'}$.
In order to compute the displacement field it is necessary to determine $\frac{\partial G_{ik}(\mathbf{x},\mathbf{x'})}{\partial x'_k}$ as follows:

$$\frac{\partial G_{ik}(\mathbf{x},\mathbf{x'})}{\partial x'_k} = \frac{1-2\nu}{8\pi\mu(1-\nu)}\frac{x_i - x'_i}{r^3} = \frac{1-2\nu}{8\pi\mu(1-\nu)}\frac{\partial}{\partial x'_i}\left(\frac{1}{r}\right). \tag{1.51}$$

In an unbounded medium the Green's function has the following property: $G_{ik}(\mathbf{x},\mathbf{x'}) = G_{ik}(\mathbf{x}-\mathbf{x'})$. By applying previous property one obtains:

$$\frac{\partial G_{ik}(\mathbf{x},\mathbf{x'})}{\partial x'_k} = -\frac{1-2\nu}{8\pi\mu(1-\nu)}\frac{\partial}{\partial x_i}\left(\frac{1}{r}\right) = -\frac{1-2\nu}{8\pi\mu(1-\nu)}\nabla\left(\frac{1}{r}\right). \tag{1.52}$$

By using eq. (1.52) we can rewrite eq. (1.50) in vector form as:

$$\mathbf{u}(\mathbf{x}) = -\epsilon_0\frac{1+\nu}{4\pi(1-\nu)}\nabla\int_{V_s}\frac{1}{|\mathbf{x}-\mathbf{x'}|}dV' = -\frac{\epsilon_1}{4\pi}\nabla\Phi_d, \tag{1.53}$$

where

$$\Phi_d(\mathbf{x}) \doteq \int_{V_s}\frac{1}{|\mathbf{x}-\mathbf{x'}|}dV' \tag{1.54}$$

is the scalar displacement potential, and

$$\epsilon_1 \doteq \epsilon_0\frac{1+\nu}{1-\nu}. \tag{1.55}$$

It is possible to observe that the displacement field is irrotational, i.e. $\nabla\times\mathbf{u} = 0$, and, taking to account that $\nabla^2\left(\frac{1}{r}\right) = -4\pi\delta(\mathbf{x}-\mathbf{x'})$, we get:

$$\nabla\cdot\mathbf{u} = -\frac{\epsilon_1}{4\pi}\nabla^2\Phi_d = \epsilon_1\int_{V_s}\delta(\mathbf{x}-\mathbf{x'})dV', \tag{1.56}$$

hence, $\nabla\cdot\mathbf{u} = \epsilon_1$ if $\mathbf{x}\in V_s$ and is equal to zero otherwise. This means that ϵ_1 represents the dilatation within the TPE source. The displacement potential Φ_d obeys the Poisson equation $\nabla^2\Phi_S = -4\pi$ within the TPE source and the Laplace equation $\nabla^2\Phi_M = 0$ in the embedding matrix.
In the embedding matrix we have, according to eq. (1.56), $\epsilon_{kk} = 0$, while within the TPE source $\epsilon_{kk} = \epsilon_1$. The strain and the stress fields can be determined from eq. (1.42):

$$\epsilon_{ij} \doteq \begin{cases}\epsilon_{ij}^{(S)} & \text{if } \mathbf{x}\in V_s\\ \epsilon_{ij}^{(M)} & \text{otherwise}\end{cases} = -\frac{\epsilon_1}{4\pi}\begin{cases}\frac{\partial^2\Phi_S}{\partial x_i\partial x_j} & \text{if } \mathbf{x}\in V_s\\ \frac{\partial^2\Phi_M}{\partial x_i\partial x_j} & \text{otherwise}\end{cases}; \tag{1.57}$$

$$\tau_{ij} \doteq \begin{cases}\tau_{ij}^{(S)} & \text{if } \mathbf{x}\in V_s\\ \tau_{ij}^{(M)} & \text{otherwise}\end{cases} = -\frac{2\mu\epsilon_1}{4\pi}\begin{cases}\frac{\partial^2\Phi_S}{\partial x_i\partial x_j} + \delta_{ij} & \text{if } \mathbf{x}\in V_s\\ \frac{\partial^2\Phi_M}{\partial x_i\partial x_j} & \text{otherwise}\end{cases}. \tag{1.58}$$

As mentioned before, we must have the continuity of the tractions $T_i(\mathbf{n}) = \tau_{ij}n_j$ applied on the boundary Σ of the source region V_s, but this requires a discontinuity in the second derivatives of Φ:

$$\left(\frac{\partial^2\Phi_M}{\partial x_i\partial x_j} - \frac{\partial^2\Phi_S}{\partial x_i\partial x_j}\right)_\Sigma n_j = 4\pi n_i. \tag{1.59}$$

This statement is equivalent to require that the linear dilatation $\epsilon_{ij}n_in_j$ in the normal direction to the boundary of the TPE region has a discontinuity of the first kind across Σ, with jump amplitude $-\epsilon_1$, that means a contraction outside the TPE source and a dilatation inside along the normal direction.

1.3.3 Displacement and stress for a spherical TPE inclusion located in an unbounded elastic medium

Due to the geometry of the problem, Belardinelli et al. (2019) used spherical coordinates, (r, θ, ϕ), in order to describe such components. In particular, r is the distance from the origin of the reference system, θ is the colatitude, and ϕ the longitude (for more details, see Appendix A). They used a reference system, showed in Fig. (2.1), centered in the center of a sphere of radius a, located at a depth z_0. The only non-vanishing component of the displacement is u_r, since invariance arguments suggested that $\mathbf{u} = u_r(r)\frac{\mathbf{r}}{r}$.
The potential displacement field obtained from Belardinelli et al. (2019) is given by:

$$\Phi_d(r) = 2\pi a^2 \begin{cases} \left(1 - \frac{1}{3}\frac{r^2}{a^2}\right) & \text{if } r < a \\ \frac{2}{3}\frac{a}{r} & \text{if } r \geq a \end{cases}. \tag{1.60}$$

It is possible to compute the displacement field from eq. (1.61):

$$u_r(r) = \frac{1}{3}\epsilon_1 a \begin{cases} \frac{r}{a} & \text{if } r < a \\ \frac{a^2}{r^2} & \text{if } r \geq a \end{cases}. \tag{1.61}$$

From eq. (1.58) it is possible to obtain the stress components. In spherical coordinates, the non-vanishing components of the stress field are the following:

$$\tau_{rr}(r) = -\frac{4}{3}\mu\epsilon_1 \begin{cases} 1 & \text{if } r < a \\ \left(\frac{a}{r}\right)^3 & \text{if } r \geq a \end{cases}, \tag{1.62}$$

and

$$\tau_{\theta\theta}(r) = \tau_{\phi\phi}(r) = -\frac{4}{3}\mu\epsilon_1 \begin{cases} 1 & \text{if } r < a \\ -\frac{1}{2}\left(\frac{a}{r}\right)^3 & \text{if } r \geq a \end{cases}. \tag{1.63}$$

1.3.4 Displacement and stress for a spherical shell TPE inclusion located in an unbounded elastic medium

A formally similar problem that has closed-form solutions is the spherical TPE shell enclosing a spherical fluid-like reservoir with radius a at pressure P_0, bounded by a spherical surface with radius $b > a$. The region $r \leq a$ can be considered as a magmatic fluid reservoir at pressure P_0 or, more generally, as a viscoelastic region surrounding a magmatic reservoir where, in the long term (after a few Maxwell times), an isotropic stress state $\tau_{ij} = -P_0\delta_{ij}$ is reached (Belardinelli et al., 2019). The displacement field obtained from Belardinelli et al. (2019) is given by:

$$u_r(r) = \begin{cases} \frac{P_0 a^3}{4\mu r^2} + \frac{1}{3}\epsilon_1\left(r - \frac{a^3}{r^2}\right) & \text{if } a \leq r \leq b \\ \frac{P_0 a^3}{4\mu r^2} + \frac{1}{3}\epsilon_1\frac{b^3 - a^3}{r^2} & \text{if } r > b \end{cases}. \tag{1.64}$$

In spherical coordinates, the non-vanishing components of the stress field are the following:

$$\tau_{rr}(r) = \begin{cases} -P_0\frac{a^3}{r^3} - \frac{4}{3}\mu\epsilon_1\left(1 - \frac{a^3}{r^3}\right) & \text{if } a \leq r \leq b \\ -P_0\frac{a^3}{r^3} - \frac{4}{3}\mu\epsilon_1\frac{b^3 - a^3}{r^3} & \text{if } r > b \end{cases}, \tag{1.65}$$

and

$$\tau_{\theta\theta}(r) = \tau_{\phi\phi}(r) = \begin{cases} P_0 \frac{a^3}{2r^3} - \frac{4}{3}\mu\epsilon_1 \left(1 + \frac{a^3}{2r^3}\right) & \text{if } a \leq r < b \\ P_0 \frac{a^3}{2r^3} + \frac{2}{3}\mu\epsilon_1 \frac{b^3 - a^3}{r^3} & \text{if } r > b \end{cases} . \tag{1.66}$$

The displacement u_i^m and stress τ_{ij}^m (associated to the inner magmatic chamber) existing prior to the onset of degassing processes can be simply obtained by setting $\epsilon_1 = 0$ and $P_0 = P_m$ in eqq. (1.64); (1.65); (1.66). Degassing is plausibly associated with a pressure decrease from P_m to $P_0 < P_m$ within the magmatic reservoir ($r < a$). The incremental displacement and stress fields, defined as $u_i^{(S/M)} - u_i^m$ and $\tau_{ij}^{(S/M)} - \tau_{ij}^m$, respectively, are then obtained by replacing P_0 with $(P_0 - P_m)$ in eqq. (1.64); (1.65); (1.66). Here, the superscripts (S) and (M) denote the solutions inside the source (i.e., $a \leq r \leq b$) and in the matrix (i.e., $r > b$), respectively.

Chapter 2

Spherically-symmetric TPE inclusions located in a half-space

This chapter presents the core contribution of this thesis: the generalization of the solutions proposed by Belardinelli et al. (2019) to compute displacement, stress, and strain throughout the entire half-space using a method described in section (2.1). The approach leads to closed-form expressions for the components of the displacement, stress, and strain fields generated by both a spherical TPE source embedded in a half-space with a free surface. Unlike many previous studies (e.g., Stissi et al. 2023), which focus on surface displacements, the formulation developed here provides the complete vector field within the medium, including stress and strain components. Such a step is essential for comparing the TPE inclusion model with seismic and gravimetric data, as interpreting these data requires knowledge of displacements, deformations, and stresses not only at the free surface, but also at depth and in the near-surface region. Since the problem is axi-symmetric, results expressed in section (1.3) can be written in cylindrical coordinates (ρ, φ, z). The adopted reference system is that centered on the free surface $z = 0$ and with the z axis oriented in the direction of the increasing depth. The model of a TPE inclusion located within the half-space $z > 0$ must therefore satisfy the stress-free boundary condition at the surface:

$$\tau_{\rho z}(\rho, \varphi, 0) = \tau_{\varphi z}(\rho, \varphi, 0) = \tau_{zz}(\rho, \varphi, 0) = 0. \tag{2.1}$$

The $\tau_{\varphi\varphi}$ component is vanishing for the axi-symmetry hypothesis; in order to remove the $\tau_{\rho z}$ component, the method of a source "image" can be exploited. Since the TPE source center is placed at $z = +z_0$, we can consider the image source center located in $z = -z_0$. To remove the normal component τ_{zz}, it is necessary to apply a procedure that starts with the method explained in the following subsection.

2.1 Introduction of the free surface for a spherical source

In cylindrical coordinates the expression of the non-vanishing components of the displacement field in an unboundend medium, expressed in eq. (1.61), are the following:

$$u_z^I(\rho, z) = \frac{1}{3}\epsilon_1 a \begin{cases} \frac{z-z_0}{a} & \text{if } \sqrt{\rho^2 + (z-z_0)^2} < a \\ \frac{a^2(z-z_0)}{(\rho^2+(z-z_0)^2)^{3/2}} & \text{if } \sqrt{\rho^2 + (z-z_0)^2} \geq a \end{cases}; \tag{2.2}$$

$$u_\rho^I(\rho,z)=\frac{1}{3}\epsilon_1 a\begin{cases}\frac{\rho}{a} & \text{if } \sqrt{\rho^2+(z-z_0)^2}<a\\ \frac{a^2\rho}{(\rho^2+(z-z_0)^2)^{3/2}} & \text{if } \sqrt{\rho^2+(z-z_0)^2}\geq a\end{cases}. \tag{2.3}$$

In Fig. (2.1) the reference system used in this work is represented. In the same figure I show the reference system used by Belardinelli et al. (2019) (i.e., spherical coordinates (r,θ,ϕ), with origin in the center of the sphere) with the only difference being that the z-axis was oriented in the opposite direction.

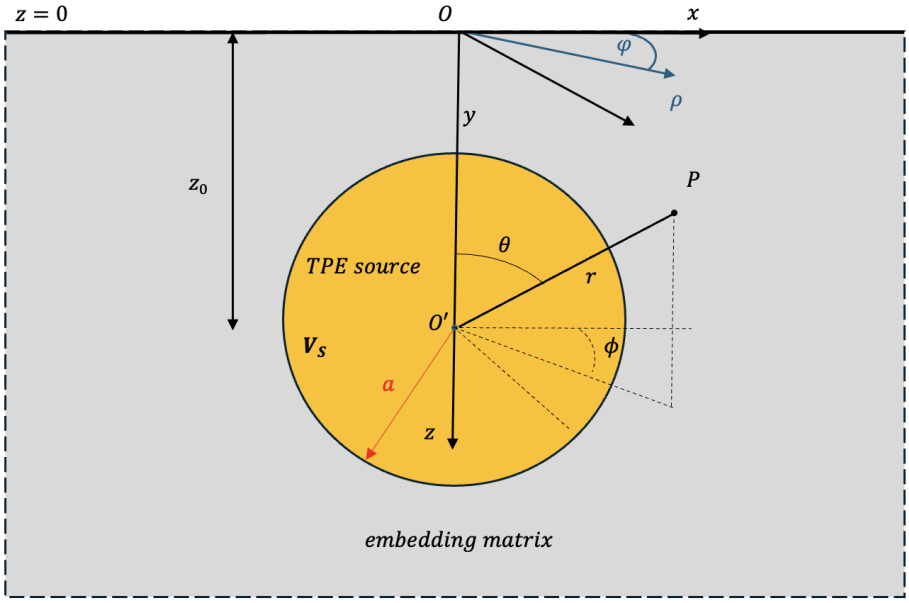

Figure 2.1: *Spherical TPE region (yellow) of radius a surrounded by an embedding matrix (gray) in drained isothermal conditions. The reference system, in cartesian (black) coordinates (x,y,z) and cylindrical (blue) coordinates (ρ,φ,z), is also represented. The origin of the reference system lies on the free surface ($z=0$) and the $z-$axis is taken positive in the downward direction. The center of the median plane of the TPE sphere is located at $(0;0;z_0)$. The reference system used by Belardinelli et al. (2019), expressed in spherical coordinates (r,θ,ϕ) and with the origin located in the center of the sphere, is also reported.*

In Appendix A.1 we computed the expressions of the non-vanishing stress components generated by the spherical TPE inclusion in an unbounded medium.
If we sum the contribution of the image source, placed in $z=-z_0$, the displacement's components in eqq. (2.3) and (2.2) assume the form:

$$u_z^{II}(\rho,z)=\frac{1}{3}\epsilon_1 a\begin{cases}\frac{z-z_0}{a}+\frac{a^2(z+z_0)}{(\rho^2+(z+z_0)^2)^{3/2}} & \text{if } \sqrt{\rho^2+(z-z_0)^2}<a\\ \frac{a^2(z-z_0)}{(\rho^2+(z-z_0)^2)^{3/2}}+\frac{a^2(z+z_0)}{(\rho^2+(z+z_0)^2)^{3/2}} & \text{if } \sqrt{\rho^2+(z-z_0)^2}\geq a\end{cases}; \tag{2.4}$$

$$u_\rho^{II}(\rho,z)=\frac{1}{3}\epsilon_1 a\begin{cases}\frac{\rho}{a}+\frac{a^2\rho}{(\rho^2+(z+z_0)^2)^{3/2}} & \text{if } \sqrt{\rho^2+(z-z_0)^2}<a\\ \frac{a^2\rho}{(\rho^2+(z-z_0)^2)^{3/2}}+\frac{a^2\rho}{(\rho^2+(z+z_0)^2)^{3/2}} & \text{if } \sqrt{\rho^2+(z-z_0)^2}\geq a\end{cases}. \tag{2.5}$$

In the same way we can obtain the stress components.
As expected, the component $\tau_{z\rho}^{II}$ vanishes in $z=0$ because we have considered the contribution of an image source in $z=-z_0$ (this statement will be proved analytically at the end of the paragraph). In order to remove the stress component τ_{zz}^{II} in $z=0$ it

is necessary to add the solution of the elastic problem in a half-space with the imposed boundary condition $-\tau_{zz}^{II}$ in $z = 0$. Hence, it is important to determine the expression, in cylindrical coordinates, of τ_{zz}^{II}. We can determine τ_{zz}^{I} from eq. (A.11) or with the relations reported in Appendix A:

$$\tau_{zz}^{I}(\rho, \varphi, z) = \tau_{rr} \cos^2\theta - \tau_{\theta r} \sin\theta \cos\theta + \tau_{\theta\theta} \sin^2\theta. \tag{2.6}$$

The last equation, considering that $\tau_{\theta r} = 0$ and, for the geometry of the problem, $\cos^2\theta = \frac{(z-z_0)^2}{\rho^2+(z-z_0)^2}$, and for the first fundamental relation of goniometry $\sin^2\theta = 1 - \cos^2\theta$, can be rewritten as follows:

$$\tau_{zz}^{I} = -\frac{2}{3}\mu\epsilon_1 a^3 \left(\frac{3(z-z_0)^2}{(\rho^2+(z-z_0)^2)^{5/2}} - \frac{1}{(\rho^2+(z-z_0)^2)^{3/2}} \right). \tag{2.7}$$

In order to determine the expression of τ_{zz}^{II} one has to consider the contribution of the image source, which, outside the inclusion (as it is at the free surface), is:

$$\tau_{zz}^{II} = -\frac{2}{3}\mu\epsilon_1 a^3 \left(\frac{3(z-z_0)^2}{(\rho^2+(z-z_0)^2)^{5/2}} - \frac{1}{(\rho^2+(z-z_0)^2)^{3/2}} + \frac{3(z+z_0)^2}{(\rho^2+(z+z_0)^2)^{5/2}} - \frac{1}{(\rho^2+(z+z_0)^2)^{3/2}} \right). \tag{2.8}$$

In $z = 0$ the previous expression becomes:

$$\tau_{zz}^{II}(\rho, 0) = -\frac{4}{3}\mu\epsilon_1 a^3 \left(\frac{3z_0^2}{(\rho^2+z_0^2)^{5/2}} - \frac{1}{(\rho^2+z_0^2)^{3/2}} \right) \neq 0. \tag{2.9}$$

Similarly, from eq. (A.12) or with the relations in Appendix A, and by adding the contribution of the image source, it is also possible to obtain the stress component $\tau_{\rho z}^{II}$:

$$\tau_{\rho z}^{II} = -2\mu\epsilon_1 a^3 \left(\frac{\rho(z-z_0)}{(\rho^2+(z-z_0)^2)^{5/2}} + \frac{\rho(z+z_0)}{(\rho^2+(z+z_0)^2)^{5/2}} \right), \tag{2.10}$$

and we can notice that $\tau_{\rho z}^{II}(\rho, 0) = 0$, and hence the prove that free surface condition is verified.

To remove the traction component in eq. (2.9), Bonafede (1990) showed the importance of the following strategy, by applying this method for a magmatic chamber.

Let us consider a solution of an axi-symmetric elasto-static problem in an unbounded medium (labeled with the superscript Z) such that:

$$\begin{cases} \tau_{zz}^{Z} = -S_0(\rho) & \text{in } z = 0; \\ \tau_{\rho z}^{Z} = \tau_{\varphi z}^{Z} = 0 & \text{in } z = 0, \end{cases} \tag{2.11}$$

where $S_0(\rho)$ is a known function as the one in the second member of eq. (2.9). Besides this boundary condition, the solution is bounded in term of displacement, deformation and stress at $z \to +\infty$. The axial symmetry can be exploited by expanding S_0 through Hankel transforms:

$$S_0(\rho) = \int_0^\infty dc\ J_0(\rho c)\tilde{S}_0(c), \tag{2.12}$$

where:

$$\tilde{S}_0(c) = \int_0^\infty d\rho\ c\rho J_0(\rho c) S_0(\rho), \tag{2.13}$$

and $J_0(\rho c)$ is the Bessel function of order zero.
It can be shown that in the absence of body forces this solution can be determined from the so called strain function of Love Z which fulfills the biharmonic equation:

$$\nabla^4 Z(\rho, z) = 0. \tag{2.14}$$

Knowing Z it is possible to derive displacement and stress from the following equations:

$$u_\rho^Z = -\frac{1}{2\mu}\frac{\partial^2 Z}{\partial\rho\partial z}; \tag{2.15}$$

$$u_z^Z = \frac{1}{2\mu}\left[2(1-\nu)\nabla^2 - \frac{\partial^2}{\partial z^2}\right] Z. \tag{2.16}$$

$$\tau_{\rho\rho}^Z = \frac{\partial}{\partial z}\left(\nu\nabla^2 - \frac{\partial^2}{\partial\rho^2}\right) Z; \tag{2.17}$$

$$\tau_{zz}^Z = \frac{\partial}{\partial z}\left[(2-\nu)\nabla^2 - \frac{\partial^2}{\partial z^2}\right] Z; \tag{2.18}$$

$$\tau_{\rho z}^Z = \frac{\partial}{\partial \rho}\left[(1-\nu)\nabla^2 - \frac{\partial^2}{\partial z^2}\right] Z. \tag{2.19}$$

If we sum the solution with superscript "II" to the solution with superscript "Z", and if $S_0(\rho)$ equals the normal traction at $z = 0$ expressed by eq. (2.9), by construction, the total solution represents zero normal traction in $z = 0$. It is important to state that the application of this procedure does not change $\tau_{\rho z}$, which is identically null at the free surface. For an axi-symmetric elastostatic problem, the Z function is the only non vanishing component of the so called Galerkin vector. The solutions for Z and u_i^Z are reported in Appendix B.

2.2 Expressions of displacement, stress and strain components for a spherical source

2.2.1 Displacement components

Once we have determined u_z^Z and u_ρ^Z, respectively in eq. (B.57) and eq. (B.64), we must add the results at u_z^{II} and u_ρ^{II}, respectively expressed in eq. (2.4) and eq. (2.2). By defining with $R(\rho, z) \doteq ((z - z_0)^2 + \rho^2)^{1/2}$ the distance from the TPE source and with $R^*(\rho, z) \doteq ((z + z_0)^2 + \rho^2)^{1/2}$ the distance from the image TPE source, we get:

$$u_z(\rho, z) = -\frac{1}{3}\epsilon_1 a^3 \begin{cases} -\frac{z-z_0}{a^3} + (3-4\nu)\frac{z+z_0}{R^{*3}} - 2\frac{z}{R^{*3}} + 6\frac{z(z+z_0)^2}{R^{*5}} & \text{if } R < a \\ -\frac{z-z_0}{R^3} + (3-4\nu)\frac{z+z_0}{R^{*3}} - 2\frac{z}{R^{*3}} + 6\frac{z(z+z_0)^2}{R^{*5}} & \text{if } R \geq a \end{cases}; \tag{2.20}$$

$$u_\rho(\rho, z) = \frac{1}{3}\epsilon_1 a^3 \begin{cases} \frac{\rho}{a^3} + (3-4\nu)\frac{\rho}{R^{*3}} - 6\frac{z(z+z_0)\rho}{R^{*5}} & \text{if } R < a \\ \frac{\rho}{R^3} + (3-4\nu)\frac{\rho}{R^{*3}} - 6\frac{z(z+z_0)\rho}{R^{*5}} & \text{if } R \geq a \end{cases}. \tag{2.21}$$

If a vector field is irrotational, it can be expressed as the gradient of a scalar potential; in three dimensions, this implies that its curl is zero:

$$\nabla \times \mathbf{u} = \mathbf{0}. \tag{2.22}$$

In cylindrical coordinates, we have that:

$$\nabla \times \mathbf{u} = \left(\frac{1}{\rho}\frac{\partial u_z}{\partial \varphi} - \frac{\partial u_\varphi}{\partial z}\right)\hat{\rho} + \left(\frac{\partial u_\rho}{\partial z} - \frac{\partial u_z}{\partial \rho}\right)\hat{\varphi} + \frac{1}{\rho}\left(\frac{\partial(\rho u_\varphi)}{\partial \rho} - \frac{\partial u_\rho}{\partial \varphi}\right)\hat{z}. \tag{2.23}$$

By substituting eq. (2.20) and eq. (2.21) into eq. (2.23), and knowing that u_φ is identically null, we get in each point in the domain:

$$\nabla \times \mathbf{u} = -8\epsilon_1 a^3(1-\nu)\frac{\rho(z+z_0)}{R^{*5}}\hat{\varphi}. \tag{2.24}$$

We obtained that, in general, $\nabla \times \mathbf{u}$ does not vanish, hence the displacement field is not irrotational, and so we cannot find an associated scalar potential, unlike in the case of an unbounded medium (section 1.3.3).

2.2.2 Strain components

From eq. (2.20) and eq. (2.21) is possible to determine the strain components ϵ_{ij}. In principle, we can state that, for the geometry of the problem, the components $\epsilon_{\varphi\rho}$, $\epsilon_{\varphi z}$ are identically null.
The diagonal component $\epsilon_{\rho\rho}$ can be determined as follows:

$$\epsilon_{\rho\rho} = \frac{\partial u_\rho}{\partial \rho}, \tag{2.25}$$

and its expression is:

$$\epsilon_{\rho\rho}(\rho,z) = \frac{1}{3}\epsilon_1 a^3 \begin{cases} \frac{1}{a^3} + \frac{(3-4\nu)}{R^{*3}} - \frac{3(3-4\nu)\rho^2}{R^{*5}} - \frac{6z(z+z_0)}{R^{*5}} + \frac{30z(z+z_0)\rho^2}{R^{*7}} & \text{if } R < a \\ \frac{1}{R^3} - \frac{3\rho^2}{R^5} + \frac{(3-4\nu)}{R^{*3}} - \frac{3(3-4\nu)\rho^2}{R^{*5}} - \frac{6z(z+z_0)}{R^{*5}} + \frac{30z(z+z_0)\rho^2}{R^{*7}} & \text{if } R \geq a \end{cases}. \tag{2.26}$$

The other diagonal component $\epsilon_{\varphi\varphi}$ can be determined as follows:

$$\epsilon_{\varphi\varphi} = \frac{u_\rho}{\rho} + \frac{1}{r}\frac{\partial u_\varphi}{\partial \varphi}, \tag{2.27}$$

and its expression is:

$$\epsilon_{\varphi\varphi}(\rho,z) = \frac{1}{3}\epsilon_1 a^3 \begin{cases} \frac{1}{a^3} + \frac{(3-4\nu)}{R^{*3}} - \frac{6z(z+z_0)}{R^{*5}} & \text{if } R < a \\ \frac{1}{R^3} + \frac{(3-4\nu)}{R^{*3}} - \frac{6z(z+z_0)}{R^{*5}} & \text{if } R \geq a \end{cases}. \tag{2.28}$$

The last diagonal component ϵ_{zz} can be determined as follows:

$$\epsilon_{zz} = \frac{\partial u_z}{\partial z}, \tag{2.29}$$

and its expression is:

$$\epsilon_{zz}(\rho,z) = \frac{1}{3}\epsilon_1 a^3 \begin{cases} \frac{1}{a^3} - \frac{(1-4\nu)}{R^{*3}} + \frac{3(3-4\nu)(z+z_0)^2}{R^{*5}} - \frac{6(z+z_0)(4z+z_0)}{R^{*5}} + \frac{30z(z+z_0)^3}{R^{*7}} & \text{if } R < a \\ \frac{1}{R^3} - \frac{(1-4\nu)}{R^{*3}} - \frac{3(z-z_0)^2}{R^5} + \frac{3(3-4\nu)(z+z_0)^2}{R^{*5}} - \frac{6(z+z_0)(4z+z_0)}{R^{*5}} + \frac{30z(z+z_0)^3}{R^{*7}} & \text{if } R \geq a \end{cases}. \tag{2.30}$$

The only non-vanishing non-diagonal component is $\epsilon_{\rho z}$, and it can be determined as follows:

$$\epsilon_{\rho z} = \frac{1}{2}\left(\frac{\partial u_\rho}{\partial z} + \frac{\partial u_z}{\partial \rho}\right), \tag{2.31}$$

and its expression is:

$$\epsilon_{\rho z}(\rho, z) = \frac{1}{3}\epsilon_1 a^3 \begin{cases} -\frac{3\rho(3z+z_0)}{R^{*5}} + \frac{30\rho z(z+z_0)^2}{R^{*7}} & \text{if } R < a \\ -\frac{3\rho(z-z_0)}{R^5} - \frac{3\rho(3z+z_0)}{R^{*5}} + \frac{30\rho z(z+z_0)^2}{R^{*7}} & \text{if } R \geq a \end{cases}. \tag{2.32}$$

2.2.3 Stress components

The stress field within the source region V_s (i.e., $R < a$) and in the embedding matrix (i.e., $R \geq a$), due to the constitutive relation, are given by eq. (1.42).
In particular, from eq. (1.42), one can compute τ_{zz} as follows:

$$\tau_{zz} = \frac{2\mu}{1-2\nu} \begin{cases} (1-\nu)\epsilon_{zz} + \nu(\epsilon_{\rho\rho} + \epsilon_{\varphi\varphi}) - (1+\nu)\epsilon_0 & \text{if } R < a \\ (1-\nu)\epsilon_{zz} + \nu(\epsilon_{\rho\rho} + \epsilon_{\varphi\varphi}) & \text{if } R \geq a \end{cases}. \tag{2.33}$$

The result for $R < a$ is the following:

$$\begin{aligned} \tau_{zz}(\rho, z) = \frac{2\mu}{3(1-2\nu)}\epsilon_1 a^3 \Bigg(& \frac{1+\nu}{a^3} + \frac{-12\nu^2 + 11\nu - 1}{R^{*3}} + \frac{3(3-4\nu)\left[(z+z_0)^2(1-\nu) - \nu\rho^2\right]}{R^{*5}} \\ & - \frac{6(z+z_0)[2z(2-\nu) + z_0(1-\nu)]}{R^{*5}} + \frac{30z(z+z_0)[(1-\nu)(z+z_0)^2 + \nu\rho^2)]}{R^{*7}} \\ & - \frac{3(1+\nu)}{a^3}\frac{\epsilon_0}{\epsilon_1}\Bigg) \\ = \tau^I_{zz}(\rho, z) & \\ + \frac{2\mu}{3(1-2\nu)}\epsilon_1 a^3 \Bigg(& \frac{-12\nu^2 + 11\nu - 1}{R^{*3}} + \frac{3(3-4\nu)\left[(z+z_0)^2(1-\nu) - \nu\rho^2\right]}{R^{*5}} \\ & - \frac{6(z+z_0)[2z(2-\nu) + z_0(1-\nu)]}{R^{*5}} + \frac{30z(z+z_0)[(1-\nu)(z+z_0)^2 + \nu\rho^2)]}{R^{*7}}\Bigg), \end{aligned} \tag{2.34}$$

and for $R \geq a$ is:

$$\begin{aligned} \tau_{zz}(\rho, z) = \frac{2\mu}{3(1-2\nu)}\epsilon_1 a^3 \Bigg(& \frac{(1+\nu)}{R^3} - \frac{3\left[\nu\rho^2 + (1-\nu)(z-z_0)^2\right]}{R^5} + \frac{(-12\nu^2 + 11\nu - 1)}{R^{*3}} \\ & + \frac{3(3-4\nu)\left[(z+z_0)^2(1-\nu) - \nu\rho^2\right]}{R^{*5}} - \frac{6(1-\nu)(z+z_0)(2z+z_0)}{R^{*5}} \\ & + \frac{30z(z+z_0)\left[(1-\nu)(z+z_0)^2 + \nu\rho^2\right]}{R^{*7}}\Bigg) \\ = \tau^I_{zz}(\rho, z) & \\ + \frac{2\mu}{3(1-2\nu)}\epsilon_1 a^3 \Bigg(& \frac{-12\nu^2 + 11\nu - 1}{R^{*3}} + \frac{3(3-4\nu)\left[(z+z_0)^2(1-\nu) - \nu\rho^2\right]}{R^{*5}} \\ & - \frac{6(z+z_0)[2z(2-\nu) + z_0(1-\nu)](1-\nu)}{R^{*5}} \\ & + \frac{30z(z+z_0)[(1-\nu)(z+z_0)^2 + \nu\rho^2)]}{R^{*7}}\Bigg). \end{aligned} \tag{2.35}$$

The non-diagonal component $\tau_{\rho z}$ can be computed, from eq. (1.42), by:

$$\tau_{\rho z} = 2\mu \begin{cases} \epsilon_{\rho z} & \text{if } R < a \\ \epsilon_{\rho z} & \text{if } R \geq a \end{cases}. \tag{2.36}$$

The result for $R < a$ is the following:

$$\tau_{\rho z}(\rho, z) = 2\mu\epsilon_1 a^3 \left(-\frac{\rho(3z + z_0)}{R^{*5}} + \frac{10\rho z(z + z_0)^2}{R^{*7}} \right), \tag{2.37}$$

and for $R \geq a$ is:

$$\tau_{\rho z}(\rho, z) = 2\mu\epsilon_1 a^3 \left(-\frac{\rho(z - z_0)}{R^5} - \frac{(3z + z_0)\rho}{R^{*5}} + \frac{10\rho z(z + z_0)^2}{R^{*7}} \right). \tag{2.38}$$

The diagonal component $\tau_{\rho\rho}$ can be calculated, from eq. (1.42), by:

$$\tau_{\rho\rho} = \frac{2\mu}{1 - 2\nu} \begin{cases} (1 - \nu)\epsilon_{\rho\rho} + \nu(\epsilon_{\varphi\varphi} + \epsilon_{zz}) - (1 + \nu)\epsilon_0 & \text{if } R < a \\ (1 - \nu)\epsilon_{\rho\rho} + \nu(\epsilon_{\varphi\varphi} + \epsilon_{zz}) & \text{if } R \geq a \end{cases}. \tag{2.39}$$

The result for $R < a$ is the following:

$$\begin{aligned} \tau_{\rho\rho}(\rho, z) = \frac{2\mu}{3(1 - 2\nu)}\epsilon_1 a^3 \Bigg(& \frac{1 + \nu}{a^3} + \frac{3 - 5\nu + 4\nu^2}{R^{*3}} + \frac{3(3 - 4\nu)\left[-(1 - \nu)\rho^2 + \nu(z + z_0)^2\right]}{R^{*5}} \\ & - \frac{6(z + z_0)\left[z + \nu(4z + z_0)\right]}{R^{*5}} + \frac{30z(z + z_0)\left[(1 - \nu)\rho^2 + \nu(z + z_0)^2\right]}{R^{*7}} \\ & - \frac{3(1 + \nu)}{a^3}\frac{\epsilon_0}{\epsilon_1} \Bigg) \\ = \tau^I_{\rho\rho}(\rho, z) + \frac{2\mu}{3(1 - 2\nu)}\epsilon_1 a^3 \Bigg(& \frac{3 - 5\nu + 4\nu^2}{R^{*3}} \\ & + \frac{3(3 - 4\nu)\left[-(1 - \nu)\rho^2 + \nu(z + z_0)^2\right]}{R^{*5}} - \frac{6(z + z_0)\left[z + \nu(4z + z_0)\right]}{R^{*5}} \\ & + \frac{30z(z + z_0)\left[(1 - \nu)\rho^2 + \nu(z + z_0)^2\right]}{R^{*7}} - \frac{3(1 + \nu)}{a^3}\frac{\epsilon_0}{\epsilon_1} \Bigg), \end{aligned} \tag{2.40}$$

and for $R \geq a$ is:

$$\begin{aligned} \tau_{\rho\rho}(\rho, z) = \frac{2\mu}{3(1 - 2\nu)}\epsilon_1 a^3 \Bigg(& \frac{1 + \nu}{R^3} - \frac{3\left[\nu(z - z_0)^2 + (1 - \nu)\rho^2\right]}{R^5} + \frac{3 - 5\nu + 4\nu^2}{R^{*3}} \\ & + \frac{3(3 - 4\nu)\left[-(1 - \nu)\rho^2 + \nu(z + z_0)^2\right]}{R^{*5}} - \frac{6(z + z_0)\left[z + \nu(4z + z_0)\right]}{R^{*5}} \\ & + \frac{30z(z + z_0)\left[(1 - \nu)\rho^2 + \nu(z + z_0)^2\right]}{R^{*7}} \Bigg) \\ = \tau^I_{\rho\rho}(\rho, z) + \frac{2\mu}{3(1 - 2\nu)}\epsilon_1 a^3 \Bigg(& \frac{3 - 5\nu + 4\nu^2}{R^{*3}} \\ & + \frac{3(3 - 4\nu)\left[-(1 - \nu)\rho^2 + \nu(z + z_0)^2\right]}{R^{*5}} - \frac{6(z + z_0)\left[z + \nu(4z + z_0)\right]}{R^{*5}} \\ & + \frac{30z(z + z_0)\left[(1 - \nu)\rho^2 + \nu(z + z_0)^2\right]}{R^{*7}} - \frac{3(1 + \nu)}{a^3}\frac{\epsilon_0}{\epsilon_1} \Bigg). \end{aligned} \tag{2.41}$$

From eq. (1.42), one can compute $\tau_{\varphi\varphi}$ as follows:

$$\tau_{\varphi\varphi} = \frac{2\mu}{1-2\nu}\begin{cases}(1-\nu)\epsilon_{\varphi\varphi} + \nu(\epsilon_{\rho\rho}+\epsilon_{zz}) - (1+\nu)\epsilon_0 & \text{if } R < a \\ (1-\nu)\epsilon_{\varphi\varphi} + \nu(\epsilon_{\rho\rho}+\epsilon_{zz}) & \text{if } R \geq a\end{cases}. \tag{2.42}$$

The result for $R < a$ is the following:

$$\begin{aligned}\tau_{\varphi\varphi}(\rho,z) &= \frac{2\mu}{3(1-2\nu)}\epsilon_1 a^3\left(\frac{1+\nu}{a^3} + \frac{3-5\nu+4\nu^2}{R^{*3}} - \frac{6(z+z_0)\left[(1-\nu)z+\nu z_0\right]}{R^{*5}}\right. \\ &\qquad \left. + \frac{3\nu(3-4\nu)\left[(z+z_0)^2-\rho^2\right]}{R^{*5}} - \frac{3(1+\nu)}{a^3}\frac{\epsilon_0}{\epsilon_1}\right) \\ &= \tau^I_{\varphi\varphi}(\rho,z) + \frac{2\mu}{3(1-2\nu)}\epsilon_1 a^3\left(\frac{3-5\nu+4\nu^2}{R^{*3}} - \frac{6(z+z_0)\left[(1-\nu)z+\nu z_0\right]}{R^{*5}}\right. \\ &\qquad \left. + \frac{3\nu(3-4\nu)\left[(z+z_0)^2-\rho^2\right]}{R^{*5}} - \frac{3(1+\nu)}{a^3}\frac{\epsilon_0}{\epsilon_1}\right),\end{aligned} \tag{2.43}$$

and for $R \geq a$ is:

$$\begin{aligned}\tau_{\varphi\varphi}(\rho,z) &= \frac{2\mu}{3(1-2\nu)}\epsilon_1 a^3\left(\frac{1-2\nu}{R^3} + \frac{3-5\nu+4\nu^2}{R^{*3}} - \frac{6(z+z_0)\left[(1-\nu)z+\nu z_0\right]}{R^{*5}}\right. \\ &\qquad \left. + \frac{3\nu(3-4\nu)\left[(z+z_0)^2-\rho^2\right]}{R^{*5}}\right) \\ &= \tau^I_{\varphi\varphi}(\rho,z) + \frac{2\mu}{3(1-2\nu)}\epsilon_1 a^3\left(\frac{3-5\nu+4\nu^2}{R^{*3}} - \frac{6(z+z_0)\left[(1-\nu)z+\nu z_0\right]}{R^{*5}}\right. \\ &\qquad \left. + \frac{3(3-4\nu)\left[(z+z_0)^2-\rho^2\right]}{R^{*5}} - \frac{3\nu(1+\nu)}{a^3}\frac{\epsilon_0}{\epsilon_1}\right).\end{aligned} \tag{2.44}$$

2.3 Expressions of displacement, stress and strain components for a spherical shell shaped source

We can apply the procedure described in section (2.1) and in the Appendix B to a spherical TPE shell enclosing a fluid-like spherical reservoir of radius a and internal pressure P_0 (i.e., a Mogi source that can represent a magmatic chamber), bounded by a spherical surface of radius $b > a$. As done in section (2.1), the results expressed in section (1.3) can be written in cylindrical coordinates (ρ, φ, z). The adopted reference system is that centered on the free surface $z = 0$ and with the z axis oriented in the direction of increasing depth. Hence, the TPE source center is placed at $z = +z_0$ and, in cylindrical coordinates, by defining with $R(\rho,z) \doteq (\rho^2 + (z-z_0)^2)^{1/2}$, the expression of the non-vanishing components of the displacement field, expressed in eq. (1.64), are the following:

$$u^I_z(\rho,z) = \begin{cases}\frac{P_0 a^3}{4\mu}\frac{z-z_0}{R^3} + \frac{1}{3}\epsilon_1(z-z_0)\left(1-\frac{a^3}{R^3}\right) & \text{if } a \leq R \leq b \\ \frac{P_0 a^3}{4\mu}\frac{z-z_0}{R^3} + \frac{1}{3}\epsilon_1(z-z_0)\frac{b^3-a^3}{R^3} & \text{if } R > b\end{cases}; \tag{2.45}$$

$$u^I_\rho(\rho,z) = \begin{cases}\frac{P_0 a^3}{4\mu}\frac{\rho}{R^3} + \frac{1}{3}\epsilon_1\rho\left(1-\frac{a^3}{R^3}\right) & \text{if } a \leq R \leq b \\ \frac{P_0 a^3}{4\mu}\frac{\rho}{R^3} + \frac{1}{3}\epsilon_1\rho\frac{b^3-a^3}{R^3} & \text{if } R > b\end{cases}. \tag{2.46}$$

In Fig. (2.2) I introduce the source parameters and cartesian coordinates.

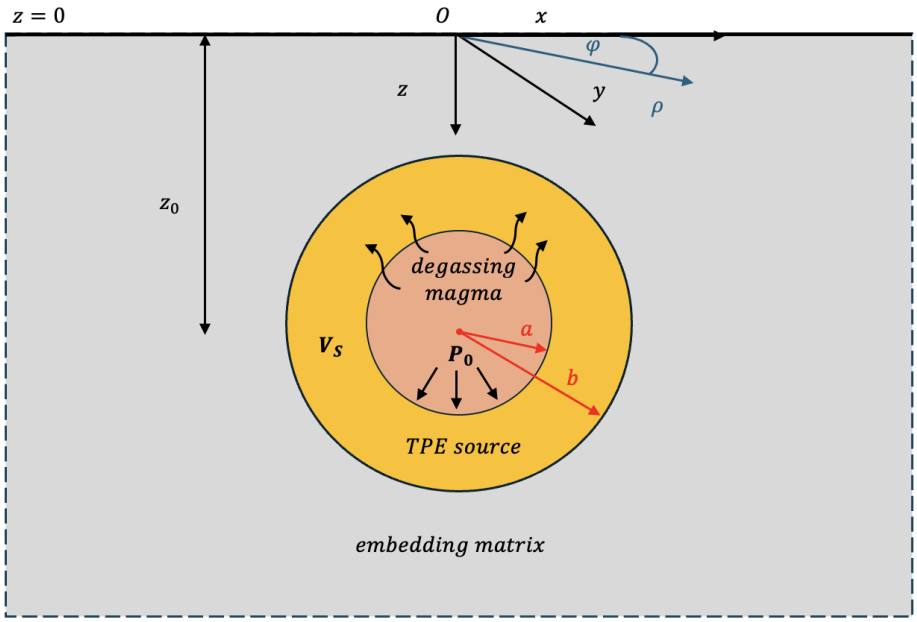

Figure 2.2: *Spherical shell TPE region (yellow) of inner radius a and outer radius b surrounded by an embedding matrix (gray) in drained isothermal conditions. The reference system, in cartesian (black) coordinates (x, y, z) and cylindrical (blue) coordinates (ρ, φ, z), is also represented. The origin of the reference system lies on the free surface ($z = 0$) and the $z-$axis is taken positive in the downward direction. The center of the median plane of the TPE shell is located at $(0; 0; z_0)$.*

In Appendix A.2 we computed the expressions of the non-vanishing stress components generated by the spherical shell TPE inclusion in an unbounded medium.
In order to remove the shear components of stress in $z = 0$ it is necessary to introduce an image source located in $z = -z_0$. By defining $R^*(\rho, z) = (\rho^2 + (z + z_0)^2)^{3/2}$, in cylindrical coordinates, the displacement's components in eqq. (2.45) and (2.46) assume the form as follows:

$$u_z^{II}(\rho, z) = \begin{cases} \frac{P_0 a^3}{4\mu}\left(\frac{z-z_0}{R^3} + \frac{z+z_0}{R^{*3}}\right) + \frac{1}{3}\epsilon_1\left[\left(1 - \frac{a^3}{R^3}\right)(z - z_0) + \frac{b^3-a^3}{R^{*3}}(z + z_0)\right] & \text{if } a \le R \le b \\ \frac{P_0 a^3}{4\mu}\left(\frac{z-z_0}{R^3} + \frac{z+z_0}{R^{*3}}\right) + \frac{1}{3}\epsilon_1(b^3 - a^3)\left(\frac{z-z_0}{R^3} + \frac{z+z_0}{R^{*3}}\right) & \text{if } R > b \end{cases}; \tag{2.47}$$

$$u_\rho^{II}(\rho, z) = \begin{cases} \frac{P_0 a^3}{4\mu}\rho\left(\frac{1}{R^3} + \frac{1}{R^{*3}}\right) + \frac{1}{3}\epsilon_1\rho\left(1 - \frac{a^3}{R^3} + \frac{b^3-a^3}{R^{*3}}\right) & \text{if } a \le R \le b \\ \frac{P_0 a^3}{4\mu}\rho\left(\frac{1}{R^3} + \frac{1}{R^{*3}}\right) + \frac{1}{3}\epsilon_1\rho(b^3 - a^3)\left(\frac{1}{R^3} + \frac{1}{R^{*3}}\right) & \text{if } R > b \end{cases}. \tag{2.48}$$

In order to remove the stress component τ_{zz}^{II} in $z = 0$ it is necessary to add the solution, denoted with the apex "Z", of the elastic problem in a half-space with the imposed boundary condition $\tau_{\rho z} = \tau_{\varphi z}$, $\tau_{zz} = -\tau_{zz}^{II}$ in $z = 0$ to the same solution with apex "II", similarly to what I showed in section (2.1).
To this aim, we have to compute τ_{zz}^{II} outside the source. From eq. (1.42) and eq. (2.47) we get:

$$\begin{aligned} \tau_{zz}^{II} = &-\frac{P_0 a^3}{2}\left(-\frac{1}{R^3} + \frac{3(z - z_0)^2}{R^5} - \frac{1}{R^{*3}} + \frac{3(z + z_0)^2}{R^{*5}}\right) \\ &- \frac{2}{3}\mu\epsilon_1(b^3 - a^3)\left(-\frac{1}{R^3} + \frac{3(z - z_0)^2}{R^5} - \frac{1}{R^{*3}} + \frac{3(z + z_0)^2}{R^{*5}}\right). \end{aligned} \tag{2.49}$$

By applying the same procedure as carried out in section (2.1) it is possible to obtain the expressions of u_ρ^Z and u_z^Z:

$$u_z^Z(\rho,z) = -\left(\frac{P_0a^3}{2\mu}+\frac{2}{3}\epsilon_1(b^3-a^3)\right)\left(2(1-\nu)\frac{z+z_0}{R^{*3}}-\frac{z}{R^{*3}}+\frac{3z(z+z_0)^2}{R^{*5}}\right); \tag{2.50}$$

$$u_\rho^Z(\rho,z) = \left(\frac{P_0a^3}{2\mu}+\frac{2}{3}\epsilon_1(b^3-a^3)\right)\left(\frac{(1-2\nu)\rho}{R^{*3}}-\frac{3\rho z(z+z_0)}{R^{*5}}\right). \tag{2.51}$$

2.3.1 Displacement components

Now we are able to compute the expressions of the total displacement $u_z = u_z^{II} + u_z^Z$ and $u_\rho = u_\rho^{II} + u_\rho^Z$.
Starting with u_z, for $a \le R \le b$ we get:

$$\begin{aligned} u_z(\rho,z) = {} & \frac{P_0a^3}{4\mu}\left(\frac{z-z_0}{R^3}+\frac{z+z_0}{R^{*3}}\right)+\frac{1}{3}\epsilon_1\left[\left(1-\frac{a^3}{R^3}\right)(z-z_0)+\frac{b^3-a^3}{R^{*3}}(z+z_0)\right]- \\ & -\left(\frac{P_0a^3}{2\mu}+\frac{2}{3}\epsilon_1(b^3-a^3)\right)\left(\frac{2(1-\nu)(z+z_0)}{R^{*3}}-\frac{z}{R^{*3}}+\frac{3z(z+z_0)^2}{R^{*5}}\right), \end{aligned} \tag{2.52}$$

and for $R > b$ we get:

$$u_z(\rho,z) = \left(\frac{P_0a^3}{4\mu}+\frac{1}{3}\epsilon_1(b^3-a^3)\right)\left(\frac{z-z_0}{R^3}-(3-4\nu)\frac{z+z_0}{R^{*3}}+\frac{2z}{R^{*3}}-\frac{6z(z+z_0)^2}{R^{*5}}\right). \tag{2.53}$$

The other component, u_ρ, for $a \le R \le b$ is:

$$\begin{aligned} u_\rho(\rho,z) = {} & \frac{P_0a^3}{4\mu}\rho\left(\frac{1}{R^3}+\frac{1}{R^{*3}}\right)+\frac{1}{3}\epsilon_1\rho\left[1-\frac{a^3}{R^3}+\frac{b^3-a^3}{R^{*3}}\right]+ \\ & +\left(\frac{P_0a^3}{2\mu}+\frac{2}{3}\epsilon_1(b^3-a^3)\right)\rho\left(\frac{1-2\nu}{R^{*3}}-\frac{3z(z+z_0)}{R^{*5}}\right), \end{aligned} \tag{2.54}$$

and for $R > b$ we get:

$$u_\rho(\rho,z) = \left(\frac{P_0a^3}{4\mu}+\frac{1}{3}\epsilon_1(b^3-a^3)\right)\rho\left(\frac{1}{R^3}+\frac{3-4\nu}{R^{*3}}-\frac{6z(z+z_0)}{R^{*5}}\right). \tag{2.55}$$

As in the case of the sphere, the displacement field is not irrotational and therefore cannot be expressed by a scalar potential.

2.3.2 Strain components

From the displacement expression it is possible to determine the strain components ϵ_{ij}. As in section (2.2.2) the components $\epsilon_{\varphi\rho}$ and $\epsilon_{\varphi z}$ are identically null.
The diagonal component $\epsilon_{\rho\rho}$, calculable by eq. (2.25), for $a \le R \le b$ is given by:

$$\begin{aligned} \epsilon_{\rho\rho}(\rho,z) = {} & \frac{P_0a^3}{4\mu}\left(\frac{1}{R^3}+\frac{1}{R^{*3}}-3\rho^2\left(\frac{1}{R^5}+\frac{1}{R^{*5}}\right)\right) \\ & +\frac{1}{3}\epsilon_1\left(1-\frac{a^3}{R^3}+\frac{b^3-a^3}{R^{*3}}+3\rho^2\left(\frac{a^3}{R^5}-\frac{b^3-a^3}{R^{*5}}\right)\right)+ \\ & +\left(\frac{P_0a^3}{2\mu}+\frac{2}{3}\epsilon_1(b^3-a^3)\right)\left(\frac{1-2\nu}{R^{*3}}-\frac{3z(z+z_0)}{R^{*5}}-\frac{3(1-2\nu)\rho^2}{R^{*5}}\right. \\ & \left.+\frac{15z(z+z_0)\rho^2}{R^{*7}}\right), \end{aligned} \tag{2.56}$$

and for $R > b$ we get:

$$\epsilon_{\rho\rho}(\rho,z) = \left(\frac{P_0 a^3}{4\mu} + \frac{1}{3}\epsilon_1(b^3-a^3)\right)\left(\frac{1}{R^3} + \frac{3-4\nu}{R^{*3}} - 3\frac{\rho^2}{R^5} - 3(3-4\nu)\frac{\rho^2}{R^{*5}} - \frac{6z(z+z_0)}{R^{*5}} + \frac{30\rho^2 z(z+z_0)}{R^{*7}}\right) \tag{2.57}$$

The diagonal component $\epsilon_{\varphi\varphi}$, calculable by eq. (2.27), for $a \leq R \leq b$ is given by:

$$\epsilon_{\varphi\varphi}(\rho,z) = \frac{P_0 a^3}{4\mu}\left(\frac{1}{R^3} + \frac{1}{R^{*3}}\right) + \frac{1}{3}\epsilon_1\left(1 - \frac{a^3}{R^3} + \frac{b^3-a^3}{R^{*3}}\right) + \left(\frac{P_0 a^3}{2\mu} + \frac{2}{3}\epsilon_1(b^3-a^3)\right)\left(\frac{1-2\nu}{R^{*3}} - \frac{3z(z+z_0)}{R^{*5}}\right), \tag{2.58}$$

and for $R > b$ we get:

$$\epsilon_{\varphi\varphi}(\rho,z) = \left(\frac{P_0 a^3}{4\mu} + \frac{1}{3}\epsilon_1(b^3-a^3)\right)\left(\frac{1}{R^3} + \frac{3-4\nu}{R^{*3}} - \frac{6z(z+z_0)}{R^{*5}}\right). \tag{2.59}$$

The other diagonal component ϵ_{zz}, calculable by eq. (2.29), for $a \leq R \leq b$ is given by:

$$\begin{aligned}\epsilon_{zz}(\rho,z) = {} & \frac{P_0 a^3}{4\mu}\left(\frac{1}{R^3} + \frac{1}{R^{*3}} - \frac{3(z-z_0)^2}{R^5} - \frac{3(z+z_0)^2}{R^{*5}}\right) \\ & + \frac{1}{3}\epsilon_1\left(1 - \frac{a^3}{R^3} + \frac{b^3-a^3}{R^{*3}} + 3a^3\frac{(z-z_0)^2}{R^5} - 3(b^3-a^3)\frac{(z+z_0)^2}{R^{*5}}\right) - \left(\frac{P_0 a^3}{2\mu}\right. \\ & \left. + \frac{2}{3}\epsilon_1(b^3-a^3)\right)\left(\frac{1-2\nu}{R^{*3}} - \frac{3(1-2\nu)(z+z_0)^2}{R^{*5}} + \frac{9z(z+z_0)}{R^{*5}} - \frac{15z(z+z_0)^3}{R^{*7}}\right),\end{aligned} \tag{2.60}$$

and for $R > b$ we get:

$$\epsilon_{zz}(\rho,z) = \left(\frac{P_0 a^3}{4\mu} + \frac{1}{3}\epsilon_1(b^3-a^3)\right)\left(\frac{1}{R^3} - \frac{1-4\nu}{R^{*3}} - \frac{3(z-z_0)^2}{R^5} + 3(1-4\nu)\frac{(z+z_0)^2}{R^{*5}} - \frac{18z(z+z_0)}{R^{*5}} + \frac{30z(z+z_0)^3}{R^{*7}}\right). \tag{2.61}$$

The only non-vanishing non-diagonal component is $\epsilon_{\rho z}$, and it can be determined through eq. (2.31):

$$\epsilon_{\rho z}(\rho,z) = -\frac{3P_0 a^3}{4\mu}\rho\left(\frac{z-z_0}{R^5} + \frac{z+z_0}{R^{*5}}\right)\epsilon_1\rho\left(\frac{a^3(z-z_0)}{R^5} - \frac{(b^3-a^3)(z+z_0)}{R^{*5}}\right) + \left(\frac{P_0 a^3}{4\mu} + \frac{1}{3}\epsilon_1(b^3-a^3)\right)\rho\left(-\frac{6z}{R^{*5}} + \frac{30z(z+z_0)^2}{R^{*7}}\right), \tag{2.62}$$

and for $R > b$ we get:

$$\epsilon_{\rho z}(\rho,z) = -3\left(\frac{P_0 a^3}{4\mu} + \frac{1}{3}\epsilon_1(b^3-a^3)\right)\rho\left(\frac{z-z_0}{R^5} + \frac{z+z_0}{R^{*5}} + \frac{2z}{R^{*5}} - \frac{10z(z+z_0)^2}{R^{*7}}\right). \tag{2.63}$$

2.3.3 Stress components

The stress field in the source region V_s and in the embedding matrix is still given by eq. (1.42).
In particular, from eq. (1.42), one can compute τ_{zz} for the spherical shell TPE as follows:

$$\tau_{zz} = \frac{2\mu}{1-2\nu}\begin{cases}(1-\nu)\epsilon_{zz} + \nu(\epsilon_{\rho\rho}+\epsilon_{\varphi\varphi}) - (1+\nu)\epsilon_0 & \text{if } a \le R \le b \\ (1-\nu)\epsilon_{zz} + \nu(\epsilon_{\rho\rho}+\epsilon_{\varphi\varphi}) & \text{if } R > b\end{cases}. \tag{2.64}$$

The result for $a \le R \le b$ is the following:

$$\begin{aligned}\tau_{zz}(\rho,z) = \frac{2\mu}{1-2\nu}\Bigg\{&\frac{P_0 a^3}{4\mu}\Bigg[(1+\nu)\left(\frac{1}{R^3}+\frac{1}{R^{*3}}\right) \\ &- 3\left(\frac{\nu\rho^2+(1-\nu)(z-z_0)^2}{R^5}+\frac{\nu\rho^2+(1-\nu)(z+z_0)^2}{R^{*5}}\right)\Bigg] \\ &+\frac{1}{3}\epsilon_1\Bigg[(1+\nu)\left(1-\frac{a^3}{R^3}\right)+(1+\nu)\frac{b^3-a^3}{R^{*3}}+3a^3\frac{\nu\rho^2+(1-\nu)(z-z_0)^2}{R^5} \\ &- 3(b^3-a^3)\frac{\nu\rho^2+(1-\nu)(z+z_0)^2}{R^{*5}}\Bigg] \\ &+\left(\frac{P_0 a^3}{2\mu}+\frac{2}{3}\epsilon_1(b^3-a^3)\right)\left(\frac{(3\nu-1)(1-2\nu)}{R^{*3}}+3(1-2\nu)\frac{(1-\nu)(z+z_0)^2-\nu\rho^2}{R^{*5}}\right. \\ &\left.- 3(3-\nu)\frac{z(z+z_0)}{R^{*5}}+15z(z+z_0)\frac{\nu\rho^2+(1-\nu)(z+z_0)^2}{R^{*7}}\right)-(1+\nu)\epsilon_0\Bigg\},\end{aligned} \tag{2.65}$$

and for $R > b$:

$$\begin{aligned}\tau_{zz}(\rho,z) = \frac{2\mu}{1-2\nu}&\left(\frac{P_0 a^3}{4\mu}+\frac{1}{3}\epsilon_1(b^3-a^3)\right)\left(\frac{1+\nu}{R^3}+\frac{1+\nu}{R^{*3}}+\frac{2(3-\nu)(1-2\nu)}{R^{*3}}\right. \\ &- 3\frac{\nu\rho^2+(1-\nu)(z-z_0)^2}{R^5}-3\frac{\nu\rho^2+(1-\nu)(z+z_0)^2}{R^{*5}} \\ &+6(1-2\nu)\frac{(1+\nu)(z+z_0)^2-\nu\rho^2}{R^{*5}}+6(\nu-3)\frac{z(z+z_0)}{R^{*5}} \\ &\left.+30z(z+z_0)\frac{\nu\rho^2+(1-\nu)(z+z_0)^2}{R^{*7}}\right).\end{aligned} \tag{2.66}$$

The non-diagonal component $\tau_{\rho z}$ can be computed, from eq. (1.42), by:

$$\tau_{\rho z} = 2\mu\begin{cases}\epsilon_{\rho z} & \text{if } a \le R \le b \\ \epsilon_{\rho z} & \text{if } R > b\end{cases}. \tag{2.67}$$

The result for $a \le R \le b$ is the following:

$$\begin{aligned}\tau_{\rho z}(\rho,z) = &-\frac{3P_0 a^3}{2}\rho\left(\frac{z-z_0}{R^5}+\frac{z+z_0}{R^{*5}}\right)+2\mu\epsilon_1\rho\left(\frac{a^3(z-z_0)}{R^5}-(b^3-a^3)\frac{z+z_0}{R^{*5}}\right) \\ &+6\left(\frac{P_0 a^3}{2}+\frac{2}{3}\mu\epsilon_1(b^3-a^3)\right)\rho\left(-\frac{z}{R^{*5}}+\frac{5z(z+z_0)^2}{R^{*7}}\right),\end{aligned} \tag{2.68}$$

and for $R > b$ is:

$$\tau_{\rho z}(\rho,z) = -\left(\frac{3P_0a^3}{2}+2\mu\epsilon_1(b^3-a^3)\right)\rho\left(\frac{z-z_0}{R^5}+\frac{z+z_0}{R^{*5}}+\frac{2z}{R^{*5}}-\frac{10z(z+z_0)^2}{R^{*7}}\right). \quad (2.69)$$

The diagonal component $\tau_{\rho\rho}$ can be calculated, from eq. (1.42), by:

$$\tau_{\rho\rho} = \frac{2\mu}{1-2\nu}\begin{cases}(1-\nu)\epsilon_{\rho\rho}+\nu(\epsilon_{\varphi\varphi}+\epsilon_{zz})-(1+\nu)\epsilon_0 & \text{if } a\le R\le b\\ (1-\nu)\epsilon_{\rho\rho}+\nu(\epsilon_{\varphi\varphi}+\epsilon_{zz}) & \text{if } R>b\end{cases}. \quad (2.70)$$

The result for $a \le R \le b$ is the following:

$$\begin{aligned}\tau_{\rho\rho}(\rho,z) = \frac{2\mu}{1-2\nu}\Bigg\{&\frac{P_0a^3}{4\mu}\Bigg[(1+\nu)\left(\frac{1}{R^3}+\frac{1}{R^{*3}}\right)\\ &-3\left(\frac{(1-\nu)\rho^2+\nu(z-z_0)^2}{R^5}+\frac{(1-\nu)\rho^2+\nu(z+z_0)^2}{R^{*5}}\right)\Bigg]\\ &+\frac{1}{3}\epsilon_1\Bigg[(1+\nu)\left(1-\frac{a^3}{R^3}\right)+(1+\nu)\frac{b^3-a^3}{R^{*3}}\\ &+3a^3\left(\frac{(1-\nu)\rho^2+\nu(z-z_0)^2}{R^5}-(b^3-a^3)\frac{(1-\nu)\rho^2+\nu(z+z_0)^2}{R^{*5}}\right)\Bigg]\\ &+\left(\frac{P_0a^3}{2\mu}+\frac{2}{3}\epsilon_1(b^3-a^3)\right)\Bigg(\frac{(1-\nu)(1-2\nu)}{R^{*3}}-3(1+3\nu)\frac{z(z+z_0)}{R^{*5}}\\ &+3(1-2\nu)\frac{-(1-\nu)\rho^2+\nu(z+z_0)^2}{R^{*5}}+15z(z+z_0)\frac{(1-\nu)\rho^2+\nu(z+z_0)^2}{R^{*7}}\Bigg)\\ &-(1+\nu)\epsilon_0\Bigg\},\end{aligned} \quad (2.71)$$

and for $R > b$ is:

$$\begin{aligned}\tau_{\rho\rho}(\rho,z) = \frac{2\mu}{1-2\nu}&\left(\frac{P_0a^3}{4\mu}+\frac{1}{3}\epsilon_1(b^3-a^3)\right)\Bigg(\frac{1+\nu}{R^3}+\frac{1+\nu}{R^{*3}}+2\frac{(1-\nu)(1-2\nu)}{R^{*3}}\\ &-3\frac{(1-\nu)\rho^2+\nu(z-z_0)^2}{R^5}-3(1-2\nu)\frac{(1-\nu)\rho^2+\nu(z+z_0)^2}{R^{*5}}\\ &-6(1+3\nu)\frac{z(z+z_0)}{R^{*5}}+3(1-2\nu)\frac{-(1-\nu)\rho^2+\nu(z+z_0)^2}{R^{*5}}\\ &+30z(z+z_0)\frac{(1-\nu)\rho^2+\nu(z+z_0)^2}{R^{*7}}\Bigg).\end{aligned} \quad (2.72)$$

From eq. (1.42), one can compute $\tau_{\varphi\varphi}$ as follows:

$$\tau_{\varphi\varphi} = \frac{2\mu}{1-2\nu}\begin{cases}(1-\nu)\epsilon_{\varphi\varphi}+\nu(\epsilon_{\rho\rho}+\epsilon_{zz})-(1+\nu)\epsilon_0 & \text{if } a\le R\le b\\ (1-\nu)\epsilon_{\varphi\varphi}+\nu(\epsilon_{\rho\rho}+\epsilon_{zz}) & \text{if } R>b\end{cases}. \quad (2.73)$$

The result for $a \leq R \leq b$ is the following:

$$\tau_{\varphi\varphi}(\rho,z) = 2\mu\left[\frac{P_0 a^3}{4\mu}\left(\frac{1}{R^3}+\frac{1}{R^{*3}}\right)+\frac{1}{3}\epsilon_1\left(\frac{1+\nu}{1-2\nu}-\frac{a^3}{R^3}+\frac{b^3-a^3}{R^{*3}}\right)\right.$$
$$+\left(\frac{P_0 a^3}{2\mu}+\frac{2}{3}\epsilon_1(b^3-a^3)\right)\left(\frac{1-\nu}{R^{*3}}-\frac{3}{1-2\nu}\frac{z(z+z_0)}{R^{*5}}+3\nu\frac{(z+z_0)^2-\rho^2}{R^{*5}}\right.$$
$$\left.\left.+\frac{6\nu}{1-2\nu}\frac{z(z+z_0)}{R^{*5}}\right)-\frac{1+\nu}{1-2\nu}\epsilon_0\right], \tag{2.74}$$

and for $R > b$ is:

$$\tau_{\varphi\varphi}(\rho,z) = 2\mu\left(\frac{P_0 a^3}{4\mu}+\frac{1}{3}\epsilon_1(b^3-a^3)\right)\left(\frac{1}{R^3}-\frac{4\nu^2-5\nu+3}{1-2\nu}\frac{1}{R^{*3}}-\frac{6z(z+z_0)}{R^{*5}}\right.$$
$$\left.+\frac{3\nu}{1-2\nu}\frac{(1-4\nu)(z+z_0)^2-(3-4\nu)\rho^2}{R^{*5}}\right). \tag{2.75}$$

2.3.4 Spherical shell TPE inclusions vs. Mogi sources

As previously mentioned, the solutions for displacement, strain and stress for a Mogi source centered at $z = z_0$, with radius b and overpressure ΔP, can be obtained by replacing, in the equations derived in sections (2.3.1); (2.3.2); (2.3.3), P_0 with ΔP, a with b, and setting $\epsilon_1 = 0$.
By defining $R_1 = \sqrt{\rho^2 + z_0^2}$, the surface displacement components of the Mogi source (denoted with superscript "m") are given by:

$$u_z^m(\rho,0) = \frac{\Delta P b^3}{4\mu}\left[-4(1-\nu)\frac{z_0}{R_1^3}\right]; \tag{2.76}$$

$$u_\rho^m(\rho,0) = \frac{\Delta P b^3}{4\mu}\left[4(1-\nu)\frac{\rho}{R_1^3}\right]. \tag{2.77}$$

From eqq. (2.53) and (2.55), by substituting P_0 with $P_0 - P_m$ (to consider the incremental field, as discussed in section 1.3.4), the surface displacement components generated by the spherical shell with inner radius a and outer radius b are:

$$u_z(\rho,0) = \left[\frac{(P_0-P_m)b^3}{4\mu}+\frac{1}{3}\epsilon_1(b^3-a^3)\right]\left[-4(1-\nu)\frac{z_0}{R_1^3}\right]; \tag{2.78}$$

$$u_\rho(\rho,0) = \left[\frac{(P_0-P_m)b^3}{4\mu}+\frac{1}{3}\epsilon_1(b^3-a^3)\right]\left[4(1-\nu)\frac{\rho}{R_1^3}\right]. \tag{2.79}$$

It can be observed that the terms inside the second brackets are identical for both the shell and the Mogi source. Therefore, the surface displacement expressions of the shell match those of the Mogi source when the overpressure satisfies:

$$\Delta P = (P_0 - P_m) + \frac{4}{3}\mu\epsilon_1\frac{b^3-a^3}{b^3}. \tag{2.80}$$

Similarly, since the dependence on ϵ_1 of all the stress and strain components appears only in the first factor, the second factor remains identical for both the Mogi source and

the shell. Hence, the relationship in eq. (2.80) applies to all components of displacement, strain, and stress.
In the special case where the pressure inside the magma chamber does not change during degassing (i.e., $P_0 = P_m$), we obtain the simplified relation:

$$\Delta P = \frac{4}{3}\mu\epsilon_1 \frac{b^3 - a^3}{b^3}. \tag{2.81}$$

Similarly, all these considerations also hold for a spherical TPE source, which is obtained by setting the inner radius of the shell to $a = 0$.

Chapter 3

Results

This chapter presents the results obtained from the analysis carried out in the previous sections. In particular, maps have been produced to illustrate the distribution of displacement, stress, and strain components on the plane $y = 0$ (Fig. 2.1) so that $\rho = |x|$. The distribution of the maximum shear stress and the Coulomb Failure Function is also shown. Two source configurations have been analyzed: a spherical source centered at a depth of 1000 m, and another at 5000 m. For both cases, the difference between the results obtained in a half-space and those in a full-space configuration have been evaluated. The presentation of results begins with the displacement field, which represents the primary quantity obtained from the solution of the thermo-poro-elastic model. From the computed displacements, both the strain and stress fields are derived through standard and constitutive relations. Among these derived fields, the stress is presented first. The strain field is then analyzed to provide a complementary view of the deformation pattern, quantifying local changes in shape and volume.
In addition, graphs have been produced to show the percentage variation in maximum shear stress between the full-space and half-space models at a point just outside the source, as functions of depth. This allows identification of the depth beyond which the difference between the two models becomes negligible (within 15%). This is because, for a sufficiently deep source, the solutions in a full space and in a half-space are expected to be equivalent, as the effects of the free surface become negligible.
Finally, the distribution of the above quantities has been analyzed along the x-axis on the median plane $z = z_0$ and on the free surface ($z = 0$). The evaluation of stress, displacement, and strain fields at the surface resulting from a TPE source is of critical importance in the geophysical modeling of volcanic and hydrothermal systems. Several reasons justify this focus, for example the direct comparison with geophysical observations and also for hazard assessment and risk mitigation. In this context, theoretical surface fields serve as the primary link between physical models and observations. Accurate computation of these quantities enables the validation and calibration of source models against empirical data.
All of these analyses have also been replicated for the case of a shell-shaped spherical TPE source. The parameter values used in this chapter are given in Tab. (3.1) for the spherical source and in Tab. (3.2) for the spherical shell shaped source.

ν	μ [Pa]	H [Pa]	α [K^{-1}]	p [Pa]	T [K]	a [m]	z_0 [m]
0.25	$6 \cdot 10^9$	$1 \cdot 10^{10}$	$3 \cdot 10^{-5}$	10^6	100	500	1000, 5000

Table 3.1: *Physical parameters used in this chapter to represent the displacement, stress and strain components derived in the previous paragraph in the case of spherical TPE source.*

ν	μ [Pa]	H [Pa]	α [K^{-1}]	p [Pa]	T [K]	P_0 [Pa]	a [m]	b [m]	z_0 [m]
0.25	$6 \cdot 10^9$	$1 \cdot 10^{10}$	$3 \cdot 10^{-5}$	10^6	100	-10^7	200	500	1000, 5000

Table 3.2: *Physical parameters used in this chapter to represent the displacement, stress and strain components derived in the previous paragraph in the case of spherical shell TPE source.*

3.1 Results for a spherical TPE inclusion

3.1.1 Displacement Field

Fig. (3.1a) shows the distribution of u_ρ generated by a spherical TPE inclusion of radius 500 m (this value is kept constant throughout the entire section), located in $z = z_0 = 1000$ m, the expression of which is reported in eq. (2.21). The same component of the displacement field is plotted in Fig. (3.1b) when $z_0 = 5000$ m. It is possible to observe that this component is everywhere positive. As for all components of all fields discussed below, it can be observed that increasing the source depth leads to a greater degree of symmetry with respect to the horizontal axis, which tends toward the behavior of a TPE source in a full space. This highlights the role of the free surface in breaking the symmetry observed near the surface. However, it is important to clarify that the symmetry is always preserved with respect to the vertical axis (i.e., the z-axis). This is a consequence of the cylindrical symmetry of the model, where all fields depend on $\rho = |x|$, and thus are invariant under reflection across the vertical axis. In the figures, also negative values of the horizontal coordinate x are shown. This graphical choice is made solely to enhance the readability of the mechanical field patterns by visually representing the symmetry of the solution with respect to the $z-$axis.
Fig. (3.1c) and Fig. (3.1d) represent the difference Δu_ρ between the radial components evaluated using the half-space solution (eq. 2.21) and the unbounded medium solution (eq. 2.3) for the same source location. The first figure shows that the main difference is positive, with a maximum value of 0.07 m, while the minimum is one order of magnitude smaller. This indicates that the presence of the free surface leads to an increase in the radial displacement component, which is most prominent at the surface. In contrast, the second figure shows that, as the source moves farther from the free surface, the differences become smaller and are not visible within the current color scale. This reduction in difference, which will be similar for all components of all considered fields, is expected: as the source is placed deeper, the influence of the free surface progressively weakens, and the solution tends to that of the full-space case (e.g., Belardinelli et al., 2019). Indeed, the differences here are one order of magnitude smaller than in the case with $z_0 = 1000$ m.

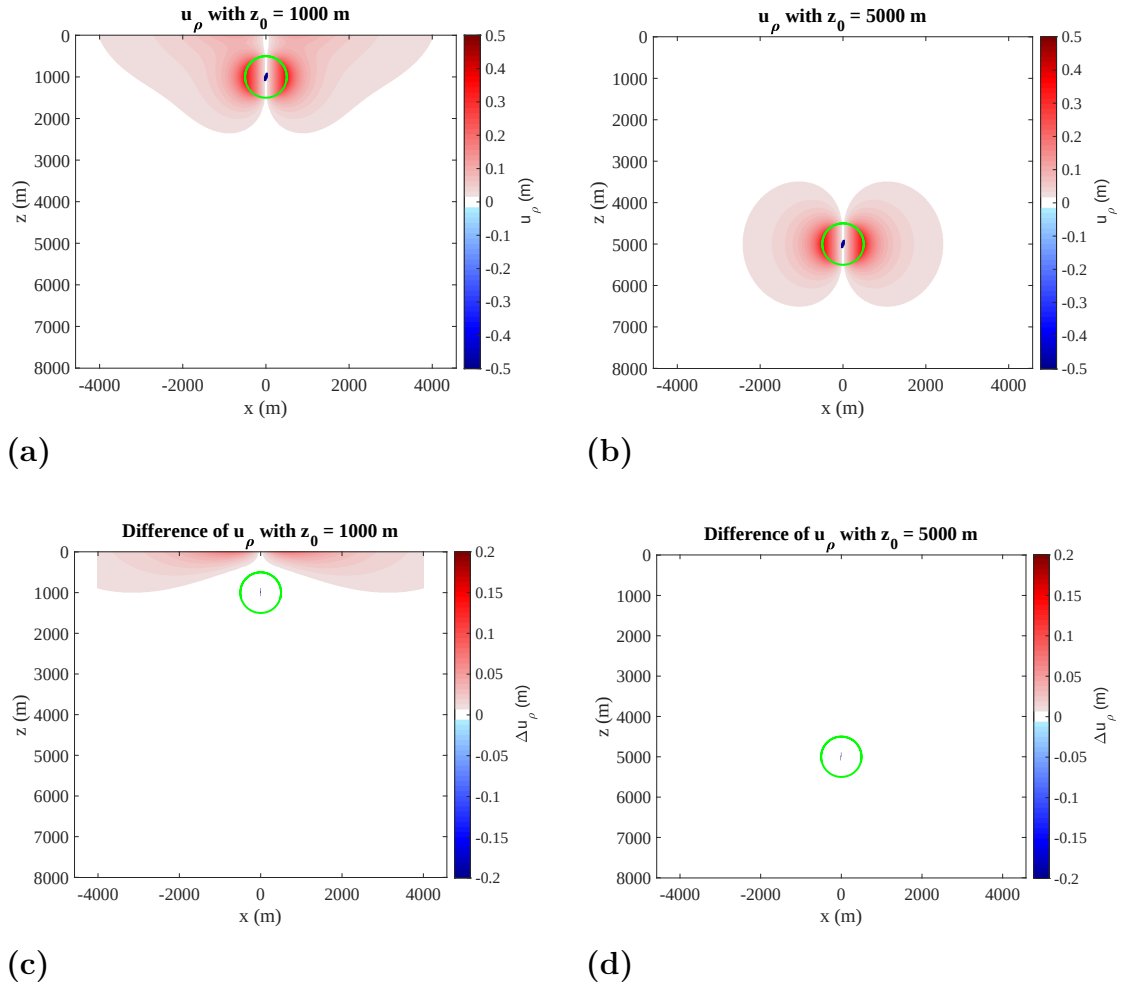

Figure 3.1: *Distribution of u_ρ generated by a spherical TPE inclusion of radius 500 m, with the center located in $z = z_0 = 1000$ m in panel (a) and in $z_0 = 5000$ m in panel (b), in the plane $y = 0$. Panels (c) and (d) show the difference Δu_ρ between the displacement component, u_ρ, respectively generated by the previous considered inclusions, placed in a bounded space (i.e., calculated with the free surface condition) and the same component calculated without that condition. The surface of the sphere is highlighted with a green line. The color bar on the right of the picture represents the magnitude of the physical quantity under consideration. Note the different color scale in panels (a)-(b) and (c)-(d).*

Fig. (3.2a) represents the distribution of u_z generated by a spherical TPE inclusion located in $z = z_0 = 1000$ m, the expression of which is reported in eq. (2.20). Fig. (3.2b) shows the same component of the displacement field is plotted when $z_0 = 5000$ m. It is possible to observe that in the part of the plane corresponding to the upper hemisphere this component is negative (while it is positive in the lower part). Since the positive semi-axis of the z-axis is pointing downward, this indicates an uplift in the upper part, which, in the case depicted in the left panel of the figure, also reaches the free surface. Fig. (3.2c) and Fig. (3.2d) represent the difference Δu_z between the vertical components evaluated using the half-space solution (eq. 2.20) and the unbounded medium solution (eq. 2.2) for the same source location. When the source is located at $z_0 = 1000$ m, the Δu_z is negative or vanishing. Its minimum value, -0.19 m, is one order of magnitude larger than the maximum of Δu_ρ. This leads to the conclusion that the presence of the free surface causes a decrease of u_z compared to the full-space case, with a maximum relative

variation of approximately 37%, reached at the portion of the free surface corresponding to the vertical projection of the source onto this plane ($x \simeq 0$). As stated for Δu_ρ, when $z_0 = 5000$ m the difference is less pronounced, although it still reaches significant values near the free surface, where the minimum of the difference is -0.074 m.

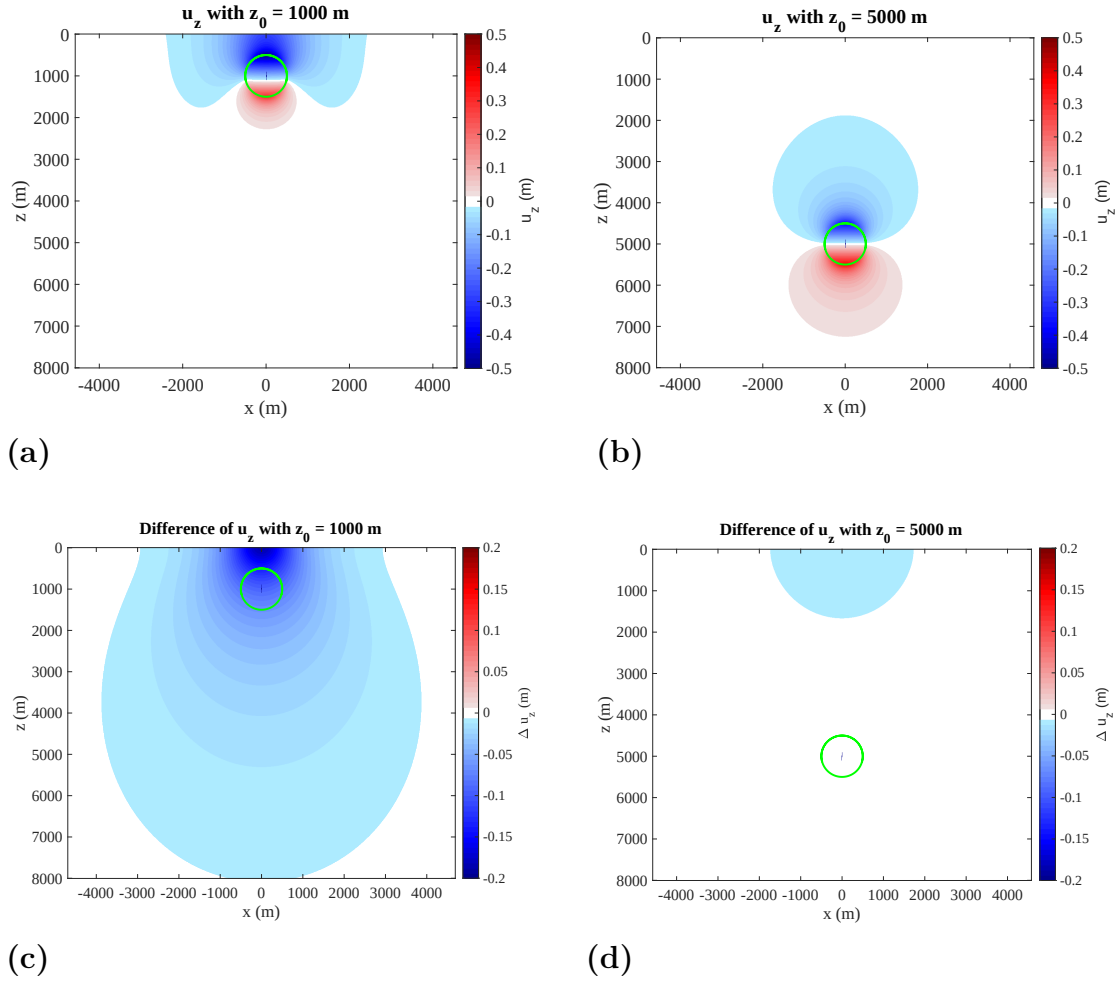

Figure 3.2: *Distribution of u_z generated by a spherical TPE inclusion of radius 500 m, with the center located in $z = z_0 = 1000$ m in panel (a) and in $z_0 = 5000$ m in panel (b), in the plane $y = 0$. Panels (c) and (d) show the difference Δu_z between the displacement component, u_z, respectively generated by the previous considered inclusions, placed in a bounded space (i.e., calculated with the free surface condition) and the same component calculated without that condition. The surface of the sphere is highlighted with a green line. The color bar on the right of the picture represents the magnitude of the physical quantity under consideration. Note the different color scale in panels (a)-(b) and (c)-(d).*

3.1.2 Stress field

Fig. (3.3a) shows the distribution of τ_{zz} and of the displacement generated by a spherical TPE inclusion located in $z = z_0 = 1000$ m, according to eqq. (2.34); (2.35). τ_{zz} satisfies the continuity condition across the TPE surface along the z direction; while it manifests a discontinuity of the first kind along the $x-$axis, moving from a strongly negative value inside the sphere to a positive value in the embedding matrix. The continuity of the normal traction component is expected across the sphere, which is τ_{zz} only when the

surface intersect the $z-$axis. Accordingly, at the intersection with the $x-$axis continuity of $\tau_{\rho\rho}$ component is expected in place of continuity τ_{zz}. It is possible to notice that the effect of the free surface is severe, as the symmetry with respect to $z - z_0 = 0$ is broken. In $z = 0$, due to the free surface condition, the value of τ_{zz} is identically null. Fig. (3.3b) shows that, for a spherical TPE inclusion located at $z = 5000$ m, the effect of the free surface is greatly mitigated, and the symmetry is much more present.
In order to show the difference between the value of τ_{zz} with and without the free surface condition, we can consider Fig. (3.3c). This picture shows the difference, $\Delta\tau_{zz}$, between τ_{zz} in the case of a sphere placed in a half-space and the same component in an unbounded space (eq. A.11). It is possible to notice that there is a prevalent positive difference inside and outside the source, especially in the part of the half-space closer to the free surface. In particular, the maximum value of $\Delta\tau_{zz}$ is $2.58 \cdot 10^6$ Pa, and the minimum value is $-6.05 \cdot 10^4$ Pa (one order of magnitude lower in absolute value). The former is not reached at the free surface, but at the point $(0; 100)$ m. However, the relative difference on the free surface is 100%, while in $(0; 100)$ m is 75%. This is consistent with the fact that the effects of the free surface decrease with increasing depth. We can conclude that the presence of the free surface allows a release of vertical stress above the source, making τ_{zz} less compressive.
Fig. (3.3d) represents the same difference when the center of the sphere is located in $z_0 = 5000$ m. Here, being far from the free surface, the maximum absolute value of the difference is more than two orders of magnitude lower than the result with the free surface condition.

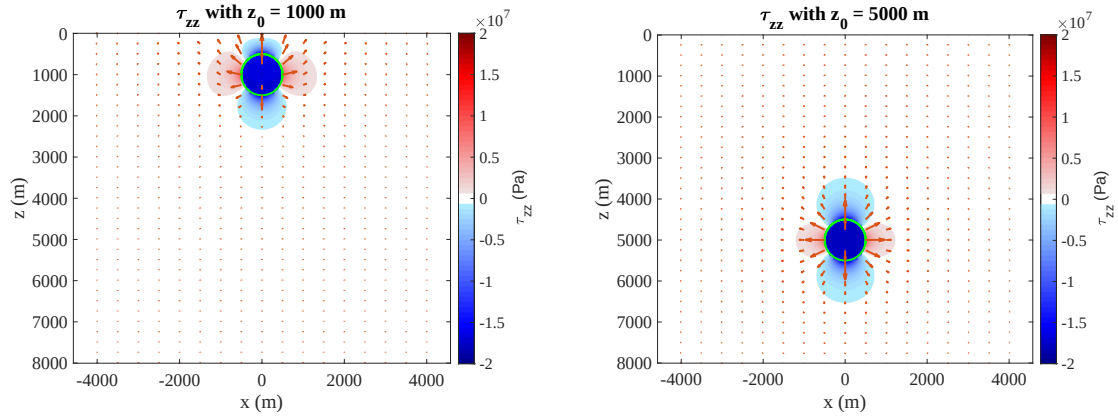

(a) (b)

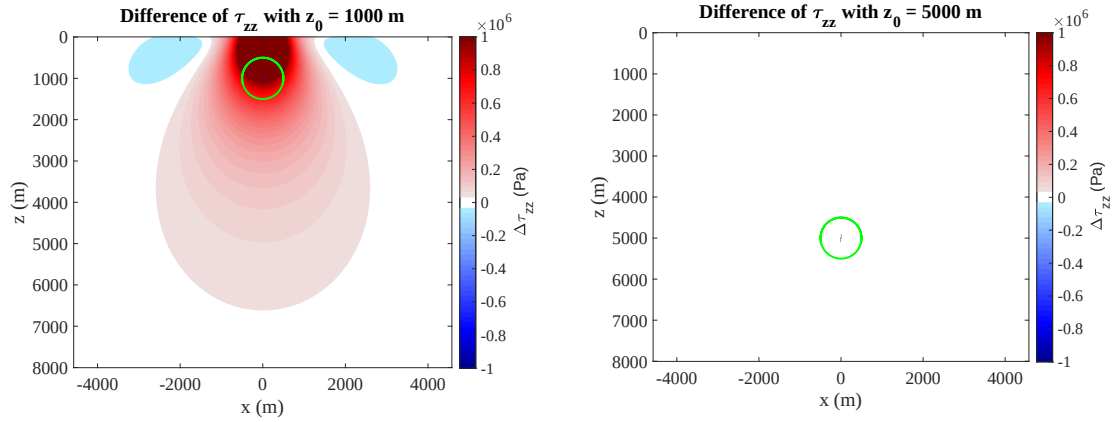

(c) (d)

Figure 3.3: *Distribution of the stress component τ_{zz} generated by a spherical TPE inclusion with a radius of 500 m, which center is located at $z = z_0 = 1000$ m in panel (a) and at $z = z_0 = 5000$ m in panel (b), in the plane $y = 0$. Panels (c) and (d) display the difference $\Delta\tau_{zz}$ between the stress field computed in a bounded domain (i.e., with the free surface condition) and the same component computed in an unbounded domain (i.e., without the free surface). The surface of the spherical inclusion is highlighted by a green line. The color bar to the right indicates the magnitude of the physical quantity shown. The arrows represent the displacement field produced from the TPE inclusion. Note the different color scale in panels (a)-(b) and (c)-(d).*

Fig. (3.4a) represents the distribution of $\tau_{\rho z}$ generated by a spherical TPE inclusion located in $z = z_0 = 1000$ m, the expression of which is reported in eqq. (2.37); (2.38). The value of $\tau_{\rho z}$ inside the sphere is much lower than outside; indeed, using this color bar range it is impossible to appreciate it.
In $z = 0$, due to the free surface condition, the value of $\tau_{\rho z}$ is identically null.
Fig. (3.4b) shows the same component of the stress field, now generated by a sphere located in $z = 5000$ m, so further away from the free surface. In this case it is impossible to evaluate the stress magnitude inside the TPE source because the effect of the free surface is reduced. Furthermore, the symmetry of $\tau_{\rho z}$ is much more present.
To show the difference, $\Delta\tau_{\rho z}$, between the value of $\tau_{\rho z}$ with and without the free surface condition (eq. A.12), we can consider the left panel of Fig. (3.4). It is possible to notice that there is a prevalent positive difference apart from the region near the free surface. The maximum of $\Delta\tau_{\rho z}$ in this configuration is $3.39 \cdot 10^5$ Pa and is reached in $(\pm 560; 600)$ m; while the minimum is $-9.50 \cdot 10^5$ Pa and it is reached in $(\pm 500; 0)$ m at $x = \pm a$. In general, due to image source method, the relative difference on the free surface is 100%. Those values decrease in modulus moving away from the source. There is also a slight negative difference, invisible in the plot for the choice of the color bar, inside the source, because in the case of the solution in the unbounded space, the value of $\tau_{\rho z}$ inside the TPE inclusion is identically null.
Fig. (3.4) shows the same difference when the center of the sphere is located in $z_0 = 5000$ m. As for τ_{zz} (Fig. 3.3d), being the source farther from the free surface, the difference between the two solutions decreased. By using the same color bar, it is impossible to appreciate the non-null values. In this case, the minimum is also reached on the free surface, at the point $(-2500; 0)$ m; while the maximum is reached at $(-2705; 2800)$ m. Both minimum and maximum are two orders of magnitude lower than the corresponding values when $z_0 = 1000$ m.

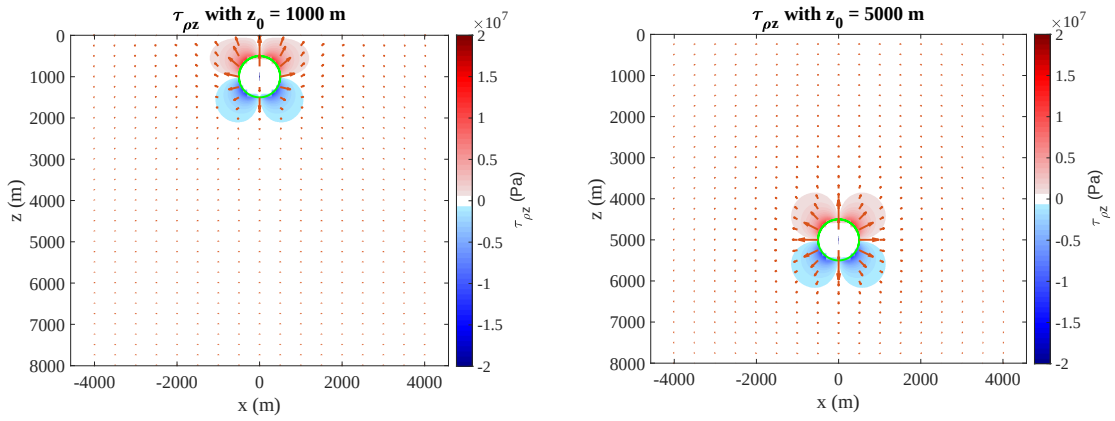

(a) **(b)**

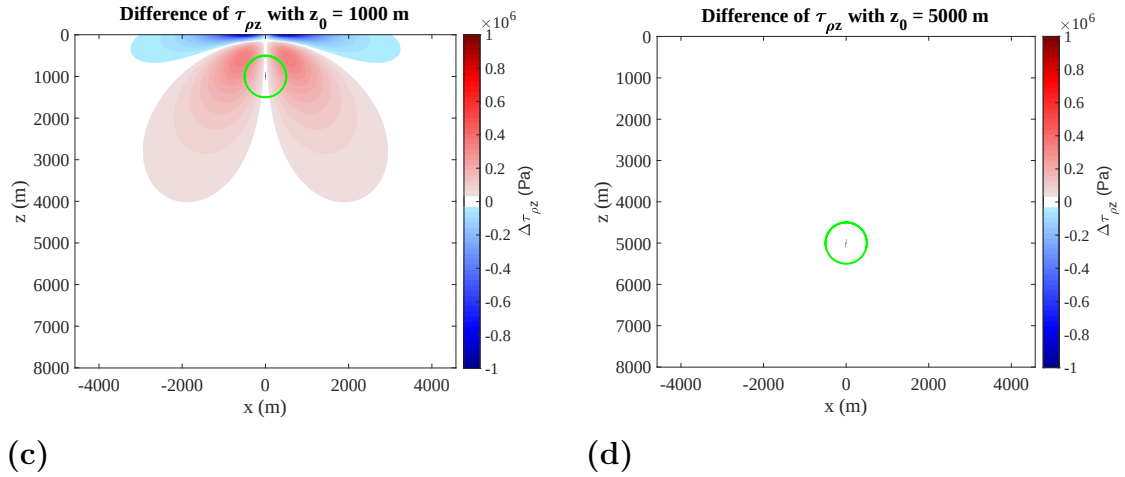

Figure 3.4: *Distribution of the stress component $\tau_{\rho z}$ generated by a spherical TPE inclusion with a radius of 500 m, which center is located at $z = z_0 = 1000$ m in panel (a) and at $z = z_0 = 5000$ m in panel (b), in the plane $y = 0$. Panels (c) and (d) display the difference $\Delta\tau_{\rho z}$ between the stress field computed in a bounded domain (i.e., with the free surface condition) and the same component computed in an unbounded domain (i.e., without the free surface). The surface of the spherical inclusion is highlighted by a green line. The color bar to the right indicates the magnitude of the physical quantity shown. The arrows represent the displacement field produced from the TPE inclusion. Note the different color scale in panels (a)-(b) and (c)-(d).*

Fig. (3.5a) represents the distribution of $\tau_{\rho\rho}$ generated by a spherical TPE inclusion located in $z = z_0 = 1000$ m, the expression of which is reported in eqq. (2.40); (2.41). $\tau_{\rho\rho}$, in contrast to τ_{zz}, satisfies the continuity condition on the TPE surface along the x direction; while it manifests a discontinuity of the first kind along the z axis, moving from a strongly negative value inside the sphere to a positive value in the embedding matrix.
In $z = 0$ this component is different from zero; indeed, we can observe positive values in the projection of the TPE. Fig. (3.5b) shows that, for a spherical TPE inclusion located in $z = 5000$ m, analogously to τ_{zz}, the effect of the free surface is greatly mitigated, and the symmetry is much more present.
In order to show the difference between the value of $\tau_{\rho\rho}$ with and without the free surface condition, we can consider Fig. (3.5c). This plot shows the difference, $\Delta\tau_{\rho\rho}$, between $\tau_{\rho\rho}$ in the case of a sphere placed in a half-space and the same component in an unbounded space (eq. A.9). It is possible to notice that there is a prevalent positive difference inside and outside the source, larger in modulus in the part of the half-space closer to the free surface. In particular, on the free surface there is a very low negative difference. The maximum of $\Delta\tau_{\rho\rho}$ in this configuration is $4.44 \cdot 10^6$ Pa and is reached in the origin of the reference system. The value of the relative difference $\Delta\tau_{\rho\rho}/\tau^u_{\rho\rho}$ is 80% ($\tau^b_{\rho\rho}$ is the stress component in a bounded medium). The minimum of $\Delta\tau_{\rho\rho}$ is $-4.28 \cdot 10^5$ Pa and is reached in $(-1415; 0)$ m; the relative difference in this point is 67%.
Fig. (3.5d) shows the same difference when the center of the sphere is located in $z_0 = 5000$ m. Here, being far from the free surface, the maximum absolute value of the difference is more than two orders of magnitude lower than the result with the free surface condition. In fact, from this figure it is impossible to appreciate the small values of difference, except for a small region very close to the projection of the source in the free surface. As in the previous case, the maximum of $\Delta\tau_{\rho\rho}$ in this configuration is $3.55 \cdot 10^4$ Pa and is reached

in the origin of the reference system. In this point, the relative difference is also the same as what we have if $z_0 = 1000$ m. The minimum of this quantity is two orders of magnitude lower than the maximum, and is reached in $(0; 8000)$ m.

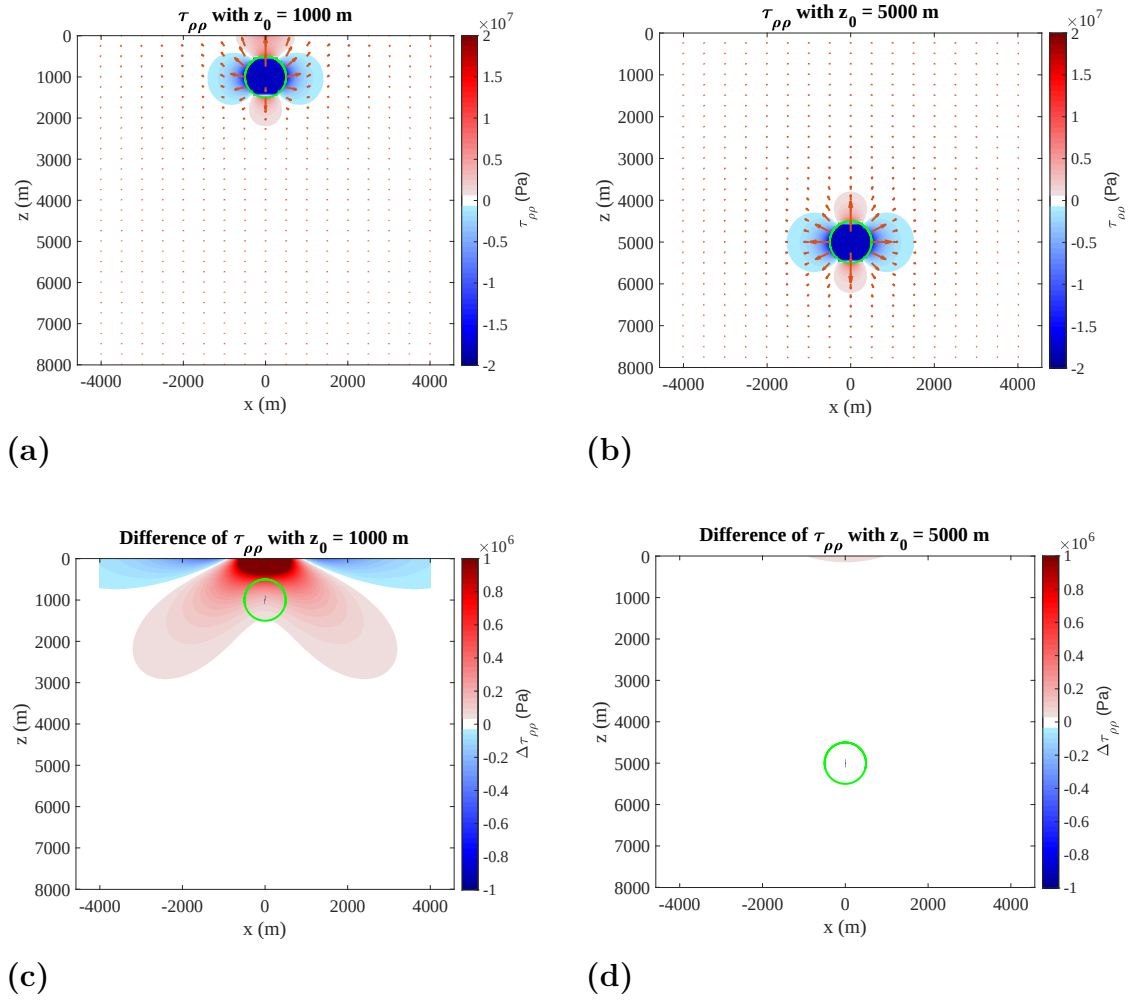

Figure 3.5: *Distribution of the stress component $\tau_{\rho\rho}$ generated by a spherical TPE inclusion with a radius of 500 m, which center is located at $z = z_0 = 1000$ m in panel (a) and at $z = z_0 = 5000$ m in panel (b), in the plane $y = 0$. Panels (c) and (d) display the difference $\Delta\tau_{\rho\rho}$ between the stress field computed in a bounded domain (i.e., with the free surface condition) and the same component computed in an unbounded domain (i.e., without the free surface). The surface of the spherical inclusion is highlighted by a green line. The color bar to the right indicates the magnitude of the physical quantity shown. The arrows represent the displacement field produced from the TPE inclusion. Note the different color scale in panels (a)-(b) and (c)-(d).*

Fig. (3.6a) represents the distribution of $\tau_{\varphi\varphi}$ generated by a spherical TPE inclusion located in $z = z_0 = 1000$ m, the expression of which is reported in eqq. (2.43); (2.44). $\tau_{\varphi\varphi}$ manifests a discontinuity moving from a strongly negative value within the sphere to a positive value in the embedding matrix.
In $z = 0$ this component is different from zero; in fact, we can observe positive values, tending toward zero, further away from the projection of the source. However, $\tau_{\varphi\varphi}$ is not a component of the traction on the plane $z = 0$, so it is not necessary that it vanishes in the half-space solution. It is possible to notice the effect of the free surface, as the symmetry of the intensity is broken. Fig. (3.6b) shows that for a spherical TPE inclusion

located in $z = 5000$ m, analogously to τ_{zz} and $\tau_{\rho\rho}$, the effect of the free surface is greatly mitigated, and the symmetry is much more present.
In order to show the difference, $\Delta\tau_{\varphi\varphi}$, between the value of $\tau_{\varphi\varphi}$ with and without the free surface condition (eq. A.10), we can consider Fig. (3.6c). It is possible to notice that there is a prevalent positive difference outside the source, larger in modulus in the part of the half-space closer to the free surface. In particular, on the free surface there is a higher positive difference. This distribution is similar to that of $\tau_{\rho\rho}$, indeed, the maximum value of $\Delta\tau_{\varphi\varphi}$ is reached at the same point and has the same value of the one computed for $\Delta\tau_{\rho\rho}$. Differently, the minimum is $-8.68 \cdot 10^3$ Pa, and is reached at the point $(0; 3000)$ m. However, the absolute value of the relative difference between the two cases is 6.7%. This confirms that the presence of the free surface causes an increase in $\tau_{\varphi\varphi}$ in most of the domain, and a decrease, much smaller in magnitude, further away from the source, with its maximum located at the surface.
Fig. (3.6d) represents the same difference when the center of the sphere is located in $z_0 = 5000$ m. Here, being far from the free surface, the maximum absolute value of $\Delta\tau_{\varphi\varphi}$ is more than two orders of magnitude lower than the result with the free surface condition. We can notice a positive difference outside the sphere, with maximum in a region closer to the projection of the sphere on the free surface. In this case, this value, as well as the minimum, coincides with the one we found for $\Delta\tau_{\rho\rho}$.

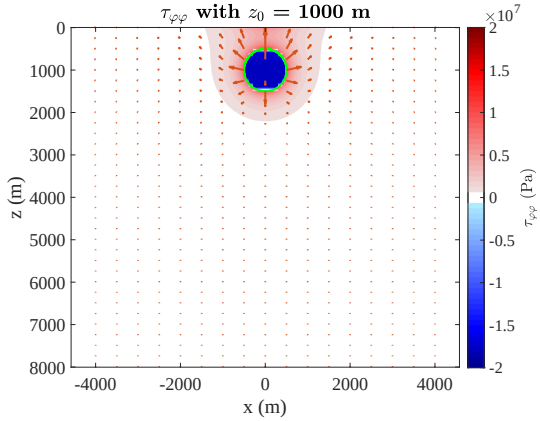

(a)

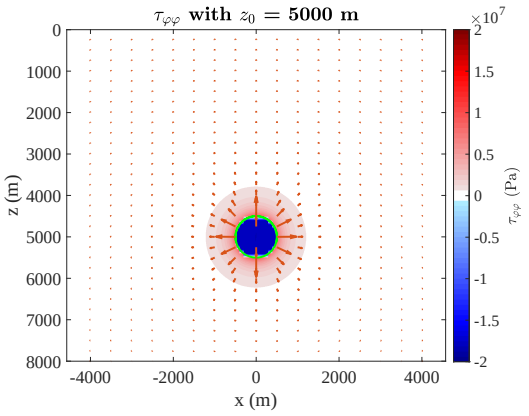

(b)

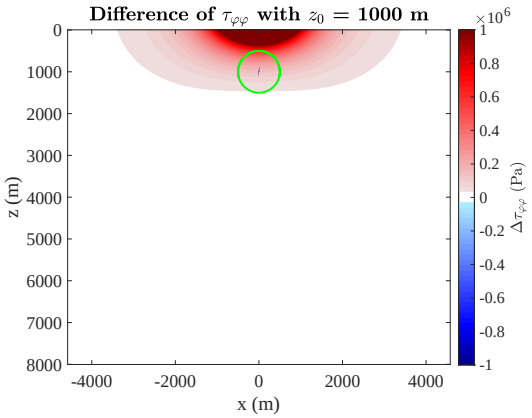

(c)

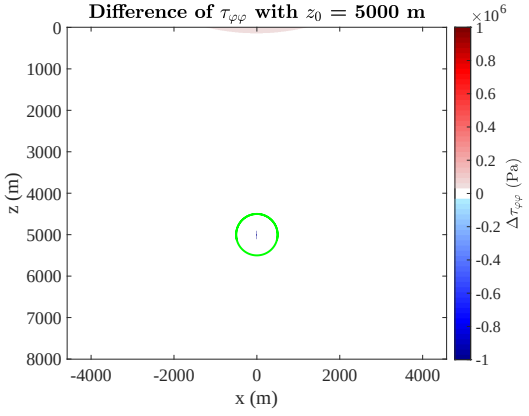

(d)

Figure 3.6: *Distribution of the stress component $\tau_{\varphi\varphi}$ generated by a spherical TPE inclusion with a radius of 500 m, which center is located at $z = z_0 = 1000$ m in panel (a) and at $z = z_0 = 5000$ m in panel (b), in the plane $y = 0$. Panels (c) and (d) display the difference $\Delta\tau_{\varphi\varphi}$ between the stress field computed in a bounded domain (i.e., with the free surface condition) and the same component computed in an unbounded domain (i.e., without the free surface). The surface of the spherical inclusion is highlighted by a green line. The color bar to the right indicates the magnitude of the physical quantity shown. The arrows represent the displacement field produced from the TPE inclusion. Note the different color scale in panels (a)-(b) and (c)-(d).*

3.1.3 Maximum shear stress

Fig. (3.7a) shows the maximum shear stress $S_{\max}$ generated by a spherical TPE inclusion located in $z = z_0 = 1000$ m, the definition of which is reported in eq. (1.18). We can observe that on the free surface $S_{\max}$ does not vanish. Fig. (3.7b) shows the same quantity generated by the same source centered in $z = 5000$ m. In the same way as for the stress components, there is a greater symmetry compared to the previous case, since the effects of the free surface are smaller. Inside the sphere the magnitude of $S_{\max}$ is few orders of magnitude lower than outside, and with this choice of the color bar those values are inappreciable. In order to demonstrate this fact, Fig. (3.8) shows the same plot as Fig. (3.7a) with a narrower range in the color bar. Unlike the full-space scenario (where inside the sphere the stress state is isotropic and outside it is deviatoric), in this case the stress field inside the sphere is not isotropic, although the deviatoric component is less significant. Similarly, outside the sphere the stress field is not completely deviatoric, unlike the full-space case, even though is dominant. Indeed, the maximum shear stress inside the sphere is non-zero, which can explain the presence of seismicity within the TPE inclusion. This is important because it represents a significant difference from the pressurized magmatic cavities (e.g., Mogi source), which exhibit an isotropic stress state inside itself.

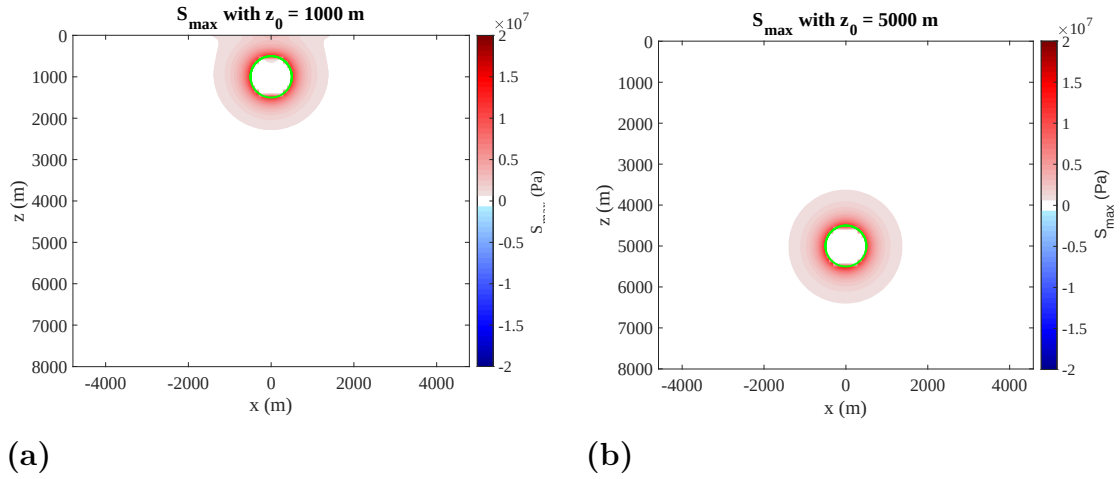

Figure 3.7: *Distribution of the maximum shear stress S_{max} generated by a spherical TPE inclusion with a radius of 500 m, which center is located at $z = z_0 = 1000$ m in panel (a) and at $z = z_0 = 5000$ m in panel (b), in the plane $y = 0$. The surface of the spherical inclusion is highlighted by a green line. The color bar to the right indicates the magnitude of S_{max}.*

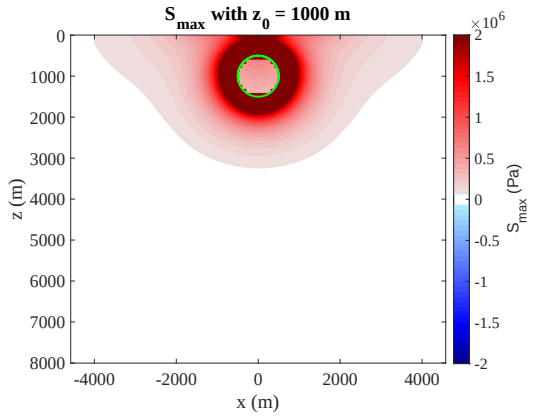

Figure 3.8: *Distribution of the maximum shear stress S_{max} generated by a spherical TPE inclusion with a radius of 500 m, which center is located at $z = z_0 = 1000$ m, in the plane $y = 0$. With respect to Fig. (3.7a), the color bar is narrowed. The surface of the spherical inclusion is highlighted by a green line. The color bar to the right indicates the magnitude of S_{max}.*

In order to understand when solutions given in this work are needed (at least for $S_{\max}$), it is possible to plot the relative difference between the absolute value of the maximum shear stress in the case where the source is in a half-space and in the case where it is in a full space, as functions of depth z. The maximum shear stress is evaluated as a function of z in $x = 0$. In Fig. (3.9) there are four cases as the ratio z_0/a changes, and we chose to plot the graphs for $0 \leq z \leq z_0 - a$. In this case $a = 500$ m is fixed and z_0 changes. At a depth such that the relative difference becomes sufficiently low, in this case 15% was considered, the solution for a full-space is also sufficiently accurate. It can be seen that the distribution of the relative difference is qualitatively the same for different z_0/a: it decreases until its value is null, then it reaches a local minimum, and then it tends to zero as z increases. For $z = 0$ we have that the relative difference is always equal to 0.4. The null value is reached in $z^* \simeq 125$ m when $z_0/a = 2$, when $z_0/a = 4$ we have $z^* \simeq 255$ m, when $z_0/a = 6$ we have $z^* \simeq 375$ m and when $z_0/a = 8$ we have $z^* \simeq 490$ m. We can observe that the decrease is rapid for $0 \leq z \leq z_*$; therefore, the solution for a full-space is sufficiently precise for depth larger than about $z^*/2$, where z^* scales with z_0/a. Below $z = z^*$, the maximum shear stress obtained in the full-space configuration is, in absolute value, greater than that obtained in the half-space configuration. As expected, although not shown in the graph, the variation between the maximum shear stress in the two cases tends to zero for $z \to +\infty$. Nevertheless, for $z > z^*$, this difference remains below 15% in absolute terms (see dashed blue lines in Fig. 3.9).

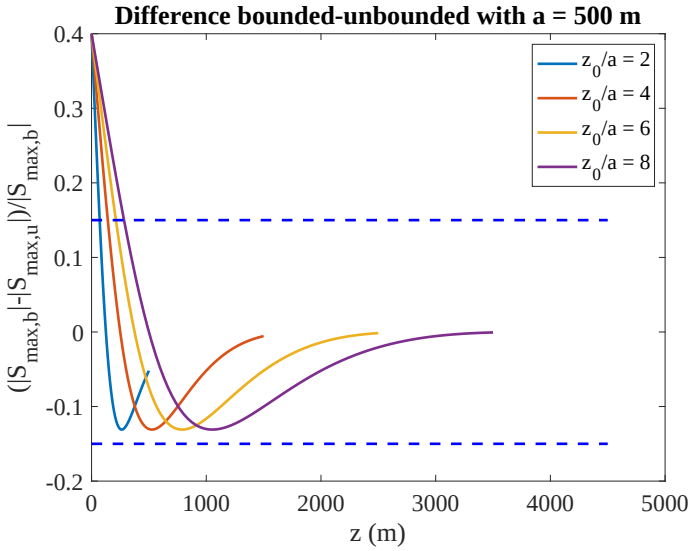

Figure 3.9: *Absolute value of the relative difference between the maximum shear stress in the case where the source is in a half-space and in the case where it is in a full space, as functions of depth z. There are four cases, shown in the legend, as the ratio z_0/a changes. In this graph we kept $a = 500$ m constant. The dashed blue lines indicate a relative difference of $\pm 15\%$.*

3.1.4 Results in the median plane and on the free surface

In this subsection I evaluate with more detail, on the median plane of the TPE sphere ($z = z_0$), displacement and stress components as functions of the x/a ratio. For these plots, the center of the spherical source was placed at $z_0 = 1000$ m.
The distribution of the displacement components can be seen in Fig. (3.10). We note that both components are continuous across the surface of the sphere and that u_ρ is always positive, while u_z is always negative, as an uplift occurs. Moving away from the source, both tend to zero.

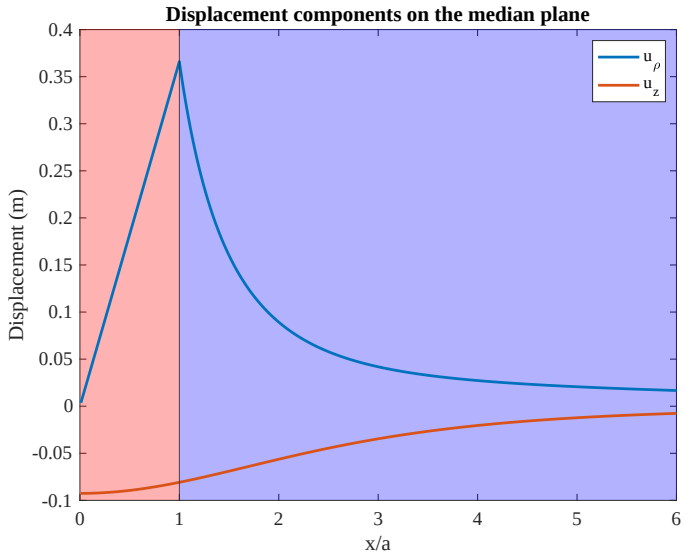

Figure 3.10: *Distribution of displacement components in the median plane ($z = z_0$) as functions of the ratio x/a. The interior of the TPE, i.e., the $x/a < 1$ half-plane, is shown in pink, while the embedding matrix, i.e., the $x/a > 1$ half-plane, is colored purple.*

The distribution of the stress components is shown in Fig. (3.11). It can be seen that the only continuous component across the surface of the sphere is $\tau_{\rho\rho}$, while $\tau_{\varphi\varphi}$ and τ_{zz} show a discontinuity of the first kind from the TPE domain to the matrix domain. The component $\tau_{\rho z}$ is identically zero. The maximum shear stress $S_{\max}$ is two orders of magnitude higher in the embedding matrix than within the TPE source; whereas, in the full-space case (Belardinelli et al., 2019), it was identically zero within the TPE inclusion.

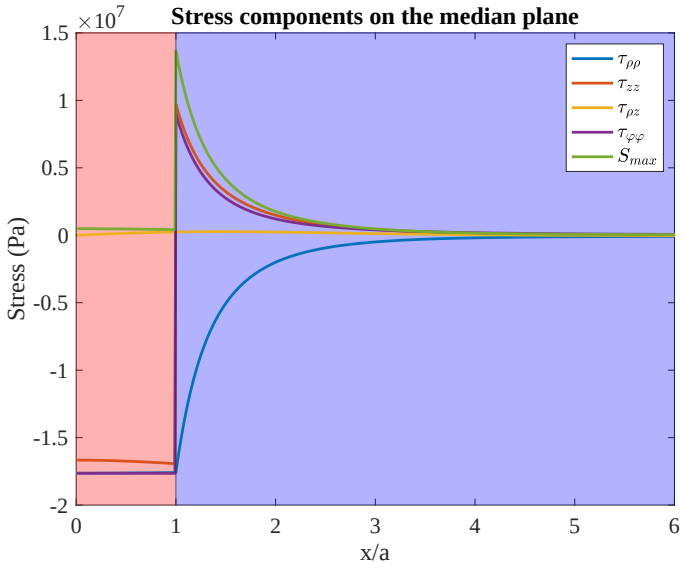

Figure 3.11: *Distribution of stress components and maximum shear stress in the median plane ($z = z_0$) as functions of the ratio x/a. The interior of the TPE, i.e., the $x/a < 1$ half-plane, is shown in pink, while the embedding matrix, i.e., the $x/a > 1$ half-plane, is colored purple.*

As stated in section (1.2.2), it is important to analyze the diagonal deviatoric stress field to determine the stress regime. We can compute these components on the median plane as shown in Fig. (3.12). It is possible to observe that we have a tensile deviatoric stress $\tau'_{zz} = \sigma'_3 > 0$ along the vertical axis for $x/a < 3$, suggesting the presence of a compressive environment within the source and in the first km outside the source. For $x > 3a$ the order of magnitude of each component is more than one lower than the corresponding value in the other half plane; hence, the seismicity they could account for would be negligible.

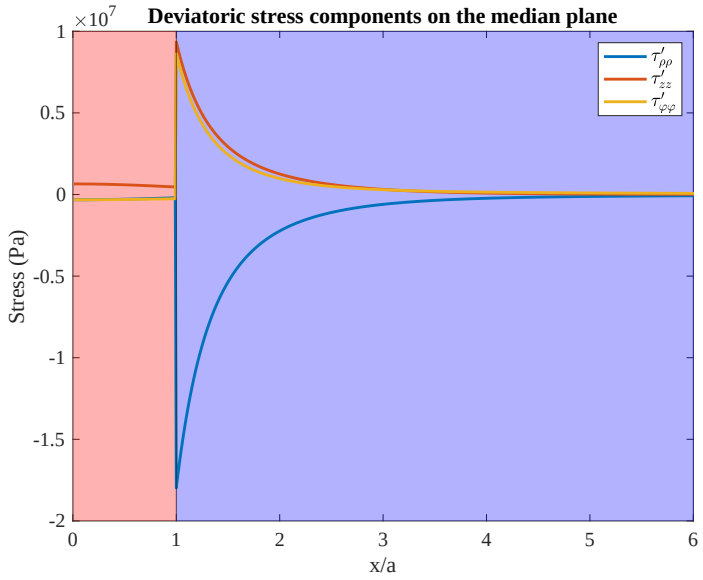

Figure 3.12: *Distribution of the diagonal deviatoric stress components in the median plane ($z = z_0$) as functions of the ratio x/a. The interior of the TPE, i.e., the $x/a < 1$ half-plane, is shown in pink, while the embedding matrix, i.e., the $x/a > 1$ half-plane, is colored purple.*

It is possible to obtain the same plots in $z = 0$, hence, at the free surface. Fig. (3.13) shows the distribution of displacement components on the free surface ($z = 0$) as functions of the ratio x/a. Differently from u_ρ, the maximum of the uplift is located in $x = 0$, and moving significantly away from the surface projection of the source, both components tend to zero. The distribution of u_z provides an initial consistency with the expected distribution of a deformation source model describing surface displacement in a hydrothermal area such as Campi Flegrei. A qualitatively similar vertical ground displacement pattern was observed during the 1982–1984 unrest episode (Trasatti et al., 2011) or during the episode of unrest at Vulcano Island summarized in section (1.1.2) and described by (Stissi et al., 2023), since such a pattern is typical of axisymmetric deformation sources.

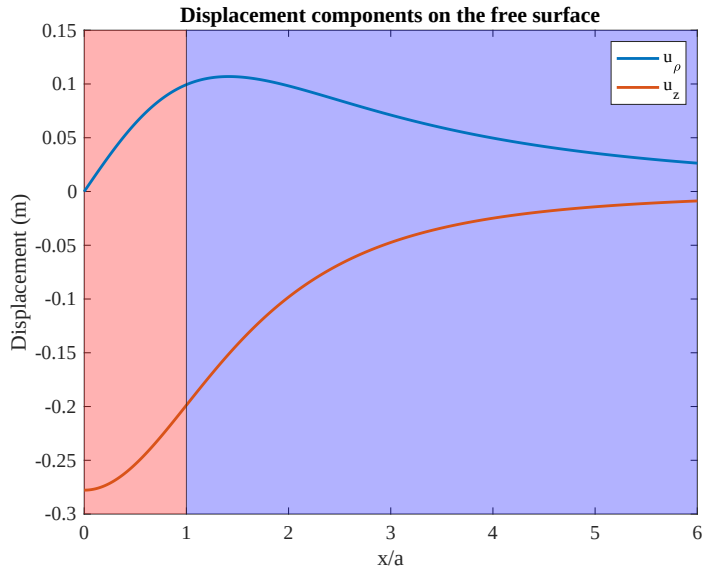

Figure 3.13: *Distribution of displacement components on the free surface ($z = 0$) as functions of the ratio x/a. The part of space corresponding to the projection of the TPE source on the surface, i.e., the $x/a < 1$ half-plane, is shown in pink, while the part corresponding to the embedding matrix, i.e., the $x/a > 1$ half-plane, is colored purple.*

We can also visualize the distribution of the components of the stress field and maximum shear stress, as shown in Fig. (3.14). It is possible to observe that, as expected from the theoretical point of view, τ_{zz} and $\tau_{\rho z}$ are identically zero, while $\tau_{\varphi\varphi}$ is always positive and $\tau_{\rho\rho}$ goes from positive to negative value for $x/a \simeq 1.7$. All stress components tend to zero for $x \to +\infty$ and the maximum order of magnitude is one less than that in the median plane. Unlike what happens on the median plane, where $x/a = 1$ indicates the transition point from the TPE source to the embedding matrix, here each component is continuous in the domain.

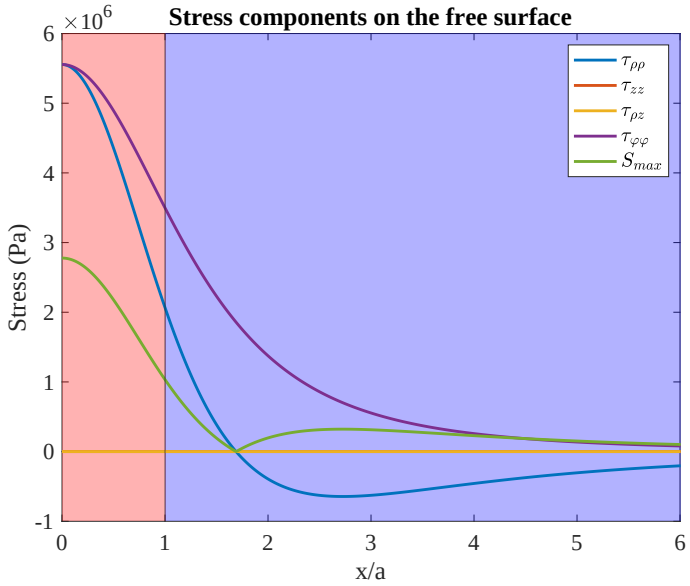

Figure 3.14: *Distribution of stress components on the free surface ($z = 0$) as functions of the ratio x/a. The part of space corresponding to the projection of the TPE source on the surface, i.e., the $x/a < 1$ half-plane, is shown in pink, while the part corresponding to the embedding matrix, i.e., the $x/a > 1$ half-plane, is colored purple.*

We can analyze the diagonal deviatoric stress components on the free surface, shown in Fig. (3.15). Here, it is possible to notice that, for $x/a < 1.7$, $\tau'_{zz} = \sigma'_1 < 0$; while, for $x/a > 1.7$ we have that $\tau'_{zz} = \sigma'_2$. This suggests an extensive tectonic environment within the TPE inclusion and just outside it; while, in the other part of the domain, as τ'_{zz} becomes the intermediate eigenvalue of the deviatoric stress tensor, we should have a strike-slip regime.

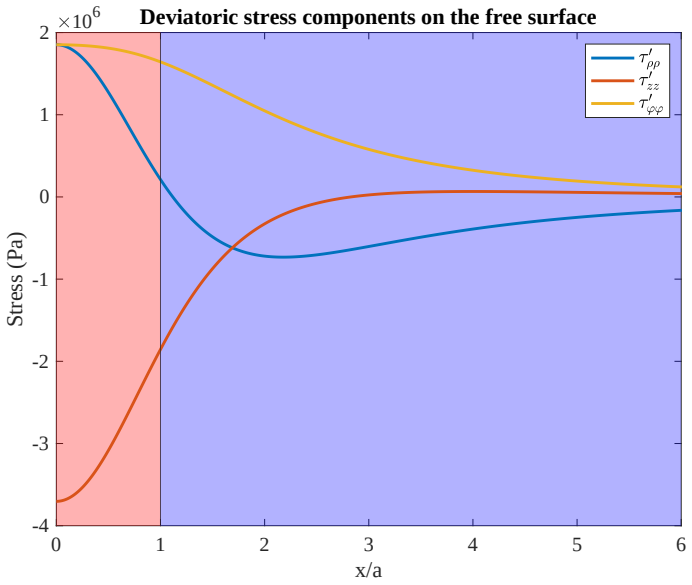

Figure 3.15: *Distribution of the diagonal deviatoric stress components on the free surface ($z = 0$) as functions of the ratio x/a. The interior of the TPE, i.e., the $x/a < 1$ half-plane, is shown in pink, while the embedding matrix, i.e., the $x/a > 1$ half-plane, is colored purple.*

3.1.5 Change of the Coulomb failure function

As shown by Belardinelli et al. (2019), in order to assess the cumulative effect of the stress changes on fault stability, it is possible to compute the change of the Coulomb failure function ΔCFF due to TPE deformation:

$$\Delta CFF = |\Delta\tau| + f\left(\Delta\sigma_n + \Delta p\right), \tag{3.1}$$

where $\Delta\tau$ is the change of the shear traction acting on the fault plane, f is the coefficient of friction, $\Delta\sigma_n$ (negative if compressive) is the change of the normal traction and $\Delta p = p$ for $R < a$ and $\Delta p = 0$ otherwise (undrained condition), is the pore pressure change. $\Delta\tau$ and $\Delta\sigma_n$ depend on the fault dip δ (where $\delta \in [0; \pi/2]$). We calculated for each point in the domain the value of the dip angle that made ΔCFF the maximum, and hence the ΔCFF. The dip angle was varied from 0 to 90°, and, for each of these values, the normal vector $\mathbf{n}$ of the corresponding plane was calculated. From Cauchy's formula in eq. (1.13), it was possible to calculate the traction T_i and, from it, $\Delta\sigma_n = T_i n_i$ and $\Delta\tau = \sqrt{|T_i|^2 - \Delta\sigma_n^2}$.
ΔCFF generated by a spherical TPE inclusion located at $z = z_0 = 1000$ m, is shown in Fig. (3.16a). The distribution of ΔCFF shown in Fig. (3.16b)represents the case where the same sphere is placed in an unlimited medium. For each plot the friction coefficient is $f = 0.6$.

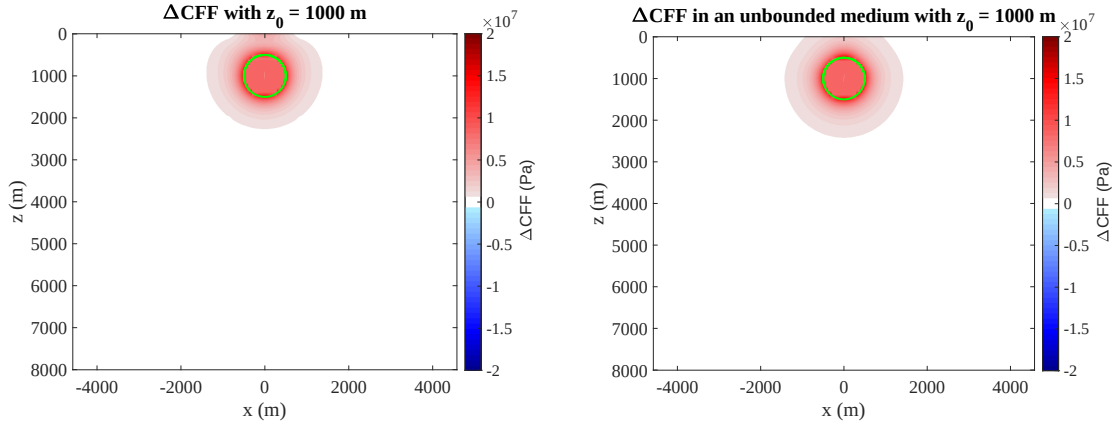

(a) (b)

Figure 3.16: *Panel (a) shows the distribution of the Coulomb failure fracture ΔCFF generated by a spherical TPE inclusion of radius 500 m, located in $z = z_0 = 1000$ m in the plane $y = 0$. The surface of the sphere is highlighted with a green line. The color bar on the right of the picture represents the magnitude of ΔCFF. The same plot for a sphere placed in an unbounded medium is in panel (b).*

3.1.6 Strain Field

From the following figures, representing the non-vanishing strain components, it will be possible to notice that their distribution is similar to that of the corresponding stress component. Fig. (3.17a) represents the distribution of the strain component ϵ_{zz} generated by a spherical TPE inclusion located in $z = z_0 = 1000$ m, the expression of which is reported in eq. (2.30). Fig. (3.17b) shows the same component of the strain field when $z_0 = 5000$ m. As said before, the similarity to τ_{zz}, shown in Fig. (3.3), is evident. The main difference is the sign of the quantities inside the TPE source, as the strain is positive and the stress is negative. This is due to the fact that the constitutive relation reported in eq. (1.42) includes, within the source region, the term $-(1+\nu)\epsilon_0$ (related to the stress-free strain tensor), which arises from the traction continuity condition across the spherical surface and, consequently, from the scalar displacement potential discontinuity condition in eq. (1.59).

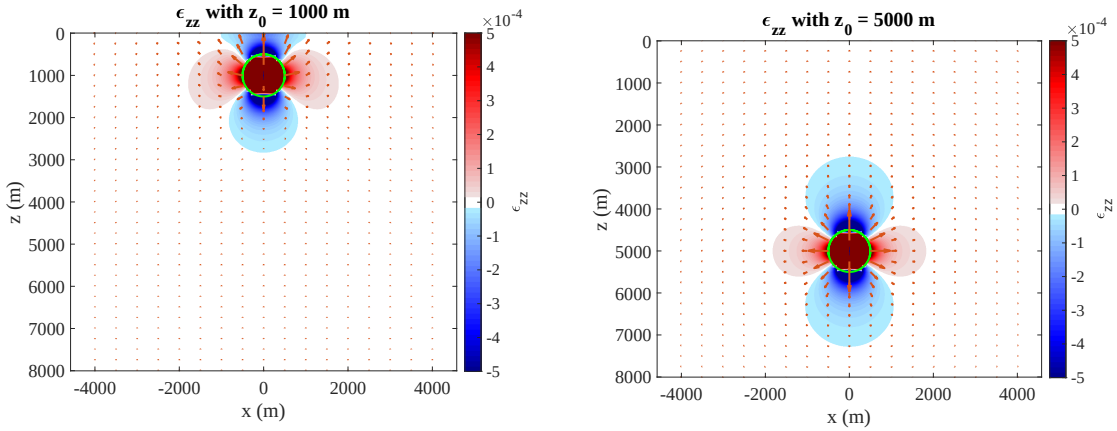

(a) (b)

Figure 3.17: *Distribution of ϵ_{zz} generated by a spherical TPE inclusion of radius 500 m, with the center located in $z = z_0 = 1000$ m in panel (a) and in $z_0 = 5000$ m in panel (b), in the plane $y = 0$. The surface of the sphere is highlighted with a green line. The color bar on the right of the picture represents the magnitude of ϵ_{zz} and the arrows represent the displacement field produced from the TPE inclusion.*

Fig. (3.18a) represents the distribution of the strain component $\epsilon_{\rho z}$ generated by a spherical TPE inclusion located in $z = z_0 = 1000$ m, the expression of which is reported in eq. (2.32). Fig. (3.18b) shows the same component of the strain field when $z_0 = 5000$ m. As said before, the similarity to $\tau_{\rho z}$, shown in Fig. (3.3), is evident. In this case, there is no sign difference with respect to the stress because the relation that links them is given by $\tau_{\rho z} = 2\mu\epsilon_{\rho z}$, and μ is a parameter defined to be positive.

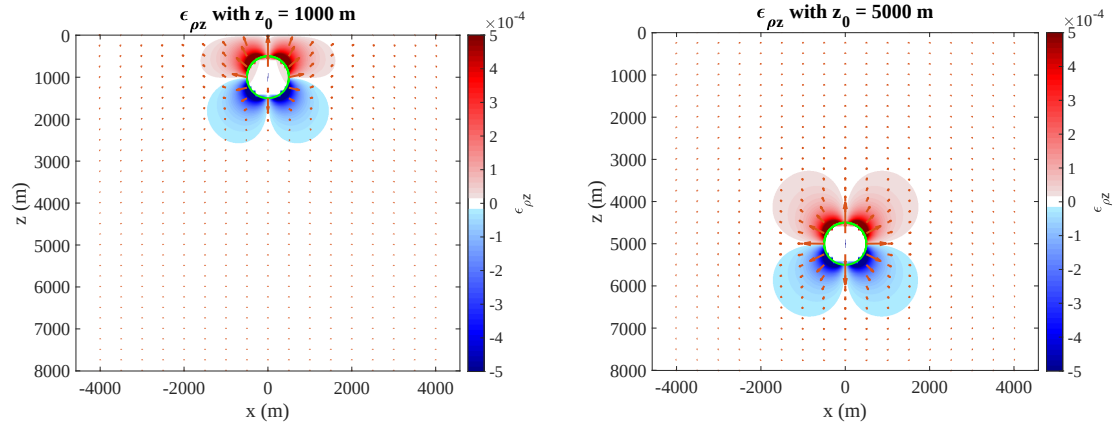

Figure 3.18: *Distribution of $\epsilon_{\rho z}$ generated by a spherical TPE inclusion of radius 500 m, with the center located in $z = z_0 = 1000$ m in panel (a) and in $z_0 = 5000$ m in panel (b), in the plane $y = 0$. The surface of the sphere is highlighted with a green line. The color bar on the right of the picture represents the magnitude of $\epsilon_{\rho z}$ and the arrows represent the displacement field produced from the TPE inclusion.*

Fig. (3.19a) represents the distribution of the strain component $\epsilon_{\rho\rho}$ generated by a spherical TPE inclusion located in $z = z_0 = 1000$ m, the expression of which is reported in eq. (2.26). Fig. (3.19b) shows the same component of the strain field when $z_0 = 5000$ m.
As said before, the similarity to $\tau_{\rho\rho}$, shown in Fig. (3.5), is evident. The main difference is the sign of the quantities inside the TPE source, as the strain is positive and the stress is negative.

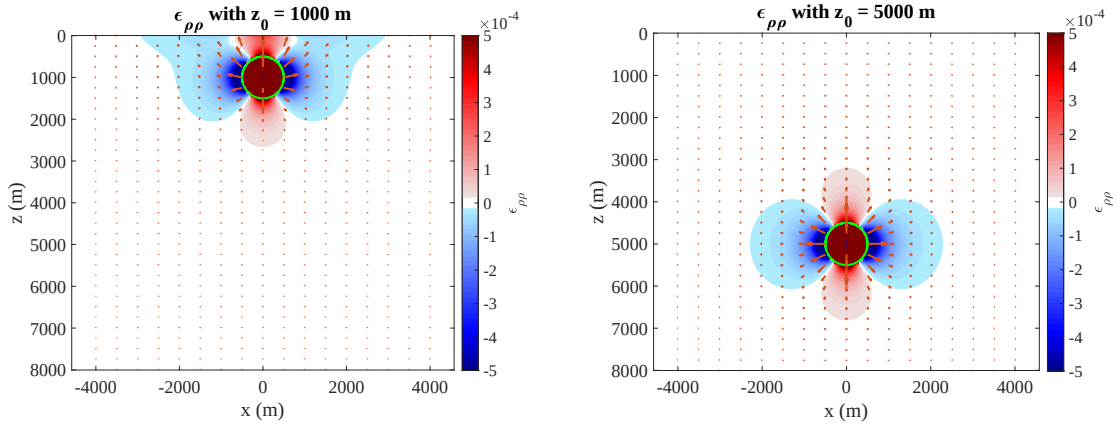

(a) **(b)**

Figure 3.19: *Distribution of $\epsilon_{\rho\rho}$ generated by a spherical TPE inclusion of radius 500 m, with the center located in $z = z_0 = 1000$ m in panel (a) and in $z_0 = 5000$ m in panel (b), in the plane $y = 0$. The surface of the sphere is highlighted with a green line. The color bar on the right of the picture represents the magnitude of $\epsilon_{\rho\rho}$ and the arrows represent the displacement field produced from the TPE inclusion.*

Fig. (3.20a) represents the distribution of the strain component $\epsilon_{\varphi\varphi}$ generated by a spherical TPE inclusion located in $z = z_0 = 1000$ m, the expression of which is reported in eq. (2.28). Fig. (3.20b) shows the same component of the strain field when $z_0 = 5000$ m.
As said before, the similarity to $\tau_{\varphi\varphi}$, shown in Fig. (3.6), is evident. The main difference is the sign of the quantities inside the TPE source, as the strain is positive and the stress is negative.

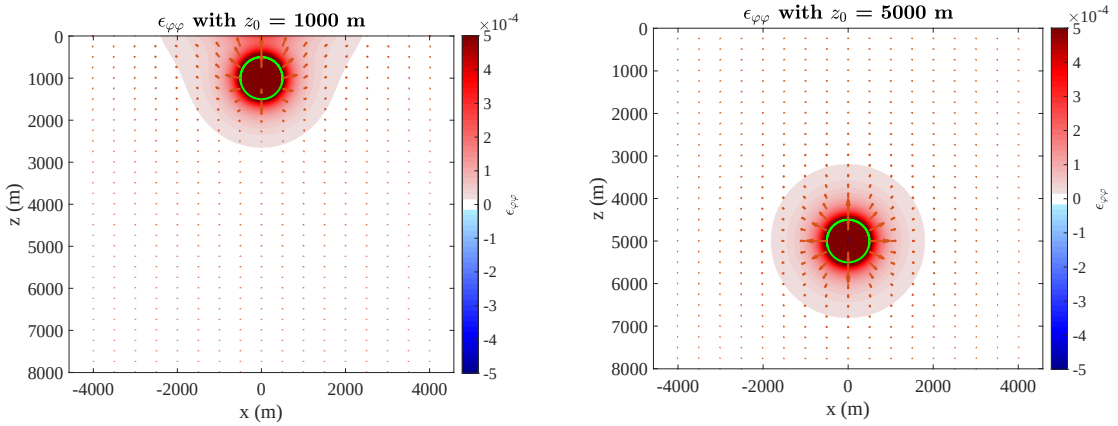

(a) **(b)**

Figure 3.20: *Distribution of $\epsilon_{\varphi\varphi}$ generated by a spherical TPE inclusion of radius 500 m, with the center located in $z = z_0 = 1000$ m in panel (a) and in $z_0 = 5000$ m in panel (b), in the plane $y = 0$. The surface of the sphere is highlighted with a green line. The color bar on the right of the picture represents the magnitude of $\epsilon_{\varphi\varphi}$ and the arrows represent the displacement field produced from the TPE inclusion.*

Fig. (3.21a) represents the distribution of the cubic dilation ϵ_{kk} generated by a spherical TPE inclusion located in $z = z_0 = 1000$ m. Fig. (3.21b) shows the cubic dilation when $z_0 = 5000$ m. It can be observed that the volumetric strain is

predominantly positive both at $z = 0$ and at $z = 5000$ m. Moreover, at greater depths the contribution of the free surface becomes less significant; in fact, the behavior of ϵ_{kk} shows a positive volume change inside the sphere and an almost negligible one outside. This highlights the clear expansion occurring within the source, which does not take place outside. This is consistent with the full-space case, where the stress is completely isotropic inside the inclusion and deviatoric outside. In contrast, the presence of the free surface induces an additional expansion in the region surrounding the source, which gradually decreases with distance from it.

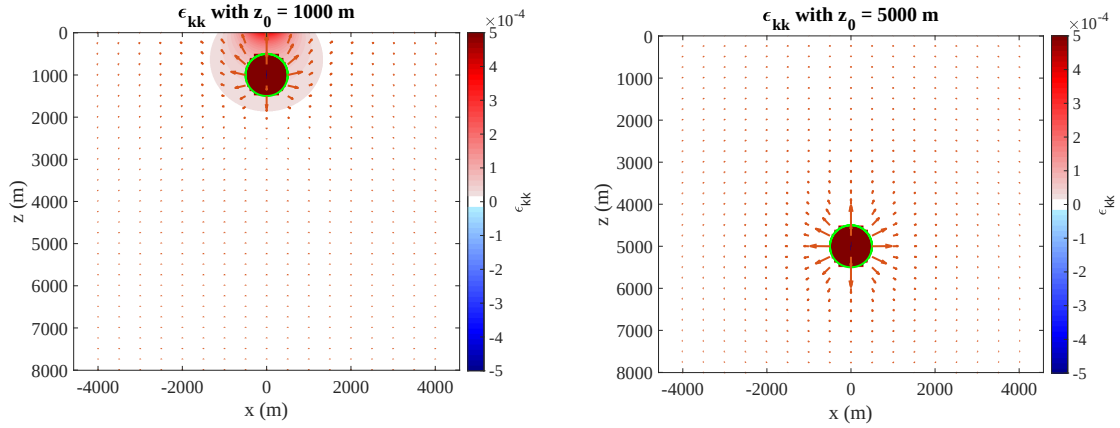

Figure 3.21: *Distribution of the cubic dilation ϵ_{kk} generated by a spherical TPE inclusion of radius 500 m, with the center located in $z = z_0 = 1000$ m in panel (a) and in $z_0 = 5000$ m in panel (b), in the plane $y = 0$. The surface of the sphere is highlighted with a green line. The color bar on the right of the picture represents the magnitude of ϵ_{kk} and the arrows represent the displacement field produced from the TPE inclusion.*

3.2 Results for a spherical TPE shell inclusion

In this section, we analyze the case of a spherical shell TPE inclusion with inner radius $a = 200$ m and outer radius $b = 500$ m. As in the case of the spherical source (discussed in section 3.1), two configurations are considered: in the first, the center of the source is located at $z_0 = 1000$ m; in the second, the source is deeper, with its center at $z_0 = 5000$ m. In the former case, it is observed that, for all components of the analyzed fields, the effect of the free surface is severe, as the symmetry along the $z - z_0$ plane is broken; while in the latter case, the effect of the free surface is greatly mitigated and the symmetry is much more preserved. Moreover, for the non-zero components of the displacement and stress fields, the differences between the solutions for a source embedded in a half-space (computed in sections 2.3.1; 2.3.2; 2.3.3) and the corresponding solutions for a source in an infinite medium (derived in section 2.1 and Appendix A.2) will be shown. These differences are indicated using the symbol of the component preceded by Δ (e.g., for the radial displacement component, such difference is labeled with Δu_ρ).
In addition, since the distribution of ΔCFF does not differ significantly from that obtained for the sphere (Fig. 3.1), the corresponding color map has not been shown in this section.
It is important to state that the figures presented in the following sections do not

show what occurs inside the magma chamber embedded within the TPE source (i.e., for $R < a$), as they only represent the expressions reported in section (2.3).

3.2.1 Displacement field

Fig. (3.22) represents the distribution of u_ρ generated by a spherical shell TPE inclusion, the expression of which is reported in eqq. (2.54); (2.55). Similarly to the sphere, the u_ρ component is everywhere non-negative. We can notice that, in both configurations, the maximum of u_ρ is in the vicinity of $z/z_0 \in [0.5; 1.5]$ and $|x|/b \in [a/b; 1]$.
Fig. (3.22c) shows that the difference Δu_ρ of the radial displacement u_ρ between the configurations with the shell placed in a bounded space and in an unbounded space at $z = z_0 = 1000$ m is qualitatively similar to the one obtained for the spherical source, shown in Fig. (3.1c). However, the maximum value of the difference, although occurring at the same location, is lower, reaching 0.064 m. This indicates that using a thin shell (compared to a full sphere) leads to a smaller incremental displacement. To confirm this, the maximum and minimum values of Δu_ρ were evaluated for different configurations of the shell's inner radius, showing that as the inner radius decreases, the values tend to approach those of the full sphere. The minimum value is also approximately one order of magnitude lower. When $z = z_0 = 5000$ m, the results for the half-space are very similar to the results for an unbounded medium, and the difference between such components is one or two orders of magnitude lower than the case of $z_0 = 1000$ m; therefore, the corresponding plots are not shown.

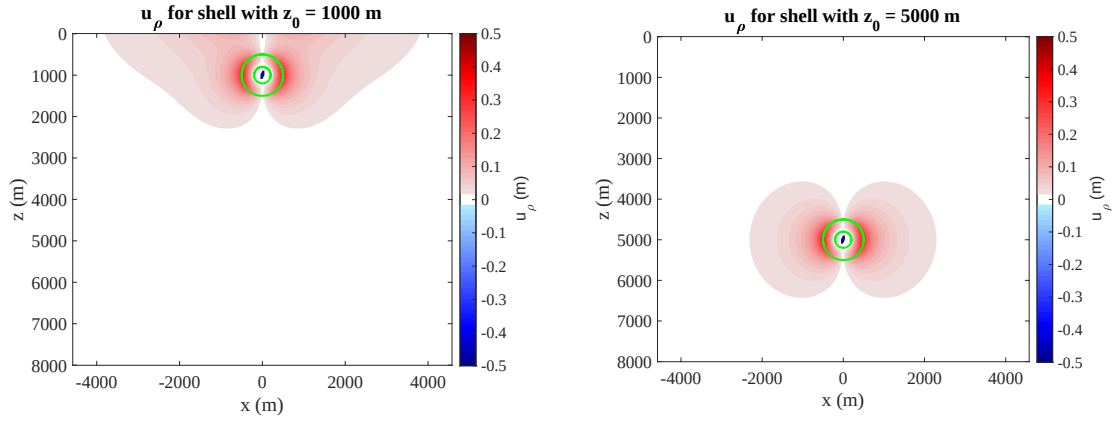

(a) (b)

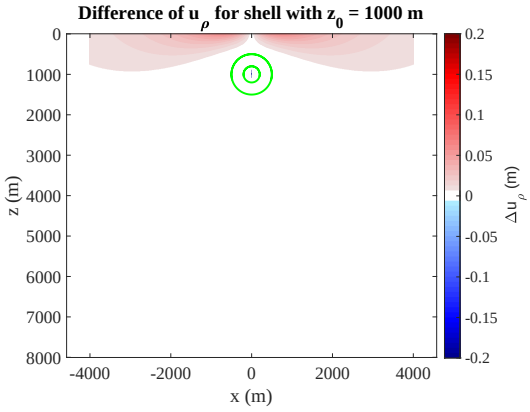

(c)

Figure 3.22: *Distribution of u_ρ generated by a spherical shell TPE inclusion with inner radius $a = 200$ m and outer radius $b = 500$ m, with the center located in $z = z_0 = 1000$ m in panel (a) and in $z_0 = 5000$ m in panel (b), in the plane $y = 0$. Panel (c) shows the difference Δu_ρ between the displacement component, u_ρ generated by the previous considered inclusions, placed in a bounded space (i.e., calculated with the free surface condition) and the same component calculated without that condition. The surface of the sphere is highlighted with a green line. The color bar on the right of the picture represents the magnitude of the physical quantity under consideration.*

Fig. (3.23) represents the distribution of u_z generated by a spherical shell TPE inclusion, the expression of which is reported in eqq. (2.52); (2.53). The u_z component is positive only in the $z > z_0$ half-plane and in the region strictly close to the shell. In the case where the shell is at depth, the sign discontinuity occurs at $z = z_0$, while in the case where the shell is located more at the surface, for $|x|/a \in [2; 6]$ there is a negative value of u_z, corresponding to an uplift.
Fig. (3.23c) shows that the difference Δu_z at $z = z_0 = 1000$ m is qualitatively similar to the one obtained for the spherical source, shown in Fig. (3.2c). Here, the minimum of Δu_z is -0.17 m, slightly lower than the result obtained for the sphere.

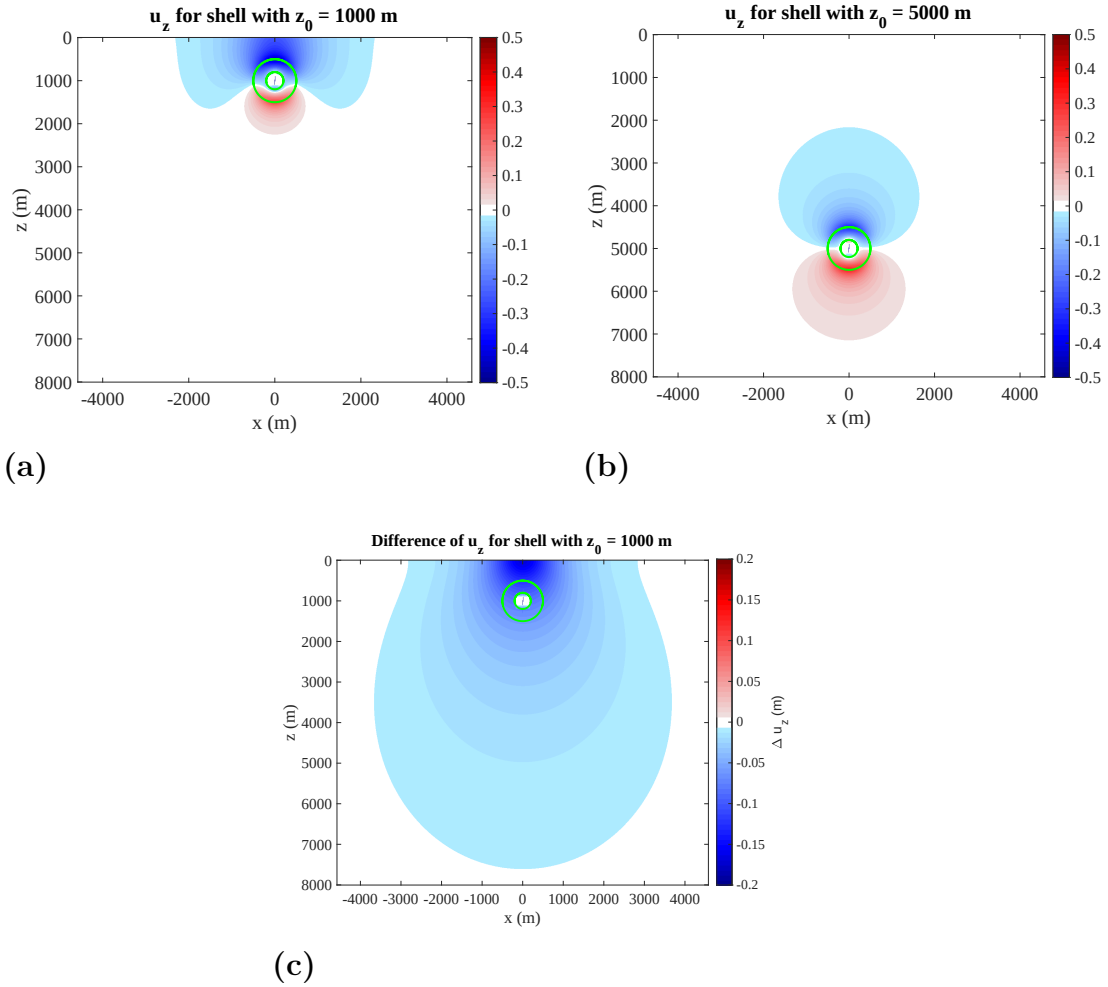

Figure 3.23: *Distribution of u_z generated by a spherical shell TPE inclusion with inner radius $a = 200$ m and outer radius $b = 500$ m, with the center located in $z = z_0 = 1000$ m in panel (a) and in $z_0 = 5000$ m in panel (b), in the plane $y = 0$. Panel (c) shows the difference Δu_z between the displacement component, u_z generated by the previous inclusion, placed in a bounded space (i.e., calculated with the free surface condition) and the same component calculated without that condition. The surface of the sphere is highlighted with a green line. The color bar on the right of the picture represents the magnitude of the physical quantity under consideration.*

3.2.2 Stress Field

Fig. (3.24) represents the distribution of τ_{zz} generated by a spherical shell TPE inclusion, the expression of which is reported in eqq. (2.65); (2.66). Similarly to spherical TPE, τ_{zz} satisfies the continuity condition on the surface of TPE along the z direction; while it manifests a discontinuity of the first kind along the x axis, moving from a strongly negative value inside the TPE to a positive value in the embedding matrix. In $z = 0$, due to the free surface condition, the value of τ_{zz} is identically null.
In order to show the difference $\Delta\tau_{zz}$ between the value of τ_{zz} with and without the free surface condition, we can consider Fig. (3.24c). This picture plots the difference between τ_{zz} in the case of a shell placed in a half-space and the same component, shown in Fig. (3.24a), in an unbounded space (eq. A.15). It is possible to notice that there is a prevalent positive difference inside and outside the source, especially in the part of the half-space closer to the free surface.
Differently from the sphere, the maximum value is $2.32 \cdot 10^6$ Pa and the minimum value is $-5.44 \cdot 10^4$ Pa; both reached at the same point in the case of the sphere.

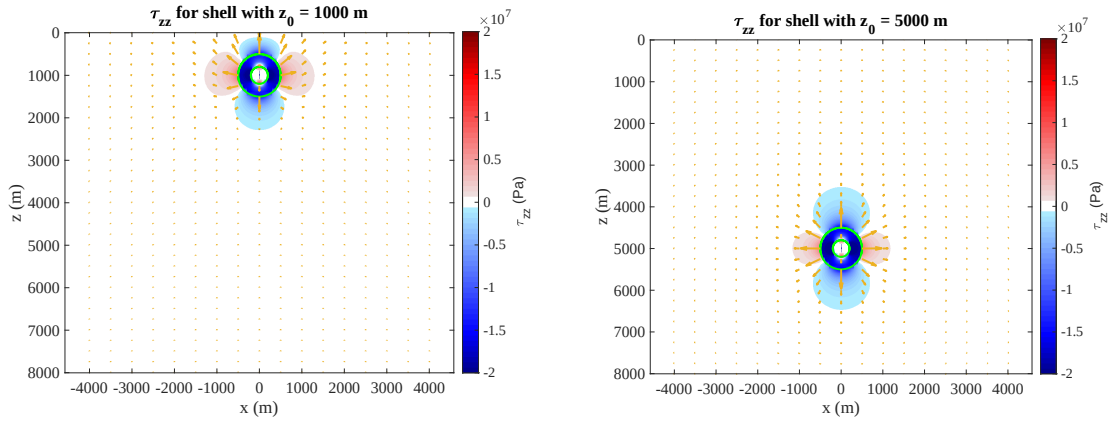

(a) **(b)**

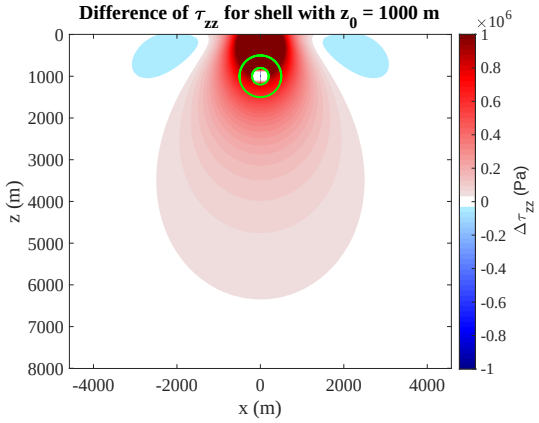

(c)

Figure 3.24: *Distribution of τ_{zz} generated by a spherical shell TPE inclusion with inner radius $a = 200$ m and outer radius $b = 500$ m, with the center located in $z = z_0 = 1000$ m in panel (a) and in $z_0 = 5000$ m in panel (b), in the plane $y = 0$. Panel (c) shows the difference $\Delta\tau_{zz}$ between the stress component, τ_{zz} generated by the previous inclusion, placed in a bounded space (i.e., calculated with the free surface condition) and the same component calculated without that condition. The surface of the sphere is highlighted with a green line. The color bar on the right of the picture represents the magnitude of the physical quantity under consideration and the arrows represent the displacement field produced from the TPE inclusion.*

Fig. (3.25) represents the distribution of $\tau_{\rho z}$ generated by a spherical shell TPE inclusion, the expression of which is reported in eqq. (2.68); (2.69). Unlike the results obtained for the sphere (Fig. 3.4), we observe comparable values of $\tau_{\rho z}$ inside the inclusion than outside it. This is consistent with what we get in the case of the unbounded medium.
In order to show the difference between the value of $\tau_{\rho z}$ with and without the free surface condition, we can consider Fig. (3.25c). This graph plots the difference between $\tau_{\rho z}$ in the case of a shell placed in a half-space and the same component, shown in Fig. (3.25a), in an unbounded space (eq. A.16). It is possible to notice that there is a prevalent positive difference outside the source in the half-space containing the higher hemisphere and a negative difference in proximity of the free surface. In this case the maximum value of $\Delta\tau_{\rho z}$ is $3.05 \cdot 10^5$ Pa and the minimum is $-8.58 \cdot 10^5$ Pa, reached at the same points of the sphere's case.

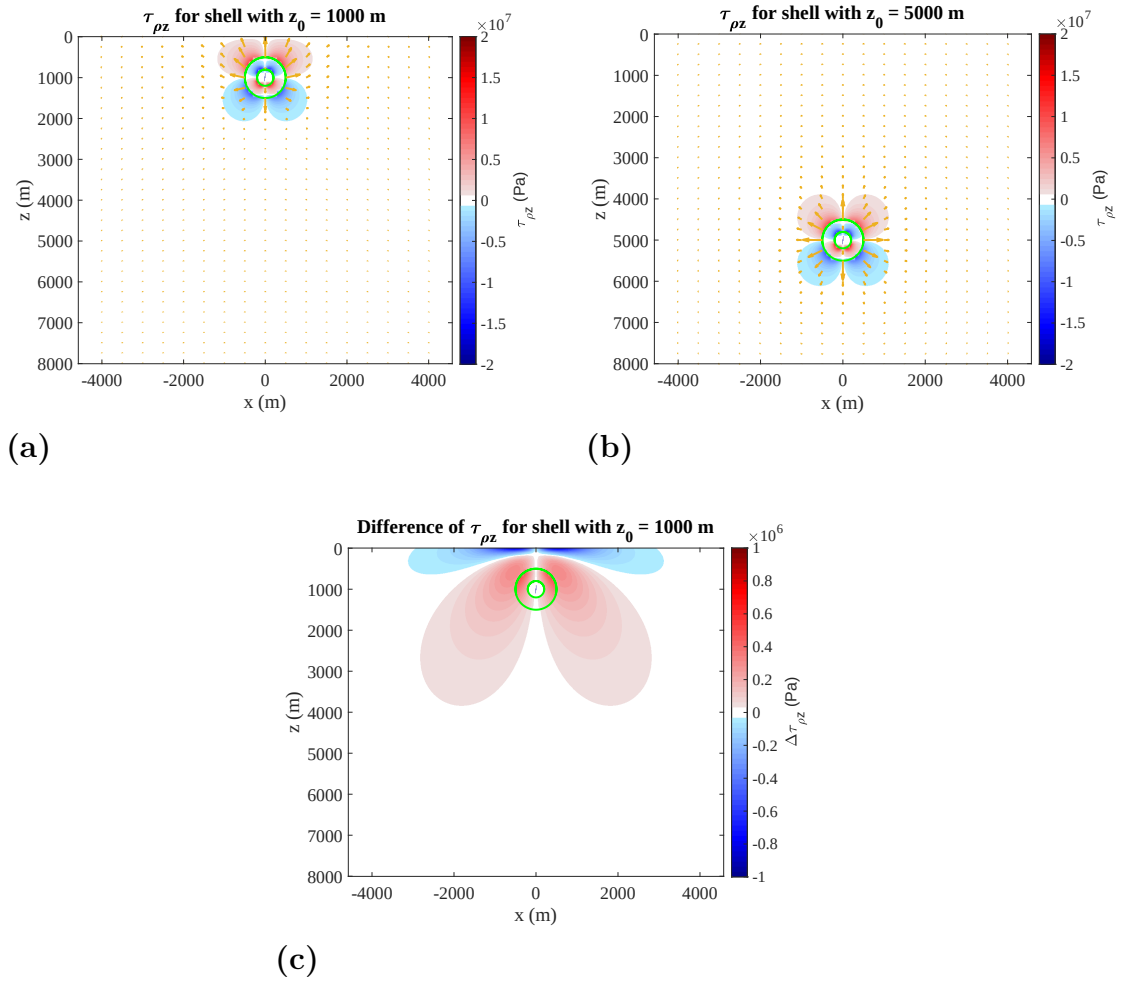

Figure 3.25: *Distribution of $\tau_{\rho z}$ generated by a spherical shell TPE inclusion with inner radius $a = 200$ m and outer radius $b = 500$ m, with the center located in $z = z_0 = 1000$ m in panel (a) and in $z_0 = 5000$ m in panel (b), in the plane $y = 0$. Panel (c) shows the difference $\Delta\tau_{\rho z}$ between the stress component, $\tau_{\rho z}$ generated by the previous inclusion, placed in a bounded space (i.e., calculated with the free surface condition) and the same component calculated without that condition. The surface of the sphere is highlighted with a green line. The color bar on the right of the picture represents the magnitude of the physical quantity under consideration and the arrows represent the displacement field produced from the TPE inclusion.*

Fig. (3.26) represents the distribution of $\tau_{\rho\rho}$ generated by a spherical shell TPE inclusion, the expression of which is reported in eqq. (2.71); (2.72). $\tau_{\rho\rho}$, in contrast to τ_{zz}, satisfies the continuity condition on the TPE surface along the x direction; while it manifests a discontinuity of the first kind along the z axis, moving from a strongly negative value inside the sphere to a positive value in the embedding matrix.
In $z = 0$ we can observe positive values at the projection of the TPE.
Fig. (3.26c) plots the difference $\Delta\tau_{\rho\rho}$ (the full-space solutions are reported in eq. A.13), which maximum and minimum values are respectively $4.00 \cdot 10^6$ Pa and $-3.85 \cdot 10^5$ Pa, reached at the same points of the sphere's case.

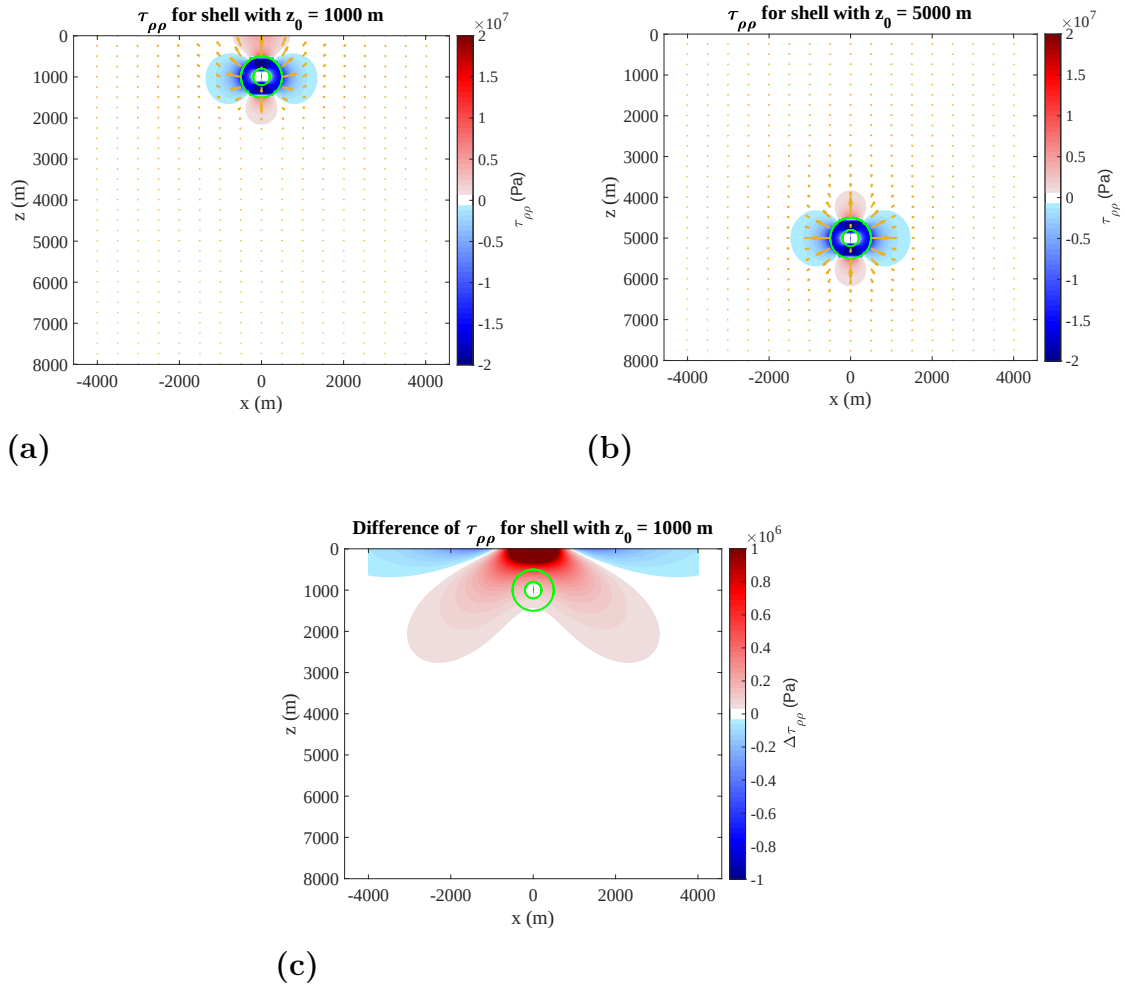

Figure 3.26: *Distribution of $\tau_{\rho\rho}$ generated by a spherical shell TPE inclusion with inner radius $a = 200$ m and outer radius $b = 500$ m, with the center located in $z = z_0 = 1000$ m in panel (a) and in $z_0 = 5000$ m in panel (b), in the plane $y = 0$. Panel (c) shows the difference $\Delta\tau_{\rho\rho}$ between the stress component, $\tau_{\rho\rho}$ generated by the previous inclusion, placed in a bounded space (i.e., calculated with the free surface condition) and the same component calculated without that condition. The surface of the sphere is highlighted with a green line. The color bar on the right of the picture represents the magnitude of the physical quantity under consideration and the arrows represent the displacement field produced from the TPE inclusion.*

Fig. (3.27) represents the distribution of $\tau_{\varphi\varphi}$ generated by a spherical TPE inclusion, the expression of which is reported in eqq. (2.74); (2.75). $\tau_{\varphi\varphi}$, in contrast to τ_{zz}, manifests a discontinuity moving from a strongly negative value within the sphere to a positive value in the embedding matrix.
Similarly to the sphere case, in $z = 0$ this component is different from zero.
In order to observe the difference between the value of $\tau_{\varphi\varphi}$ with and without the free surface condition, we can consider Fig. (3.27c). This graph plots the difference between $\tau_{\varphi\varphi}$ in the case of a shell placed in a half-space and the same component, shown in Fig. (3.27), in an unbounded space (eq. A.14). It is possible to notice that there is a predominant positive difference outside and inside the source. In particular, on the free surface there is a higher positive difference. In this case the maximum value of $\Delta\tau_{\varphi\varphi}$ is $4 \cdot 10^6$ Pa and the minimum is $-7.81 \cdot 10^3$ Pa, reached at the same points of the sphere's case.

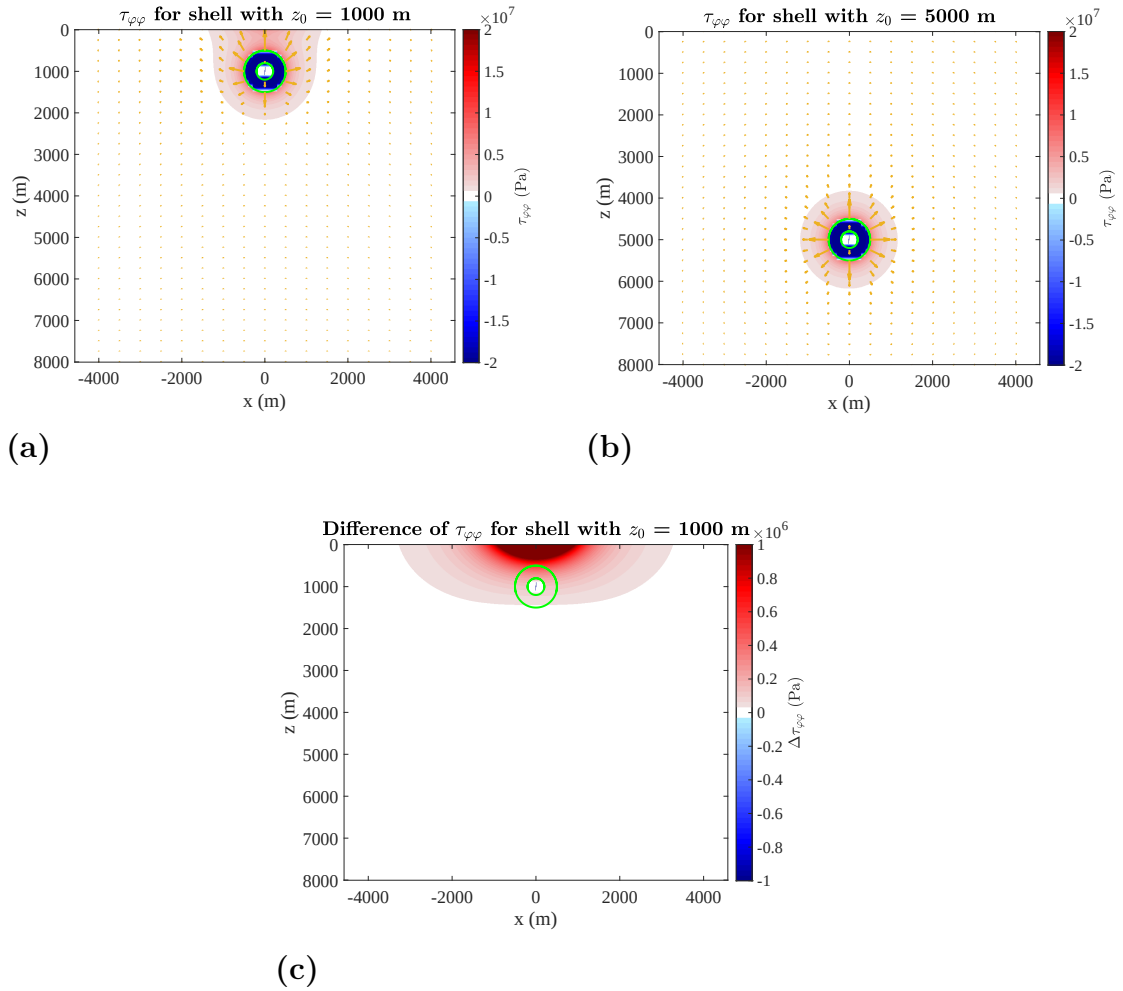

Figure 3.27: *Distribution of $\tau_{\varphi\varphi}$ generated by a spherical shell TPE inclusion with inner radius $a = 200$ m and outer radius $b = 500$ m, with the center located in $z = z_0 = 1000$ m in panel (a) and in $z_0 = 5000$ m in panel (b), in the plane $y = 0$. Panel (c) shows the difference $\Delta\tau_{\varphi\varphi}$ between the stress component, $\tau_{\varphi\varphi}$ generated by the previous inclusion, placed in a bounded space (i.e., calculated with the free surface condition) and the same component calculated without that condition. The surface of the sphere is highlighted with a green line. The color bar on the right of the picture represents the magnitude of the physical quantity under consideration and the arrows represent the displacement field produced from the TPE inclusion.*

3.2.3 Maximum shear stress

Fig. (3.28) shows the maximum shear stress $S_{\max}$ generated by a spherical shell TPE inclusion, the definition of which is reported in eq. (1.18). As observed in the sphere case, the maximum shear stress does not vanish at the free surface. However, unlike the TPE sphere, where $S_{\max}$ remains low within the inclusion, the TPE shell (with the same external radius) exhibits non-vanishing and significantly higher values within its interior (see Fig. 3.28). This feature will be examined in greater detail in chapter 4, and it further confirms the advantage of TPE inclusions in modeling magmatic sources of deformation, particularly in explaining internal seismicity through the presence of significant internal shear stress.

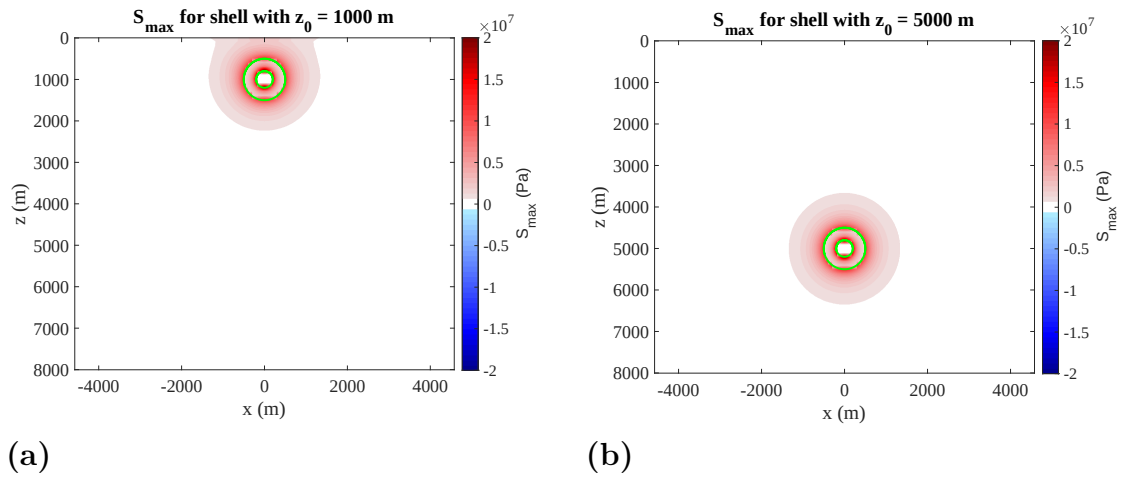

Figure 3.28: *Distribution of maximum shear stress S_{max} generated by a spherical shell TPE inclusion with inner radius $a = 200$ m and outer radius $b = 500$ m, with the center located in $z = z_0 = 1000$ m in panel (a) and in $z_0 = 5000$ m in panel (b), in the plane $y = 0$. The surface of the shell is highlighted with a green line. The color bar on the right of the picture represents the magnitude of S_{max}.*

We can show the same graph of Fig. (3.9) in the case of a shell where the ratio z_0/b varies keeping $b = 500$ m and $a = 200$ m fixed. We can observe that the results are equal to those shown for the sphere.

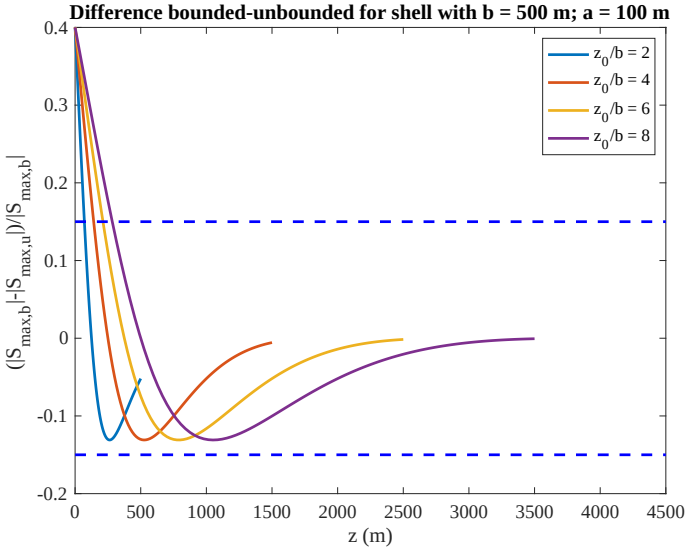

Figure 3.29: *Relative difference of the absolute values of the maximum shear stress in the case where the source is in a half-space and in the case where it is in a full space, as functions of depth z. There are four cases, shown in the legend, as the ratio z_0/b changes. In this graph, we kept $b = 500$ m and $a = 200$ m constants.*

3.2.4 Results in the median plane and on the free surface

In this subsection I evaluate with more detail, on the median plane of the TPE shell ($z = z_0$), displacement and stress components as functions of the x/b ratio. For these graphs, the center of the source was placed at $z_0 = 1000$ m.
The distribution of the displacement components can be seen in Fig. (3.30). We note

that both components are continuous across the outer surface of the shell and u_z is always negative. The radial component u_ρ is positive everywhere in the domain except very close to the inner radius of the shell. Moving away from the source, both tend to zero.
The stress components as functions of x can be observed in Fig. (3.31). The component $\tau_{\rho z}$ is identically zero. The maximum shear stress $S_{\max}$ is one order of magnitude lower in the embedding matrix than within the TPE source. We note that, unlike the sphere (see Fig. 3.11), $S_{\max}$ is higher within TPE domain.

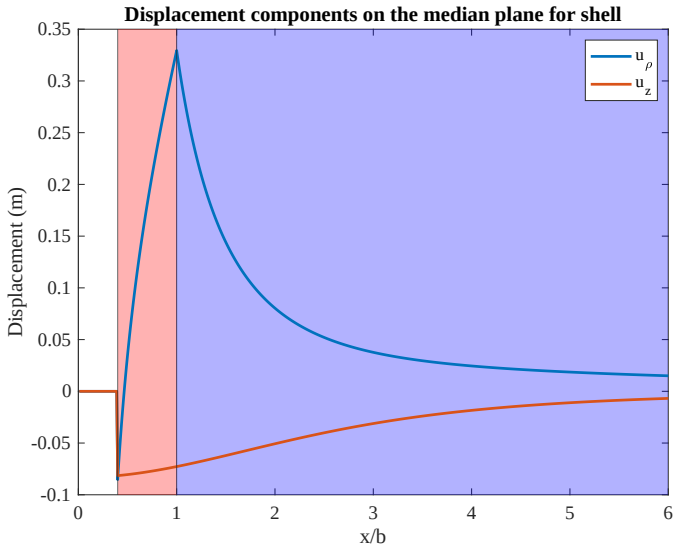

Figure 3.30: *Distribution of displacement components in the median plane ($z = z_0$) as functions of the ratio x/b. The interior of the TPE, i.e., the $a/b < x/b < 1$ half-plane, is shown in pink, while the embedding matrix, i.e., the $x/b > 1$ half-plane, is colored purple.*

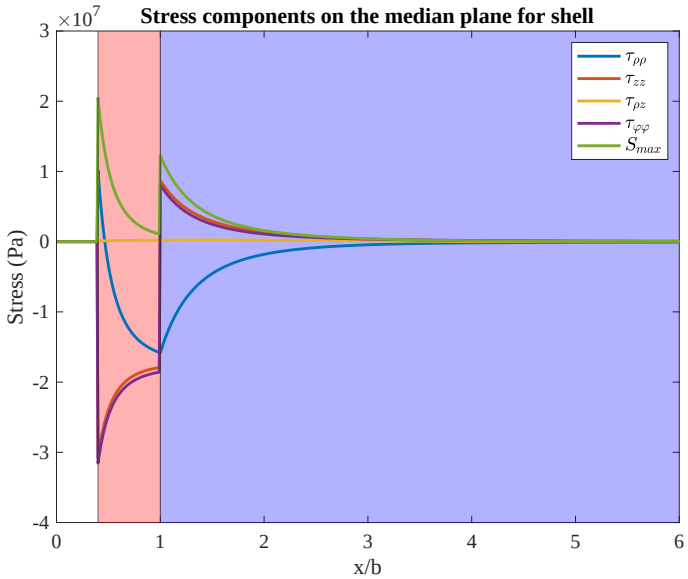

Figure 3.31: *Distribution of stress components and maximum shear stress in the median plane ($z = z_0$) as functions of the ratio x/b. The interior of the TPE, i.e., the $a/b < x/b < 1$ half-plane, is shown in pink, while the embedding matrix, i.e., the $x/b > 1$ half-plane, is colored purple.*

We can compute the diagonal components of the deviatoric stress field on the median plane as shown in Fig. (3.32). It is possible to observe that inside the TPE inclusion the deviatoric stress $\tau'_{zz} = \sigma'_2$ is the intermediate eigenvalue, suggesting the presence of a strike-slip environment. Differently, $\tau'_{zz} = \sigma'_3$ is the most tensile eigenvalue in the embedding matrix, suggesting a compressive stress regime outside the source.

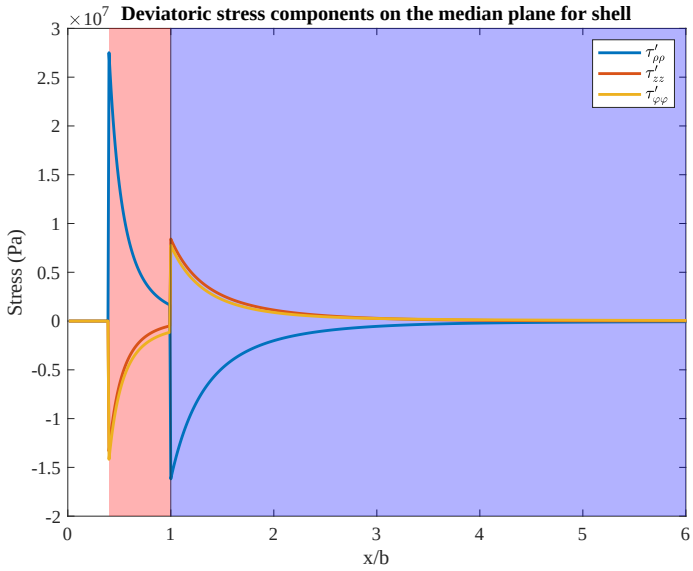

Figure 3.32: *Distribution of the diagonal deviatoric stress components in the median plane ($z = z_0$) as functions of the ratio x/a. The interior of the TPE, i.e., the $a/b < x/b < 1$ half-plane, is shown in pink, while the embedding matrix, i.e., the $x/b > 1$ half-plane, is colored purple.*

The results at the surface, thus at a greater distance from the center of the source, are similar to those obtained for the sphere, since, for a suitable choice of parameters, the solutions for the shell or the sphere match those of the Mogi source at the surface (section 2.3.4). This is shown, respectively, in Fig. (3.33) and (3.34). The results for the spherical source were shown in Fig. (3.13) and (3.14).

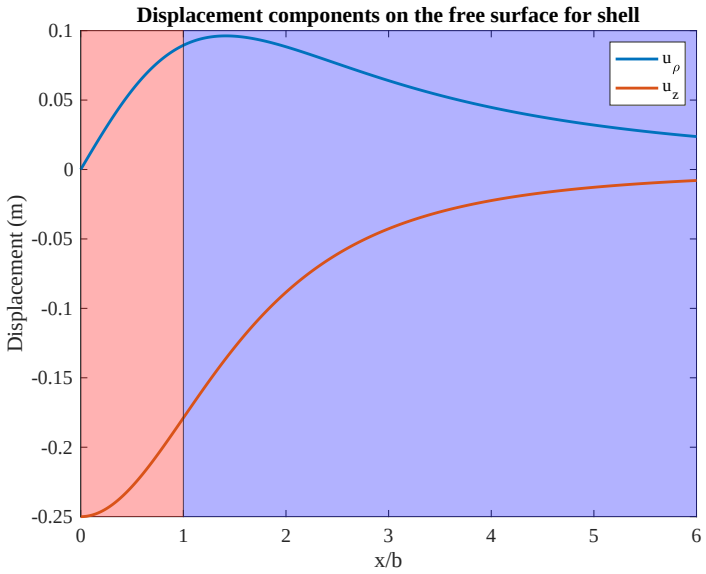

Figure 3.33: *Distribution of displacement components on the free surface ($z = 0$) as functions of the ratio x/b. The part of space corresponding to the projection of the TPE source on the surface, i.e., the $0 < x/b < 1$ half-plane, is shown in pink, while the part corresponding to the embedding matrix, i.e., the $x/b > 1$ half-plane, is colored purple.*

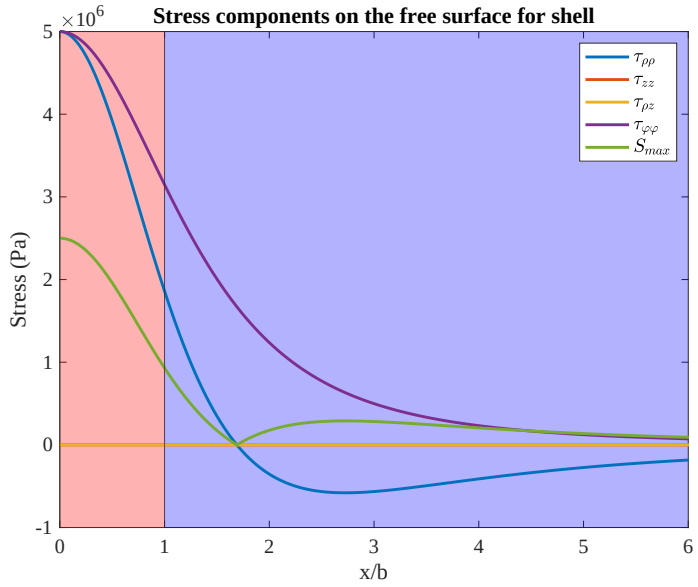

Figure 3.34: *Distribution of stress components on the free surface ($z = 0$) as functions of the ratio x/a. The part of space corresponding to the projection of the TPE source on the surface, i.e., the $0 < x/b < 1$ half-plane, is shown in pink, while the part corresponding to the embedding matrix, i.e., the $x/b > 1$ half-plane, is colored purple.*

We can analyze the diagonal deviatoric stress components on the free surface, shown in Fig. (3.35). Here, it is possible to notice that, for $x/a < 1.7$, $\tau'_{zz} = \sigma'_1 < 0$; while, for $x/a > 1.7$ we have that $\tau'_{zz} = \sigma'_2$. This suggests an extensive tectonic environment within the TPE inclusion and just outside it; while, in the other part of the domain, as τ'_{zz} becomes the intermediate eigenvalue of the deviatoric stress tensor, we should have a strike-slip regime. These results are similar to those obtained for the spherical TPE inclusion (Fig. 3.35).

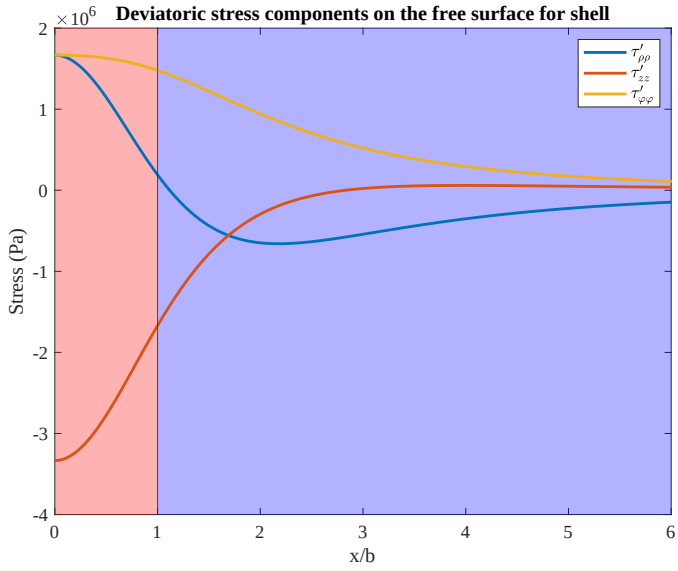

Figure 3.35: *Distribution of the diagonal deviatoric stress components on the free surface ($z = 0$) as functions of the ratio x/a. The interior of the TPE, i.e., the $x/b < 1$ half-plane, is shown in pink, while the embedding matrix, i.e., the $x/b > 1$ half-plane, is colored purple.*

3.2.5 Strain Field

In the following figures (Figg. 3.36; 3.37; 3.38; 3.39), the distributions of the non-zero components of the strain field are shown (respectively, ϵ_{zz}, $\epsilon_{\rho z}$, $\epsilon_{\rho\rho}$, and $\epsilon_{\varphi\varphi}$). These trends are similar to those obtained for the stress field, with the difference that the diagonal components have opposite sign within the TPE source. This behavior is analogous to what is observed in the case of the sphere and is explained in section (3.1.6).

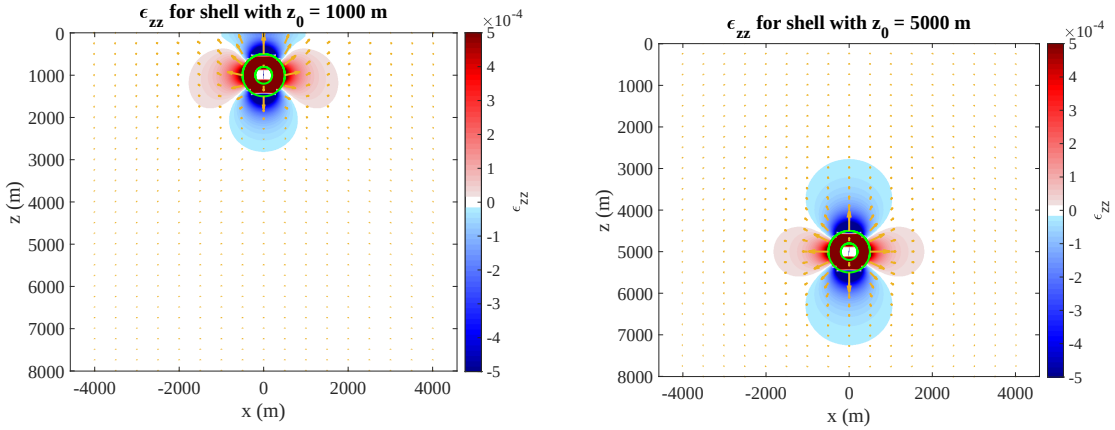

(a) **(b)**

Figure 3.36: *Distribution of ϵ_{zz} generated by a spherical shell TPE inclusion with inner radius $a = 200$ m and outer radius $b = 500$ m, with the center located in $z = z_0 = 1000$ m in the panel (a) and in $z_0 = 5000$ m in the panel (b), in the plane $y = 0$. The surface of the shell is highlighted with a green line. The color bar on the right of the picture represents the magnitude of ϵ_{zz} and the arrows represent the displacement field produced from the TPE inclusion.*

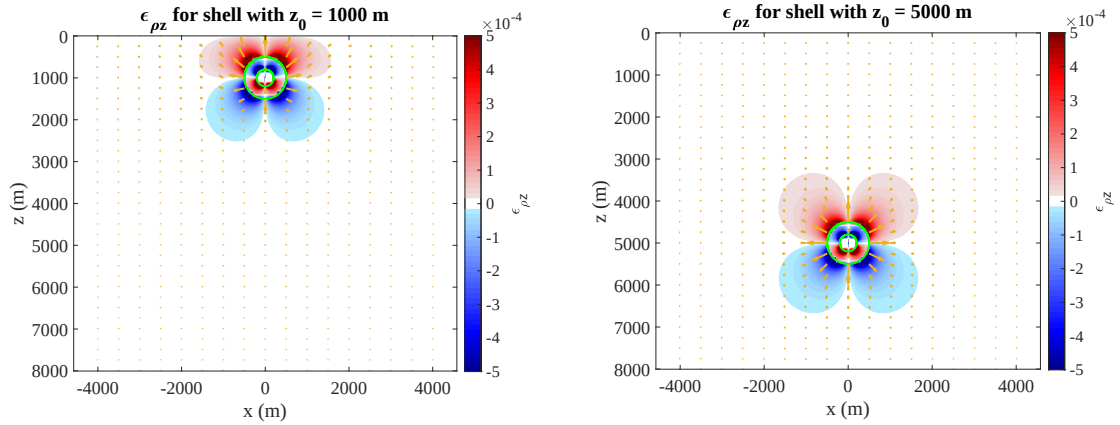

(a) **(b)**

Figure 3.37: *Distribution of $\epsilon_{\rho z}$ generated by a spherical shell TPE inclusion with inner radius $a = 200$ m and outer radius $b = 500$ m, with the center located in $z = z_0 = 1000$ m in the panel (a) and in $z_0 = 5000$ m in the panel (b), in the plane $y = 0$. The surface of the shell is highlighted with a green line. The color bar on the right of the picture represents the magnitude of $\epsilon_{\rho z}$ and the arrows represent the displacement field produced from the TPE inclusion.*

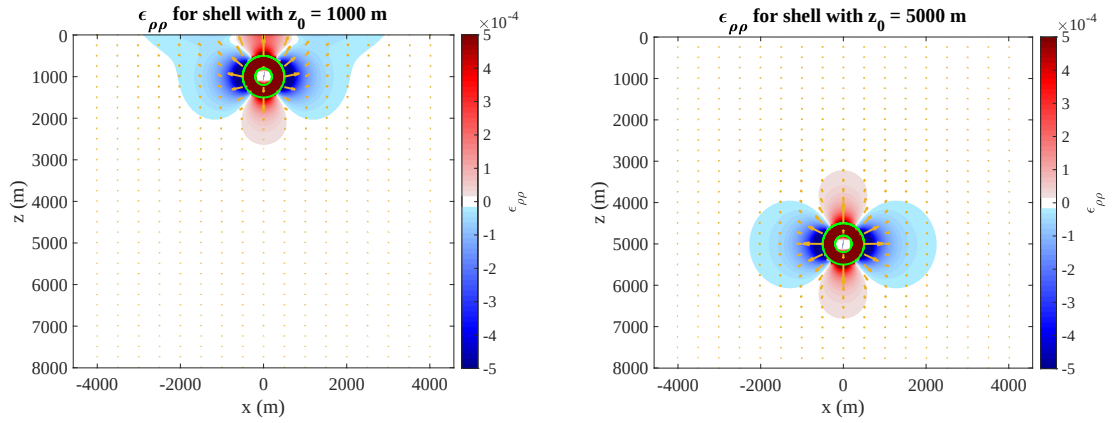

(a) **(b)**

Figure 3.38: *Distribution of $\epsilon_{\rho\rho}$ generated by a spherical shell TPE inclusion with inner radius $a = 200$ m and outer radius $b = 500$ m, with the center located in $z = z_0 = 1000$ m in the panel (a) and in $z_0 = 5000$ m in the panel (b), in the plane $y = 0$. The surface of the shell is highlighted with a green line. The color bar on the right of the picture represents the magnitude of $\epsilon_{\rho\rho}$ and the arrows represent the displacement field produced from the TPE inclusion.*

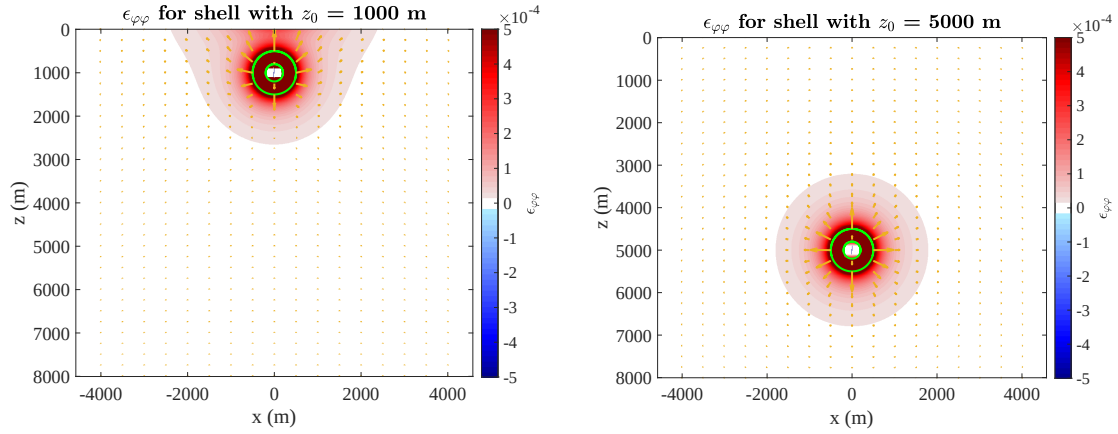

(a) (b)

Figure 3.39: *Distribution of $\epsilon_{\varphi\varphi}$ generated by a spherical shell TPE inclusion with inner radius $a = 200$ m and outer radius $b = 500$ m, with the center located in $z = z_0 = 1000$ m in the panel (a) and in $z_0 = 5000$ m in the panel (b), in the plane $y = 0$. The surface of the shell is highlighted with a green line. The color bar on the right of the picture represents the magnitude of $\epsilon_{\varphi\varphi}$ and the arrows represent the displacement field produced from the TPE inclusion.*

Fig. (3.40) represents the distribution of the cubic dilation ϵ_{kk} generated by a spherical shell TPE inclusion. It can be observed that the cubic dilation is predominantly positive both at $z = 0$ and at $z = 5000$ m. As shown in the case of the spherical TPE inclusion (Fig. 3.21), the distribution of ϵ_{kk} shows a positive volume change inside the sphere and an almost negligible one outside. To understand the variation in cubic dilation outside and inside the sphere, we can consider that on the surface the maximum value of ϵ_{kk} is $3.7 \cdot 10^{-4}$, while the maximum value on the equatorial plane is 0.023.

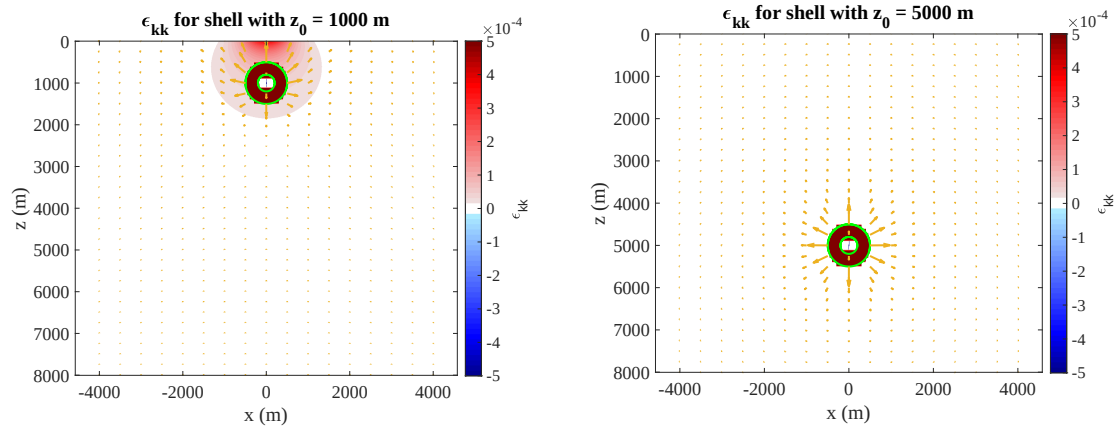

(a) (b)

Figure 3.40: *Distribution of the cubic dilation ϵ_{kk} generated by a spherical shell TPE inclusion with inner radius $a = 200$ m and outer radius $b = 500$ m, with the center located in $z = z_0 = 1000$ m in the panel (a) and in $z_0 = 5000$ m in the panel (b), in the plane $y = 0$. The surface of the shell is highlighted with a green line. The color bar on the right of the picture represents the magnitude of ϵ_{kk} and the arrows represent the displacement field produced from the TPE inclusion.*

Chapter 4

Discussion

The analytical model presented in this thesis provides explicit expressions for displacement, stress, and strain fields generated by a TPE source with spherical or spherical shell geometry, throughout the half-space $z \geq 0$, including the interior of the source. The surface $z = 0$ is stress-free and serves as a proxy for the Earth's surface.
Unlike Belardinelli et al. (2019), which derived such solutions for a TPE inclusion with spherical or spherical shell geometry in an unbounded medium (full-space), the present solutions include the fundamental effect of the free surface. This addition is crucial, as the Earth's surface is stress-free by nature ($\tau_{zz} = \tau_{\rho z} = 0$), making a model that includes it more accurate, albeit more complex. Furthermore, accounting for the free surface is essential when evaluating the deformation fields at the ground level, where most geophysical and geodetic measurements are collected. In particular, surface displacements allow us to compare with uplift (or subsidence) phenomena observed in volcanic and hydrothermal regions, stress and maximum shear stress provide insight into seismicity, while strain fields are necessary to study gravity changes, which are linked to variations in density and thus volume.

The use of simple geometries allows for a direct analytical description of the deformation fields induced by variations in pore pressure and temperature. Analytical models are therefore particularly useful for providing first-order estimates of deformation parameters and for understanding the fundamental physics governing a phenomenon.
A spherical source may serve as the simplest geometric representation of a reservoir where hot and pressurized fluids accumulate due to local increases in permeability, the latter of which may be enhanced by stress perturbations associated with the inflation of a nearby magma chamber.
In addition to the spherical TPE source, I considered the case in which a spherical Mogi source is embedded within a spherical shell characterized by TPE properties. This shell represents a physically distinct region, such as a damaged or fractured rock volume surrounding the magma chamber, which is capable of responding in a coupled way to variations in temperature, pore pressure, and deformation. During phases of pressure increase within the magma chamber, the stress field generated by the Mogi source, along with the temperature of the fluids within it, is transmitted to the TPE shell, according to thermo-poro-elastic behavior. The interaction between these effects may lead to localized fracturing, permeability changes, and fluid migration from the magma chamber to the outer TPE shell.
This type of modeling, which couples a Mogi source with a surrounding spherical TPE volume, allows for a realistic representation of the interactions between a pressurized

magma chamber and its immediate surroundings, especially in cases where geophysical signals related to fluid migration and induced seismicity are observed.

The results presented in chapter 3 clearly show that, as the source is located closer to the free surface, there is a progressive breakdown of symmetry with respect to the plane $z - z_0 = 0$. In general, representing the free surface becomes increasingly important as the inclusion gets shallower. Results indicate that when the source is at $z_0 = 5000$ m, differences in displacement and stress between the half-space (with free surface) and infinite medium models are much smaller than those when $z_0 = 1000$ m. For the displacement field, the largest relative variations are observed at the surface. Similarly, for the stress components τ_{zz} and $\tau_{\rho z}$, relative variations $\Delta\tau_{zz}/\tau^u_{zz}$ and $\Delta\tau_{\rho z}/\tau^u_{\rho z}$ (where the stress components labeled with the superscript "u" refer to the corresponding values in the full-space case) reach 100% at the surface, since these components are zero in an infinite medium but become non-zero in the presence of a free surface.
In the shallower case ($z_0 = 1000$ m), the maximum values of $\Delta\tau_{\rho\rho}/\tau^u_{\rho\rho}$ and $\Delta\tau_{\varphi\varphi}/\Delta\tau^u_{\varphi\varphi}$ are also observed at the surface, reaching values of approximately 80%.
Moreover, the figures showing the stress components generated by both inclusions (sphere and spherical shell) highlight that the normal component of the traction is continuous across the boundary of the inclusion. In particular, $\tau_{\rho\rho}$ is continuous along the x-axis (Fig. 3.5 and Fig. 3.26), τ_{zz} is continuous along the z-axis (Fig. 3.3 and Fig. 3.24), and $\tau_{\varphi\varphi}$ does not contribute to the normal traction, and therefore does not need to satisfy any continuity condition (Fig. 3.6 and Fig. 3.27).
Although this is not clearly visible in Fig. (3.4a), within the spherical source embedded in a half-space, the $\tau_{\rho z}$ component is not zero, even though it remains more than one order of magnitude smaller than the values outside the source. Indeed, as shown in Fig. (3.11), unlike the case without the free surface, the stress state within the source on the median plane is not completely isotropic, while outside the source it is not fully deviatoric.
In the case of the TPE shell, as shown in Fig. (3.30), the stress tensor within the inclusion is strongly (though not purely) deviatoric, and outside the source it is also not fully deviatoric, in contrast with the solutions obtained by Belardinelli et al. (2019).
As illustrated in Fig. (3.15), an extensional tectonic regime is observed at the surface, directly above and slightly beyond the vertical projection of the source at $z = 0$, while the rest of the domain is characterized by a strike-slip regime. This behavior is similar to with the results obtained for a thin-disk-shaped TPE source, as reported by Mantiloni et al. (2020). On the median plane, the stress regime is predominantly compressive. This result is also in good agreement with the case of the thin disk, with the difference that in the latter configuration a strike-slip regime is observed near the disk edges within the source.
It is important to note that a drawback of using a spherical TPE source is that, as shown in Fig. (3.7), the maximum shear stress inside the inclusion remains very low (compared to the case of a spherical TPE shell with same external radius cfr Fig. 3.28), which does not favor the occurrence of seismicity. Shear stress appears to be significantly higher in inclusions with anisotropic geometries, particularly when one dimension is much smaller than the others (e.g., disk-like shapes rather than spherical ones). This suggests that shear stress within TPE inclusions increases as the geometry becomes more flattened or elongated, i.e., as the width, thickness, and height differ more markedly. It is very important to take these results into account when comparing with real seismicity distributions (e.g. Nespoli et al., 2021). We will investigate more deeply the case of a

spherical TPE shell in the next subsection.

As shown in section (2.3.4), at the surface, the Mogi source, the TPE sphere and the TPE shell-shaped inclusion produce identical displacement, stress, and strain components for a suitable choice of parameters. This equivalence can make it particularly challenging to detect or confirm the presence of a TPE source based solely on surface measurements. The implications are significant: even when the internal physics of the system differs substantially, the surface response may remain indistinguishable, highlighting the importance of integrating other data that also depend on what happens at depth (e.g., seismicity or gravimetric measurements) in order to discriminate magmatic effects from hydrothermal ones.

4.1 Analysis of the maximum shear stress

Since the magnitude and spatial distribution of the maximum shear stress depend strongly on the geometry of the spherical TPE shell, I will focus on how $S_{\max}$ varies with the inner radius a of the shell. Numerical results (Figg. C.1 and C.2) show that for a spherical TPE inclusion ($a = 0$), the shear stress is one order of magnitude lower within its interior (around 10^6 Pa) than outside the inclusion (around 10^7 Pa). As the inner cavity increases in size, $S_{\max}$ rises significantly near the cavity wall, while still decaying steeply with distance (Fig. C.1a). Despite this, the internal stress profiles retain a similar shape when plotted against the normalized radial coordinate x/a, suggesting a form of self-similarity (Fig. C.1b).
Outside the shell (Fig. C.2), the trend reverses: increasing a leads to lower values of $S_{\max}$ in the surrounding medium. In this sense, the full-sphere case represents the configuration that maximizes the external shear stress, while hollowing the inclusion shifts the stress concentration inward. Notably, the external profiles do not collapse when normalized, indicating a lack of self-similarity in the surrounding domain.
These results highlight a redistribution of shear stress as the shell geometry changes: larger cavities (i.e., thinner shells) enhance stress localization within the shell and reduce the stress transmitted to the external medium.

4.2 Issues with the boundary condition on the inner spherical surface

As highlighted in section (1.3.4), the boundary condition on the internal spherical boundary must be satisfied at the inner surface of the TPE shell source, defined by the radius a. In spherical coordinates (r, θ, ϕ) (see Fig. 2.1 and Fig. 2.2), this condition requires that the normal stress τ_{rr} exerted by the deforming source on the surface $r = a$ equals the negative of the magma chamber pressure, i.e., $\tau_{rr}(r = a) = -P_0$. Such condition is fulfilled by the solution proposed by Belardinelli et al. (2019).

It is important to note that the procedure presented by Bonafede (1990), and followed in section (2.1) of this thesis, represents a first step toward determining the displacement, strain, and stress fields generated by a Mogi source in a semi-infinite medium. As shown by McTigue (1986) and further quantified by Battaglia et al. (2013), the introduction of the free surface inherently yields deviations from the ideal boundary condition for the case of the Mogi source. Indeed, the resulting surface displacement differs from the

correct one by approximately 12% for a source depth $z_0/a = 2$, and about 3% when $z_0/a = 3$ (Battaglia et al., 2013).

Hence, when applying the method described in section (2.1), which introduces the free surface to model of a spherical shell shaped TPE source embedded in an unbounded medium, we no longer have confirmation that the boundary condition on the internal spherical boundary is satisfied.
For the aforementioned considerations, when introducing the free surface, we could suppose that in the present model there is an error associated with the violation of the boundary condition $\tau_{rr}(r = a) = -P_0$, due to three contributions:

- the TPE shell itself;
- the Mogi source embedded within the shell;
- the interaction between the two sources.

In this section I describe the individual contributions of the TPE shell inclusion, neglecting the magma chamber located within it, and of a Mogi source with a radius equal to that of the shell's inner boundary (in absence of the surrounding TPE shell). The centers of both sources is the same and it is $z = z_0$.

Given the analytical expressions for the stress fields of both the shell and the Mogi source (the latter is obtained from the general expressions derived in section 2.3.3 by setting the stress-free strain $\epsilon_0 = 0$ and keeping $P_0 \neq 0$), it is possible to compute τ_{rr} and evaluate its deviation from the theoretical value $-P_0 = 10^7$ Pa at the inner boundary of the shell. Since the solutions presented in section (2.3.3) are expressed in cylindrical coordinates (ρ, φ, z), the evaluation of τ_{rr} is carried out at two specific locations where its computation becomes straightforward:

i) on the median plane ($z = z_0$, $\rho = a$), where $\tau_{rr} = \tau_{\rho\rho}$;

ii) along the vertical axis of the source ($z = z_0 - a$, $\rho = 0$), where $\tau_{rr} = \tau_{zz}$.

Initially, I performed these computations for a source centered at $z_0 = 1000$ m, with inner radius $a = 200$ m and outer radius $b = 500$ m (i.e., the reference configuration analyzed in chapter 3). On the median plane, the stress is $\tau_{rr} \simeq 1.013 \cdot 10^7$ Pa, corresponding to a relative error of 1.3%. On the vertical axis, we obtain $\tau_{rr} \simeq 1.126 \cdot 10^7$ Pa, which corresponds to a relative error of 12.6%. In both cases, the discrepancy remains below 15%, which is considered acceptable for the purposes of this study. The larger value occurring on the axis, is likely due to its 20% closer proximity to the free surface.

For the "internal" Mogi source, we consider a pressurized sphere located at the same depth $z_0 = 1000$ m, with radius $a = 200$ m and pressure $P_0 = -10^7$ Pa. In this configuration, the deviation from the theoretical value is only 0.05% on the mid-plane and 0.51% on the axis.

As further investigated in Appendix C, since both contributions are related to the influence of the free surface, the corresponding error increases as the center of the source is located closer to the plane $z = 0$. In general, we can observe that the error associated with the Mogi source represents an underestimation of the correct value and for both the shell and the internal Mogi source the error is greater when computed on the axis, likely due to its closer proximity to the free surface.
The evaluation of the stress along the axis (Fig. C.6; i.e., the most unfavorable case) reveals that, when the source center lies below a certain depth, the relative error falls

below a fixed threshold regardless all values of a. To further explore this behavior, Fig. (4.1) was generated. It shows that for $z_0 \geq 950$ m, the relative error remains consistently below 15% (as indicated by the red dashed line), for each value of a. This result implies that, for $z_0/b \gtrsim 2$, the solutions proposed in this work yield sufficiently accurate results.
Notably, the minimum depth satisfying this condition ($z_0 = 950$ m) closely corresponds to the configuration analyzed in chapter 3 ($z_0 = 1000$ m). In such a case, the full-space solution proposed by Belardinelli et al. (2019) proves inadequate for accurately reproducing surface displacements, even in the spherical case (i.e., when boundary conditions are not an issue; see, e.g., Fig. 3.1c and Fig. 3.2c). In particular, the absence of the free surface causes an underestimation of the uplift by 37% in both the sphere and shell cases when $z_0 = 1000$ m. Therefore, employing the half-space solution becomes essential for a reliable interpretation of surface deformation data.
We can conclude that, at least for $z_0/b \gtrsim 2$, the model developed in this thesis can be used to estimate the mechanical fields generated by a spherical shell-shaped TPE source.

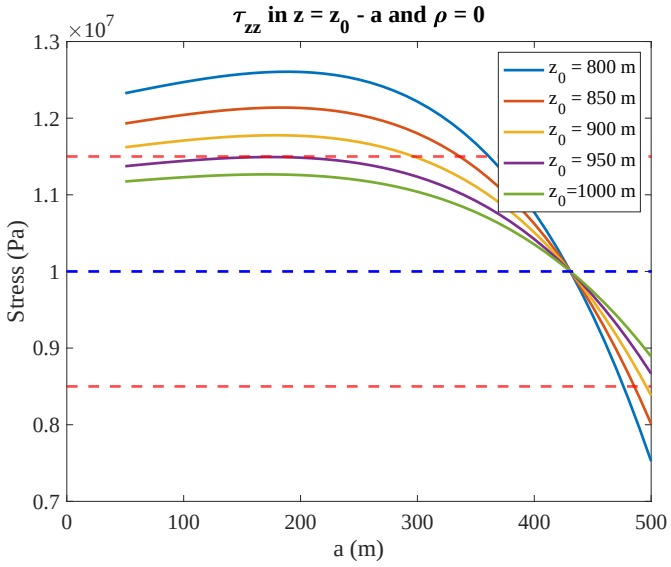

Figure 4.1: *Normal stress τ_{rr} generated by a spherical shell TPE inclusion as a function of the inner radius of the shell a for different values of z_0. The blue dashed line indicates the absence of error (i.e., $\tau_{rr} = -P_0$), while the red dashed line represents an error of* 15%.

As previously mentioned, to obtain a more accurate result, it would be necessary to apply a procedure analogous to the one proposed by McTigue (1986), suitably adapted to the specific problem addressed in this thesis. This represents one of the possible directions for future developments of the present work.

4.3 Applications and future developments of the model

A possible application of this thesis work, as already mentioned in section (1.1.2), concerns the study of unrest episodes at Vulcano Island. In fact, based on GNSS

and InSAR data collected during the 2018 and 2021 unrest episodes, one can perform inversions of deformation in unrest intervals to infer the features of the underlying deformation sources. Several models can be employed in this analysis, including the classical Mogi source (e.g., Bonafede 1990), the Compound Dislocation Model (CDM) (Nikkhoo and Rivalta, 2022), the thin-disk-shaped TPE inclusion model (Mantiloni et al. 2020), the spherical TPE source and the spherical shell TPE source, and allowing for comparison of the results obtained. It should be noted that in the case of the spherical shell TPE inclusion, particular care must be taken if the inversion of geodetic data suggests a shallow source ($z_0/b < 2$).

In addition to the application in the inversion of geophysical data, a promising future development of the model presented in this work involves extending McTigue (1986)'s corrections to a spherical shell and to the Mogi source within it. This refinement aims to reduce errors at all depths, ensuring a more accurate representation of subsurface processes.

The models considered in this thesis assume that pore pressure and temperature remain constant throughout the TPE region. A more realistic approach would allow these parameters to vary gradually towards the boundaries, simulating fluid propagation within the inclusion, either through analytical methods (e.g., Nespoli et al., 2023b) or by coupling with numerical simulators for modeling fluid flow in permeable media

Moreover, an important step forward in the TPE frameworks, especially relevant in volcanic and geothermal environments, would be to incorporate viscoelastic rheology into the solid matrix by using the correspondence principle (Fung and Drucker, 1966). This would enable the model to capture time-dependent deformation processes that can be triggered by high temperatures and pore pressures, such as thermally activated creep (Wang and Manga, 2021) and pressure solution creep (Gratier et al., 2012). By considering these effects, the model could more effectively simulate the mechanical behavior of geological materials under realistic conditions.

Finally, another potential improvement would be to apply Eshelby's method to different TPE inclusion geometries as an ellipsoidal one, in order to extend the analytical solutions to the description of reservoirs that do not necessarily have a spherical symmetry.

Chapter 5

Conclusive remarks

This thesis builds upon the work of Belardinelli et al. (2019), who applied Eshelby's method to derive analytical solutions for TPE sources with spherical symmetry embedded in an unbounded poro-elastic medium. Starting from those full-space solutions, I extended the analysis to the case of a semi-infinite poro-elastic medium bounded by a free surface. In particular, I derived analytical expressions for the displacement, strain, and stress components associated with a spherical TPE source placed within such a medium (section 2.2). Furthermore, I presented a first step toward obtaining analytical solutions for a spherical shell source (section 2.3). To incorporate the effects of the free surface, I employed both the image-source technique and the method described in section (2.1), as detailed in section (2.1) and Appendix B.

In chapter 3, I analyzed the spatial behavior of the displacement, strain and stress fields, as well as the maximum shear stress and the Coulomb failure function. Our results show that when the source is deeper, the field components closely approach those derived for a full-space configuration. Conversely, as the source approaches the surface, a clear loss of symmetry with respect to the horizontal plane ($z = z_0$) emerges due to the influence of the free boundary. At the surface, the stress components $\tau_{\rho z}$ and τ_{zz} vanish identically, as a consequence of the boundary conditions imposed by the image-source and Galerkin methods. This leads to a 100% relative variation when compared to the full-space solutions.

For both sources, the analysis of the deviatoric stress components reveals an extensional tectonic regime at the surface, near the vertical projection of the source, transitioning to strike-slip conditions farther away. On the equatorial plane within the source, the regime is predominantly compressive for the sphere and strike-slip for the shell; while, outside both inclusions, the stress state is compressive.

Regarding the spherical shell, I demonstrated that the solutions obtained here represent only an approximation. This is because the image-source technique, while satisfying boundary conditions at the free surface, does not fully enforce the boundary condition on the internal spherical boundary. I quantified the error in several configurations, all with an outer radius of 500 m but varying in inner radius and depth. Results show that the error, decreasing with increasing source depth, is consistently lower on the equatorial plane than along the polar axis. These observations will be revisited and extended in future work, incorporating the corrections proposed by McTigue (1986). However, as expressed in chapter 4, the solutions of Belardinelli et al. (2019) underestimate the uplift by 37% when the source center lies at a depth of $z_0 = 1$ km, due to the absence of the free surface. For the shell source, if the depth

is comparable to its outer radius (i.e., $z_{0,\min} \simeq 2b$), the error on the internal boundary condition is below 15% and decreases with increasing depth. Therefore, for $z_0 > z_{0,\min}$, the model developed in this thesis is more suitable than the unbounded model, as it more accurately estimates surface displacements while satisfying the internal boundary conditions within acceptable limits. Conversely, for $z_0 < z_{0,\min}$, neither model is appropriate: the shell model fails to satisfy the internal boundary condition, whereas the unbounded model neglects the free surface, leading to significant errors in the estimation of vertical displacement.

A key finding of this study (section 4.1) is that as the shell becomes thinner, the maximum shear stress inside the inclusion increases, showing self-similar behavior with respect to the normalized horizontal distance x/a. This is particularly important, as it may provide an explanation for seismicity occurring within the source, something not captured by a classical Mogi source.

Acknowledgements

I would like to express my deepest gratitude to my supervisors, Prof.ssa Maria Elina Belardinelli and Dr. Massimo Nespoli, for their constant guidance, patience, and invaluable insights throughout the development of this thesis. Their support has been fundamental not only for the scientific direction of this work, but also for my personal and academic growth. Working under their supervision has deepened my understanding of the discipline and strengthened my passion for research.

I sincerely thank my family for their unwavering support and encouragement during this academic journey. Special thanks to my friends for their understanding, motivation and for always being present, especially in the most challenging times.

Appendix A

Converting vectors and tensors from spherical to cylindrical coordinates

In order to convert a vector $\mathbf{u} = u_r\hat{e_r} + u_\theta\hat{\epsilon_\theta} + u_\phi\hat{u}_\phi$ from spherical coordinates (r, θ, ϕ) to cylindrical coordinates (ρ, φ, z) it is necessary to apply the two rotation matrix $\boldsymbol{Q}$ and $\boldsymbol{P}$:

$$\mathbf{u}(\rho, \varphi, z) = \mathbf{QPu}(r, \theta, \phi), \tag{A.1}$$

where $\mathbf{P}$ is:

$$\mathbf{P} = \begin{bmatrix} \sin\theta\cos\phi & \cos\theta\cos\phi & -\sin\theta \\ \sin\theta\sin\phi & \cos\theta\sin\phi & \cos\phi \\ \cos\theta & -\sin\theta & 0 \end{bmatrix} \tag{A.2}$$

and $\mathbf{Q}$ is:

$$\mathbf{Q} = \begin{bmatrix} \cos\varphi & -\sin\varphi & 0 \\ \sin\varphi & \cos\varphi & 0 \\ 0 & 0 & 1 \end{bmatrix}. \tag{A.3}$$

If one wants to orient the reference system with the z axis pointing downwards, one must apply the matrix $\mathbf{R}$, defined as follows:

$$\mathbf{R} = \begin{bmatrix} 1 & 0 & 0 \\ 0 & 1 & 0 \\ 0 & 0 & -1 \end{bmatrix}. \tag{A.4}$$

The final conversion for the displacement is:

$$\mathbf{u}(\rho, \varphi, z) = \mathbf{RQPu}(r, \theta, \phi). \tag{A.5}$$

The strain and the stress tensor, respectively $\mathbf{e}$ and $\boldsymbol{\tau}$, can be obtained with the following expressions:

$$\mathbf{e}(\rho, \varphi, z) = \mathbf{RQPe}(r, \theta, \phi)\mathbf{P^T Q^T R^T}. \tag{A.6}$$

$$\boldsymbol{\tau}(\rho, \varphi, z) = \mathbf{RQP}\boldsymbol{\tau}(r, \theta, \phi)\mathbf{P^T Q^T R^T}. \tag{A.7}$$

In our treatment we made a translation of the origin of the reference system, from $z = z_0$ to $z = 0$. The expression of the displacement, strain and stress fields are the following:

$$\mathbf{u}'(\rho, \varphi, z) = \mathbf{u}(\rho, \varphi, z - z_0); \quad \mathbf{e}'(\rho, \varphi, z) = \mathbf{e}(\rho, \varphi, z - z_0); \quad \boldsymbol{\tau}'(\rho, \varphi, z) = \boldsymbol{\tau}(\rho, \varphi, z - z_0). \tag{A.8}$$

By applying previous procedure we can obtain the conversion of the stress components, obtained from Belardinelli et al. (2019).

A.1 Stress components in cylindrical coordinates for a spherical TPE inclusion in an unbounded space

The expressions of the stress in eqq. (1.62) and (1.63) in cylindrical coordinates can be derived. By defining $R \doteq (\rho^2 + (z-z_0)^2)^{1/2}$:

$$\tau^I_{\rho\rho}(\rho,z) = \frac{2\mu}{3(1-2\nu)}\epsilon_1 a^3 \begin{cases} \frac{1+\nu}{a^3} - \frac{3(1+\nu)}{a^3}\frac{\epsilon_0}{\epsilon_1} & \text{if } R < a \\ \frac{1+\nu}{(\rho^2+(z-z_0)^2)^{3/2}} - \frac{3\left[(1-\nu)\rho^2+\nu(z-z_0)^2\right]}{(\rho^2+(z-z_0)^2)^{5/2}} & \text{if } R \geq a \end{cases}; \tag{A.9}$$

$$\tau^I_{\varphi\varphi}(\rho,z) = \frac{2\mu}{3(1-2\nu)}\epsilon_1 a^3 \begin{cases} \frac{1+\nu}{a^3} - \frac{3(1+\nu)}{a^3}\frac{\epsilon_0}{\epsilon_1} & \text{if } R < a \\ \frac{1-2\nu}{(\rho^2+(z-z_0)^2)^{3/2}} & \text{if } R \geq a \end{cases}; \tag{A.10}$$

$$\tau^I_{zz}(\rho,z) = \frac{2\mu}{3(1-2\nu)}\epsilon_1 a^3 \begin{cases} \frac{1+\nu}{a^3} - \frac{3(1+\nu)}{a^3}\frac{\epsilon_0}{\epsilon_1} & \text{if } R < a \\ \frac{1+\nu}{(\rho^2+(z-z_0)^2)^{3/2}} - \frac{3\left[\nu\rho^2+(1-\nu)(z-z_0)^2\right]}{(\rho^2+(z-z_0)^2)^{5/2}} & \text{if } R \geq a \end{cases}; \tag{A.11}$$

$$\tau^I_{\rho z}(\rho,z) = 2\mu\epsilon_1 a^3 \begin{cases} 0 & \text{if } R < a \\ -\frac{\rho(z-z_0)}{(\rho^2+(z-z_0)^2)^{5/2}} & \text{if } R \geq a \end{cases}. \tag{A.12}$$

A.2 Stress components in cylindrical coordinates for a spherical shell TPE inclusion in an unbounded space

The expressions of the stress components in eqq. (1.65) and (1.66) in cylindrical coordinates can be derived:

$$\tau^I_{\rho\rho}(\rho,z) \tag{A.13}$$
$$= \frac{2\mu}{1-2\nu} \begin{cases} \frac{P_0 a^3}{4\mu}\left(\frac{1+\nu}{R^3} - 3\frac{(1-\nu)\rho^2+\nu(z-z_0)^2}{R^5}\right) + \\ \quad + \frac{1}{3}\epsilon_1\left[(1+\nu)\left(1-\frac{a^3}{R^3}\right) + 3a^3\frac{(1-\nu)\rho^2+\nu(z-z_0)^2}{R^5}\right] - (1+\nu)\epsilon_0 & \text{if } a^2 \leq R^2 \leq b^2 \\ \left(\frac{P_0 a^3}{4\mu} + \frac{1}{3}\epsilon_1(b^3-a^3)\right)\left(\frac{1+\nu}{R^3} - 3\frac{(1-\nu)\rho^2+\nu(z-z_0)^2}{R^5}\right) & \text{if } R^2 > b^2 \end{cases};$$

$$\tau^I_{\varphi\varphi}(\rho,z) = 2\mu \begin{cases} \frac{P_0 a^3}{4\mu}\frac{1}{R^3} + \frac{1}{3}\epsilon_1\left(\frac{1+\nu}{1-2\nu} - \frac{a^3}{R^3}\right) - \frac{1+\nu}{1-2\nu}\epsilon_0 & \text{if } a^2 \leq R^2 \leq b^2 \\ \left(\frac{P_0 a^3}{4\mu} + \frac{1}{3}\epsilon_1(b^3-a^3)\right)\frac{1}{R^3} & \text{if } R^2 \geq b^2 \end{cases}; \tag{A.14}$$

$$\tau^I_{zz}(\rho,z) \tag{A.15}$$
$$= \frac{2\mu}{1-2\nu} \begin{cases} \frac{P_0 a^3}{4\mu}\left(\frac{1+\nu}{R^3} - 3\frac{\nu\rho^2+(1-\nu)(z-z_0)^2}{R^5}\right) + \\ \quad + \frac{1}{3}\epsilon_1\left[(1+\nu)\left(1-\frac{a^3}{R^3}\right) + 3a^3\frac{\nu\rho^2+(1-\nu)(z-z_0)^2}{R^5} - (1+\nu)\epsilon_0\right] & \text{if } a^2 \leq R^2 \leq b^2 \\ \left(\frac{P_0 a^3}{4\mu} + \frac{1}{3}\epsilon_1(b^3-a^3)\right)\left(\frac{1+\nu}{R^3} - 3\frac{\nu\rho^2+(1-\nu)(z-z_0)^2}{R^5}\right) & \text{if } R^2 > b^2 \end{cases};$$

$$\tau^I_{\rho z}(\rho,z) = -\begin{cases} \left(\frac{3}{2}P_0 a^3 - 2\mu\epsilon_1 a^3\right)\frac{\rho(z-z_0)}{R^5} & \text{if } a^2 \leq R^2 \leq b^2 \\ \left(\frac{3}{2}P_0 a^3 + 2\mu\epsilon_1(b^3-a^3)\right)\frac{\rho(z-z_0)}{R^5} & \text{if } R^2 > b^2 \end{cases}. \tag{A.16}$$

Appendix B

Complete solution for Z and u_i^Z

In the same way of $S_0(\rho)$, Z can be expanded through Hankel transform:

$$Z(\rho, z) = \int_0^\infty dc\ J_0(\rho c)\tilde{Z}(c, z), \tag{B.1}$$

where:

$$\tilde{Z}(c, z) = \int_0^\infty d\rho\ c\rho J_0(\rho c)Z(\rho, z). \tag{B.2}$$

An important property of Bessel's functions is required to solve the problem:

$$J_0''(x) + \frac{1}{x}J_0'(x) + J_0(x) = 0. \tag{B.3}$$

Due to linearity of previous equations and superposition principle, it is possible to consider one harmonic component at time, and, applying eq. (2.14) in eq. (B.1) it is possible to obtain:

$$\int_0^\infty dc\ J_0(\rho c)\left[\tilde{Z}^{(IV)}(c, z) - 2c^2\tilde{Z}^{(II)}(c, z) + c^4\tilde{Z}(c, z)\right] = 0, \tag{B.4}$$

where roman numerals in superscript represents the order of the derivative of the function with respect to z.
In order to obtain an expression for $\tilde{Z}(c, z)$ we can exploit the completeness property of Bessel functions $J_0(\rho c)$, requiring that:

$$\int_0^\infty d\rho\ \rho c J_0(\rho c)J_0(\rho c') = \delta(c' - c), \tag{B.5}$$

where $\delta(x)$ is the Dirac's delta function. In eq. (B.4) it is possible to multiply by $\rho J_0(c'\rho)$ and, after an integration in $d\rho$, we obtain the term in the square bracket evaluated in $c = c'$ must vanish. This last part results in a fourth-order homogeneous differential equation, in which the characteristic polynomial has two solutions $(\pm c)$ with multiplicity equal to two; hence, the general solution can be written in the form:

$$\tilde{Z}(c, z) = \left[(A + Bcz)e^{-cz} + (C + Dcz)e^{+cz}\right], \tag{B.6}$$

where A, B, C, D are coefficients to be determined and the factor c which multiplies z is placed in order to make dimensionally homogeneous previous coefficients. It is possible to observe that C and D must vanish because when $z \to +\infty$ the solution must be

bounded.
If one considers each single component $Z_c(\rho, z)$ of $Z(\rho, z)$:

$$Z_c(\rho, z) = J_0(c\rho)\tilde{Z}(c, z), \tag{B.7}$$

one can observe that it satisfies $\nabla^4 Z_c(\rho, z) = 0$ and stress components τ^c_{zi} obtained from Z_c according to eqq. (2.17) and (2.19); (2.18), obey boundary conditions derived from eq. (2.11).

$$\begin{cases} \tau^C_{\rho z} = 0 & \text{in } z = 0 \\ \tau^C_{zz} = -\tilde{S}_0(c)J_0(c\rho) & \text{in } z = 0 \end{cases}. \tag{B.8}$$

We can rewrite those conditions for the single component Z_c:

$$\begin{cases} \frac{\partial}{\partial \rho}\left[(1-\nu)\nabla^2 - \frac{\partial^2}{\partial z^2}\right] Z_c = 0 & \text{in } z = 0 \\ \frac{\partial}{\partial z}\left[(2-\nu)\nabla^2 - \frac{\partial^2}{\partial z^2}\right] Z_c = -\tilde{S}_0(c)J_0(c\rho) & \text{in } z = 0 \end{cases}. \tag{B.9}$$

By using eq. (B.6) and the fact that $C = D = 0$, eq. (B.7) becomes:

$$Z_c(\rho, z) = J_0(c\rho)(A + Bz)e^{-cz}. \tag{B.10}$$

Now, we can impose the first condition of eq. (B.9):

$$\frac{\partial}{\partial \rho}\left[(1-\nu)\nabla^2 - \frac{\partial^2}{\partial z^2}\right]\left(J_0(c\rho)(A + Bz)e^{-cz}\right) = 0. \tag{B.11}$$

The partial derivative $\frac{\partial}{\partial z}$ of the argument of eq. (B.11) is:

$$\frac{\partial}{\partial z}\left(J_0(c\rho)(A + Bz)e^{-cz}\right) = J_0(c\rho)\left(Be^{-cz} - c(A + Bz)e^{-cz}\right), \tag{B.12}$$

and the corresponding second derivative is:

$$\begin{aligned} \frac{\partial^2}{\partial z^2}\left(J_0(c\rho)(A + Bz)e^{-cz}\right) &= \frac{\partial}{\partial z}J_0(c\rho)\left(Be^{-cz} - c(A + Bz)e^{-cz}\right) \\ &= J_0(c\rho)\left(-2cB + c^2(A + Bz)\right)e^{-cz}, \end{aligned} \tag{B.13}$$

but in $z = 0$, this equation becomes:

$$\frac{\partial^2}{\partial z^2}\left(J_0(c\rho)(A + Bz)e^{-cz}\right)\Big|_{z=0} = J_0(c\rho)(-2cB + c^2A). \tag{B.14}$$

The expression of the Laplacian of an axi-symmetric function in cylindrical coordinate is the following:

$$\nabla \doteq \frac{\partial^2}{\partial \rho^2} + \frac{1}{\rho}\frac{\partial}{\partial \rho} + \frac{\partial^2}{\partial z^2}. \tag{B.15}$$

By using eq. (B.15) we get the Laplacian of the argument of eq. (B.11):

$$\begin{aligned} \nabla^2\left(J_0(c\rho)(A + Bz)e^{-cz}\right) &= \left(c^2 J_0''(c\rho) + \frac{c}{\rho}J_0'(c\rho)\right)(A + Bz)e^{-cz} \\ &\quad + J_0(c\rho)\left(-2cB + c^2(A + Bz)\right)e^{-cz}, \end{aligned} \tag{B.16}$$

which in $z = 0$, equals to:

$$\nabla^2 \left(J_0(c\rho)(A + Bz)e^{-cz} \right)\Big|_{z=0} = A \left(c^2 J_0''(c\rho) + \frac{c}{\rho} J_0'(c\rho) \right) + J_0(c\rho) \left(-2cB + c^2 A \right). \quad \text{(B.17)}$$

By multiplying eq. (B.17) for $(1 - \nu)$ and by adding the opposite of eq. (B.14) we obtain an expression that has to be differentiating with respect to ρ to reproduce the first equation in eq. (B.9):

$$\begin{aligned} \frac{\partial}{\partial \rho} \Bigg\{ \left[(1-\nu)c^2 \left(J_0''(c\rho) + \frac{1}{\rho c} J_0'(c\rho) + J_0(c\rho) \right) A - 2(1-\nu)cB J_0(c\rho) \right] \\ - J_0(c\rho)(-2cB + c^2 A) \Bigg\} = 0; \end{aligned} \quad \text{(B.18)}$$

by using eq. (B.3) and by doing some algebra we get:

$$\frac{\partial}{\partial \rho} \left[J_0(c\rho)(2c\nu B - c^2 A) \right] = 0. \quad \text{(B.19)}$$

Hence, we get:

$$A = \frac{2\nu B}{c}. \quad \text{(B.20)}$$

We can impose the second condition of eq. (B.9):

$$\frac{\partial}{\partial z} \left[(2-\nu)\nabla^2 - \frac{\partial^2}{\partial z^2} \right] \left(J_0(c\rho)(A + Bz)e^{-cz} \right) = -\tilde{S}_0(c) J_0(c\rho). \quad \text{(B.21)}$$

We have already computed the second derivative with respect to z and the Laplacian of the argument in the first term of equation (B.21), which are respectively given in equations (B.13) and (B.16). By differentiating with respect to z the second derivative, we obtain:

$$\frac{\partial}{\partial z} \frac{\partial^2}{\partial z^2} \left[J_0(c\rho) \left(A + Bz \right) e^{-cz} \right] = J_0(c\rho) \left(3c^2 B e^{-cz} - c^3 (A + Bz) e^{-cz} \right), \quad \text{(B.22)}$$

and, in $z = 0$, we get:

$$\frac{\partial}{\partial z} \frac{\partial^2}{\partial z^2} \left[J_0(c\rho) \left(-2cBe^{-cz} + c^2 (A + Bz) e^{-cz} \right) \right] \Big|_{z=0} = J_0(c\rho) c^2 \left(3B - cA \right). \quad \text{(B.23)}$$

The partial derivative with respect to z of eq. (B.16) is:

$$\begin{aligned} &\frac{\partial}{\partial z} \left[\left(c^2 J_0''(c\rho) + \frac{c}{\rho} J_0'(c\rho) \right) (A + Bz) e^{-cz} + J_0(c\rho) \left(-2cB + c^2 (A + Bz) \right) e^{-cz} \right] \\ &= c^2 \left(J_0''(c\rho) + \frac{1}{c\rho} J_0'(c\rho) \right) \left(B - c(A + Bz) \right) e^{-cz} + J_0(c\rho) \left(Bc^2 + 2c^2 B - c^3 (A + Bz) \right) e^{-cz}. \end{aligned} \quad \text{(B.24)}$$

The previous expression, in $z = 0$, takes the form as follows:

$$\frac{\partial}{\partial z} \nabla^2 \left(J_0(c\rho)(A + Bz)e^{-cz} \right) \Big|_{z=0} = \left(J_0''(c\rho) + \frac{1}{c\rho} J_0'(c\rho) \right) \left(B - cA \right) c^2 + J_0(c\rho) c^2 \left(3B - cA \right). \quad \text{(B.25)}$$

To solve eq. (B.21), we multiply eq. (B.25) by $(2-\nu)$ and add the opposite of eq. (B.23). Applying these operations, we obtain:

$$(2-\nu)\left(J_0''(c\rho)+\frac{1}{c\rho}J_0'(c\rho)\right)c^2(B-cA)+(1-\nu)J_0(c\rho)c^2(3B-cA), \tag{B.26}$$

and, by using eq. (B.3), we obtain:

$$(2-\nu)c^2\left(-J_0(c\rho)\right)(B-cA)+(1-\nu)J_0(c\rho)c^2(3B-cA). \tag{B.27}$$

Now, by imposing the conditions given in eq. (B.21) and in eq. (B.20), we obtain the value of the coefficient B:

$$B=-\frac{\tilde{S}_0}{c^3}. \tag{B.28}$$

Once the coefficient B has been determined, equation (B.20) can be used to obtain the coefficient A:

$$A=2\nu B=-2\nu\frac{\tilde{S}_0}{c^3}. \tag{B.29}$$

The expression of $S_0(\rho)$, needed to continue the treatment, can be determined from the condition:

$$S_0(\rho)=\tau_{zz}^{II}(z=0). \tag{B.30}$$

From eq. (2.9), we have that eq. (B.30) assumes the following form:

$$S_0(\rho)=\tau_{zz}^{II}(z=0)=-\frac{4}{3}\mu\epsilon_1 a^3\left(\frac{3z_0^2}{(\rho^2+z_0^2)^{5/2}}-\frac{1}{(\rho^2+z_0^2)^{3/2}}\right). \tag{B.31}$$

By substituting eq. (B.31) into eq. (2.13) we have:

$$\tilde{S}_0(c)=\int_0^\infty d\rho\ c\rho J_0(\rho c)\left[-\frac{4}{3}\mu\epsilon_1 a^3\left(\frac{3z_0^2}{(\rho^2+z_0^2)^{5/2}}-\frac{1}{(\rho^2+z_0^2)^{3/2}}\right)\right]. \tag{B.32}$$

The second part of the integral is:

$$\int_0^\infty d\rho\ \frac{\rho J_0(c\rho)}{(\rho^2+z_0^2)^{3/2}}. \tag{B.33}$$

This integral is tabulated in Gradshteyn and Ryzhik (2014). The general solution of the integral is:

$$\int_0^\infty dt\ \frac{t^{\zeta+1}J_\zeta(ct)}{(t^2+z_0^2)^{\chi+1}}=\frac{c^\chi z_0^{\zeta-\chi}}{2^\chi\Gamma(\chi+1)}K_{\zeta-\chi}(cz_0), \tag{B.34}$$

where K_α is the modified Bessel function of the second kind:

$$K_\alpha(x)=\int_0^\infty dm\ e^{-x\cosh m}\cosh\alpha m, \tag{B.35}$$

and $\Gamma(l)$ is the Gamma function, defined as follows:

$$\Gamma(l)=\int_0^\infty dn\ n^{l-1}e^{-n};\qquad \mathcal{R}(l)>0. \tag{B.36}$$

The modified Bessel function of the second kind can be developed by asymptotic expansion (Abramowitz and Stegun, 1972):

$$K_\alpha(x) \simeq \sqrt{\frac{\pi}{2x}} e^{-x} \left(1 + \frac{(4\alpha^2-1)}{8x} + \frac{(4\alpha^2-1)(4\alpha^2-9)}{2!\,(8x)^2} - \frac{(4\alpha^2-1)(4\alpha^2-9)(4\alpha^2-25)}{3!\,(8x)^3} + ...\right). \tag{B.37}$$

By comparing eq. (B.33) and eq. (B.34) we can set $t = \rho$, $\zeta = 0$, $\chi = 1/2$ and we have:

$$\int_0^\infty d\rho \, \frac{\rho J_0(c\rho)}{(\rho^2 + z_0^2)^{3/2}} = \sqrt{\frac{c}{2z_0}} \frac{1}{\Gamma(3/2)} K_{-1/2}(cz_0). \tag{B.38}$$

By using eq. (B.37) for $\alpha = -1/2$ we can notice that the only non-vanishing term is the first one:

$$K_{-1/2}(cz_0) = \sqrt{\frac{\pi}{2cz_0}} e^{-cz_0}, \tag{B.39}$$

hence, by using eq. (B.36) for $l = 3/2$ (we get $\Gamma(3/2) = \sqrt{\pi}/2$), the result of eq. (B.38) is:

$$\int_0^\infty d\rho \, \frac{\rho J_0(c\rho)}{(\rho^2 + z_0^2)^{3/2}} = \frac{e^{-cz_0}}{z_0}. \tag{B.40}$$

The second part of the integral is:

$$\int_0^\infty d\rho \, \frac{\rho J_0(c\rho)}{(\rho^2 + z_0^2)^{5/2}}. \tag{B.41}$$

By comparing eq. (B.41) and eq. (B.34) we can set $t = \rho$, $\zeta = 0$, $\chi = 3/2$ and we have:

$$\int_0^\infty d\rho \, \frac{\rho J_0(c\rho)}{(\rho^2 + z_0^2)^{5/2}} = \sqrt{\frac{c^3}{(2z_0)^3}} \frac{1}{\Gamma(5/2)} K_{-3/2}(cz_0). \tag{B.42}$$

By using eq. (B.37) for $\alpha = -3/2$ we can notice that, for $K_{-3/2}(cz_0)$, the only non-vanishing terms are the first two:

$$K_{-3/2}(cz_0) = \sqrt{\frac{\pi}{2cz_0}} e^{-cz_0} \left(1 + \frac{1}{cz_0}\right) \tag{B.43}$$

hence, by using eq. (B.36) for $l = 5/2$ (we get $\Gamma(5/2) = 3\sqrt{\pi}/4$), the result of eq. (B.38) is:

$$\int_0^\infty d\rho \, \frac{\rho J_0(c\rho)}{(\rho^2 + z_0^2)^{5/2}} = \frac{c}{3z_0^2} \left(1 + \frac{1}{cz_0}\right) e^{-cz_0}. \tag{B.44}$$

Now, we can introduce the results expressed in eqq. (B.40) and (B.44) into eq. (B.32), obtaining:

$$\tilde{S}_0(c) = -\frac{4}{3} \mu \epsilon_1 a^3 c^2 e^{-cz_0}. \tag{B.45}$$

In order to obtain the expression of $Z(\rho, z)$ it is necessary to determine the single component $Z_c(\rho, z)$ from eq. (B.7):

$$Z_c(\rho, z) = +\frac{4}{3} \mu \epsilon_1 \frac{a^3}{c} (2\nu + cz) e^{-c(z+z_0)} J_0(c\rho), \tag{B.46}$$

where we substituted the values of $\tilde{S}_0(c)$ into the expressions of A and B in eqq. (B.29) and (B.28), and then, those values in eq. (B.6).
From eq. (2.15) and eq. (2.16) it is possible to determine the expression of the components of the displacement associated to Z_c:

$$2\mu u_\rho^c = +\frac{4}{3}\mu\epsilon_1 a^3 J_1(\rho c)(1-2\nu-cz)ce^{-c(z+z_0)}; \tag{B.47}$$

$$2\mu u_z^c = -\frac{4}{3}\mu\epsilon_1 a^3 J_0(\rho c)\left[2(1-\nu)+cz\right]ce^{-c(z+z_0)}. \tag{B.48}$$

It is important to notice that in eq. (B.47) it was used that $J_1(x) = -\frac{d}{dx}J_0(x)$, while in eq. (B.48) it was used the property expressed in eq. (B.3).
The final step in determining u_z^Z and u_ρ^Z is to integrate u_z^c and u_ρ^c in dc, according with the superposition principle. By starting with u_z^Z we obtain:

$$2\mu u_z^Z = -\frac{4}{3}\mu\epsilon_1 a^3 \int_0^\infty dc\ J_0(\rho c)\left[2(1-\nu)+cz\right]ce^{-c(z+z_0)}. \tag{B.49}$$

Except for multiplicative constants, the first part of the integral is:

$$\int_0^\infty dc\ J_0(\rho c)ce^{-c(z+z_0)}. \tag{B.50}$$

This integral is tabulated in Gradshteyn and Ryzhik (2014). The general solution of the integral is:

$$\int_0^\infty dt\ e^{-\gamma t}J_\zeta(\beta t)t^{\zeta+1} = \frac{2\gamma(2\beta)^\zeta\Gamma(\zeta+3/2)}{\sqrt{\pi}(\gamma^2+\beta^2)^{\zeta+3/2}}. \tag{B.51}$$

By comparing eq. (B.50) and eq. (B.51) we can set $t = c$, $\zeta = 0$, $\gamma = (z+z_0)$, $\beta = \rho$ and, by using eq. (B.36) for $l = 3/2$ (we get $\Gamma(3/2) = \sqrt{\pi}/2$), we have:

$$\int_0^\infty dc\ J_0(\rho c)ce^{-c(z+z_0)} = \frac{(z+z_0)}{((z+z_0)^2+\rho^2)^{3/2}}. \tag{B.52}$$

The first part of the integral in eq. (B.32) is proportional to:

$$\int_0^\infty dc\ J_0(\rho c)c^2e^{-c(z+z_0)}. \tag{B.53}$$

This integral is also tabulated in Gradshteyn and Ryzhik (2014). The general solution of the integral is:

$$\int_0^\infty dt\ e^{-\gamma t}J_\zeta(\beta t)t^{\chi-1} = (\gamma+\beta)^{-1/2\chi}\Gamma(\zeta+\chi)P_{\chi-1}^{-\zeta}\left[\gamma(\gamma^2+\beta^2)^{-1/2}\right], \tag{B.54}$$

where $P_l^m(x)$ is the associated Legendre polynomial of degree l and order m. By comparing eq. (B.53) and eq. (B.54) we can set $t = c$, $\zeta = 0$, $\chi = 3$, $\gamma = (z+z_0)$, $\beta = \rho$, so that the integral in eq. (B.53) is proportional to the second order Legendre polynomial:

$$P_2^0\left[\frac{(z+z_0)}{((z+z_0)^2+\rho^2)^{1/2}}\right] = \frac{1}{2}\left[\frac{2(z+z_0)^2-\rho^2}{(z+z_0)^2+\rho^2}\right], \tag{B.55}$$

where I used the relation $P_2^0(x) = \frac{1}{2}(3x^2-1)$, and since $\Gamma(3) = 2$, we get:

$$\int_0^\infty dc\ J_0(\rho c)c^2e^{-c(z+z_0)} = \frac{2(z+z_0)^2-\rho^2}{((z+z_0)^2+\rho^2)^{5/2}}. \tag{B.56}$$

By combining eqq. (B.49) and (B.52); (B.56) we get the expression of $u_z^Z(\rho, z)$:

$$u_z^Z(\rho,z) = -\frac{2}{3}\epsilon_1 a^3 \left[2(1-\nu)\frac{z+z_0}{((z+z_0)^2+\rho^2))^{3/2}} - \frac{z}{((z+z_0)^2+\rho^2))^{3/2}} + \frac{3z(z+z_0)^2}{((z+z_0)^2+\rho^2))^{5/2}}\right]. \tag{B.57}$$

By proceeding with u_ρ^Z we obtain:

$$2\mu u_\rho^Z = +\frac{4}{3}\mu\epsilon_1 a^3 \int_0^\infty dc\ J_1(\rho c)[1-2\nu-cz]ce^{-c(z+z_0)}. \tag{B.58}$$

Except for multiplicative constants the first part of the integral is:

$$\int_0^\infty dc\ J_1(\rho c)ce^{-c(z+z_0)}, \tag{B.59}$$

and, by comparing eq. (B.59) and eq. (B.54) we can set $t = c$, $\zeta = 1$, $\chi = 2$, $\gamma = (z+z_0)$, $\beta = \rho$. Here it shows up the associated Legendre polynomial of degree 1 and order -1:

$$P_1^{-1}\left[\frac{(z+z_0)}{(\rho^2+(z+z_0)^2)^{1/2}}\right] = -\left[\frac{\rho^2}{\rho^2+(z+z_0)^2}\right]^{1/2}, \tag{B.60}$$

where we used the relation $P_1^{-1}(x) = -(1-x^2)^{1/2}$, and since $\Gamma(3) = 2$, we get:

$$\int_0^\infty dc\ J_1(\rho c)ce^{-c(z+z_0)} = \frac{\rho}{((z+z_0)^2+\rho^2)^{3/2}}. \tag{B.61}$$

The second part of the integral is proportional to:

$$\int_0^\infty dc\ J_1(\rho c)c^2e^{-c(z+z_0)}, \tag{B.62}$$

and, by comparing eq. (B.59) and eq. (B.51) we can set $t = c$, $\zeta = 1$, $\gamma = (z+z_0)$, $\beta = \rho$. The result of eq. (B.62) is

$$\int_0^\infty dc\ J_1(\rho c)c^2e^{-c(z+z_0)} = \frac{3\rho(z+z_0)}{(\rho^2+(z+z_0)^2)^{5/2}}. \tag{B.63}$$

By combining eqq. (B.58) and (B.61); (B.63) we get the expression of $u_\rho^Z(z, \rho)$:

$$u_\rho^Z = \frac{2}{3}\epsilon_1 a^3 \left[(1-2\nu)\frac{\rho}{((z+z_0)^2+\rho^2)^{3/2}} - \frac{3z(z+z_0)\rho}{((z+z_0)^2+\rho^2)^{5/2}}\right]. \tag{B.64}$$

Appendix C

Auxiliary figures supporting the discussion

Fig. (C.1) and Fig. (C.2) show the maximum shear stress $S_{\max}$ generated by spherical shells of difference geometries, respectively, within and outside the source. In particular, the center of the shell is fixed at a depth of $z_0 = 1000$ m, and the outer radius is kept constant at $b = 500$ m. On the other hand, the inner radius a varies from 0 m (i.e., spherical source) up to 400 m, in increments of 100 m.

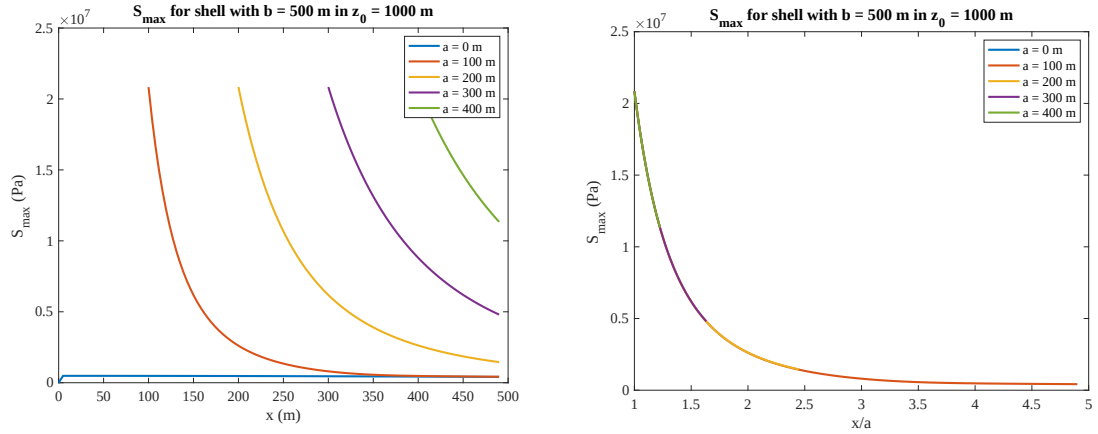

(a) **(b)**

Figure C.1: *Maximum shear stress S_{max} generated by spherical shells of different geometries (i.e., varying inner radius a), evaluated on the median plane $z = z_0 = 1000$ m and within the shell. Panel (a) shows the variation of S_{max} as a function of x, while panel (b) displays the same quantity as a function of the normalized coordinate x/a.*

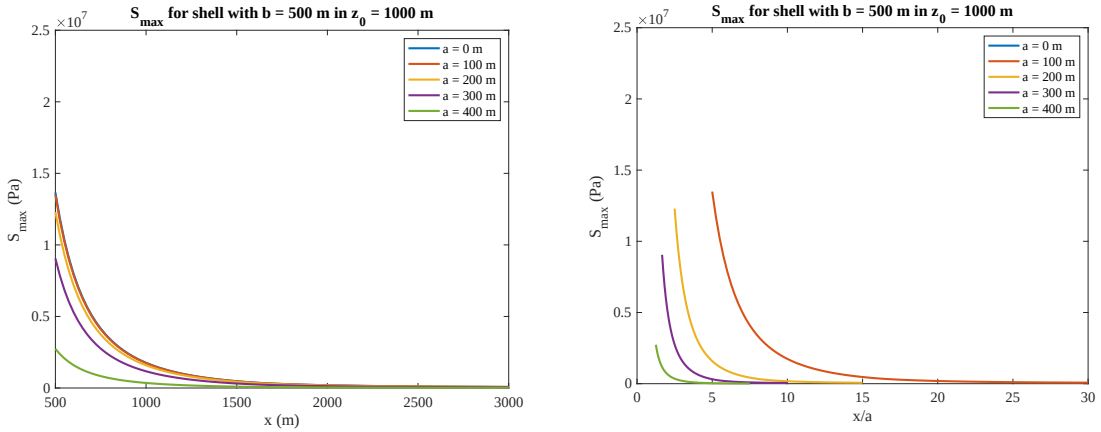

(a) **(b)**

Figure C.2: *Maximum shear stress S_{max} generated by spherical shells of different geometries (i.e., varying inner radius a), evaluated on the median plane $z = z_0 = 1000$ m and outside the shell. Panel (a) shows the variation of S_{max} as a function of x, while panel (b) displays the same quantity as a function of the normalized coordinate x/a.*

To further investigate the behavior discussed in section (4.2), a set of plots (Fig. C.3 and Fig. C.4) was produced showing the variation of τ_{rr} as a function of the source depth z_0, for different values of the radius a, keeping $b = 500$ m constant. This last reference value is relevant only for the contribution of the shell, since in the case of the Mogi source the terms involving b vanish when $\epsilon_1 = 0$ is imposed; indeed, in this configuration, for $r > a$, the medium corresponds solely to the embedding matrix.
Both errors decrease with increasing z_0 for a fixed a.
In the median plane (Fig C.3), for any value of a, the shell error falls below 10% already at $z_0 \simeq 700$ m, while on the axis this occurs only at significantly greater depth ($z_0 \simeq 1100$ m). However, in the axis (Fig. C.4), for $z_0 \geq 700$ m, the error remains below 25%. In general, the error is greater when computed on the axis, likely due to its closer proximity to the free surface.
At the minimum depth analyzed ($z_0 = 500$ m), the maximum error on the median plane for the shell remains below 14%, while for the Mogi error is below 5%.

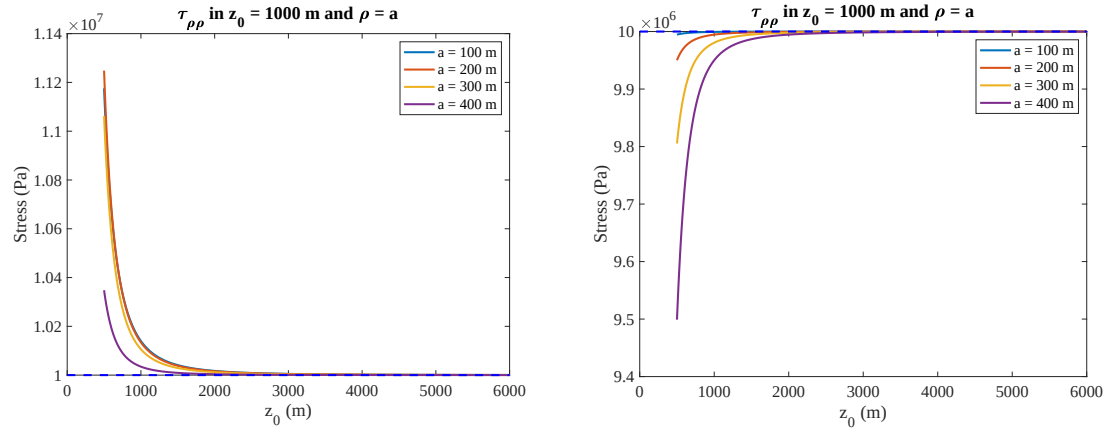

(a) **(b)**

Figure C.3: *Panel (a) shows τ_{rr} generated by a spherical shell TPE inclusion as a function of the vertical coordinate of the center of the source z_0 for different values of the inner radius a. Panel (b) shows the same plot for the Mogi source. The dashed line indicates the absence of error, i.e., $\tau_{rr} = -P_0$.*

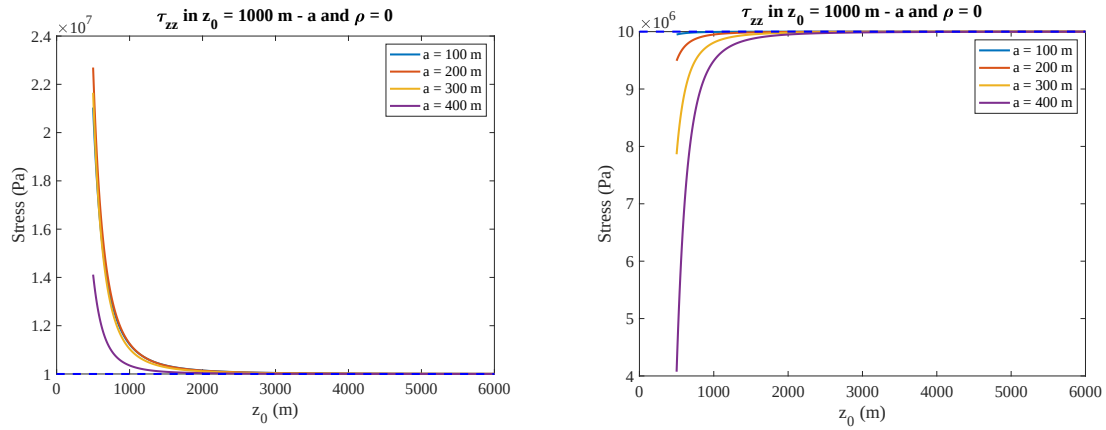

(a) **(b)**

Figure C.4: *Panel (a) shows τ_{rr} generated by a spherical shell TPE inclusion as a function of the vertical coordinate of the center of the source z_0 for different values of the inner radius a. Panel (b) shows the same plot for the Mogi source. The dashed line indicates the absence of error, i.e., $\tau_{rr} = -P_0$.*

We have also analyzed the trend of τ_{rr} as a function of the radius a for fixed depth z_0 (Fig. C.5a and Fig. C.6a). Also in this case, the behavior differs between the shell and the Mogi source; in particular, for the shell, the stress variation is non-monotonic. A zero error is obtained at $a \simeq 435$ m for each z_0. For $a < 435$ m, the shell overestimates the correct value (positive error), whereas for $a > 435$ m, it underestimates it (negative error). In the range $a < 435$ m, for deeper sources (e.g., $z_0 = 700 - 800$ m), the curve is nearly monotonic: as the inner radius a increases, the calculated stress converges toward the target value. By contrast, for shallower sources (e.g., $z_0 = 500$ m) the error grows to a peak and then declines. These positive and negative errors should be added to that of the Mogi source to provide a complete picture of the total stress deviation.
For the Mogi source (Fig. C.5b and Fig. C.6b), the behavior is nearly monotonic with increasing a, and the stress consistently underestimates the correct value.
Finally, as expected, for $a = 500$ m, the stress value of the Mogi source matches that of the shell.
In the median plane (Fig. C.5a), for the shallowest depth considered $z_0 = 500$ m, the shell error remains below 5% within the interval $a \in [390; 460]$ m. Within the same range, the Mogi source error (Fig. C.5b) lies between 5% and 8%, leading to a combined maximum error below 13%.

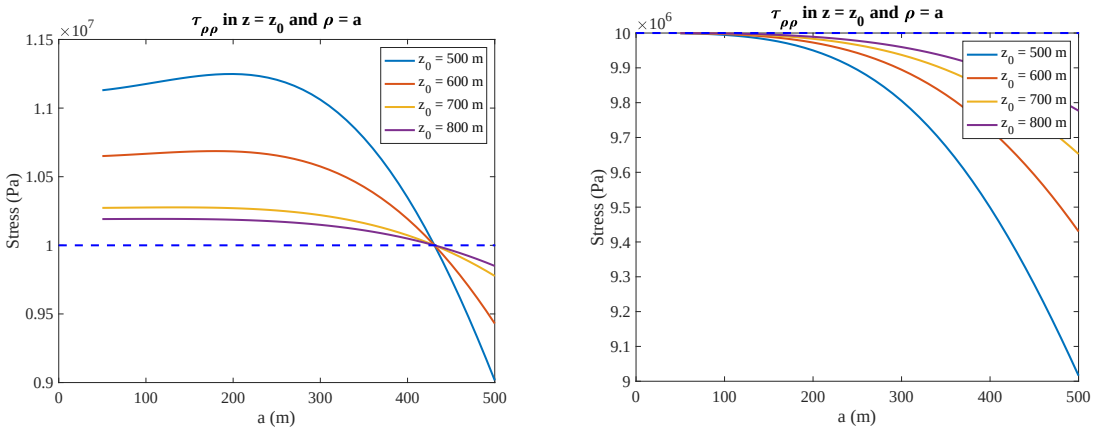

(a) **(b)**

Figure C.5: *Panel (a) shows τ_{rr} generated by a spherical shell TPE inclusion as a function of the inner radius of the shell a for different values of z_0. Panel (b) shows the same plot for the Mogi source. The dashed line indicates the absence of error, i.e., $\tau_{rr} = -P_0$.*

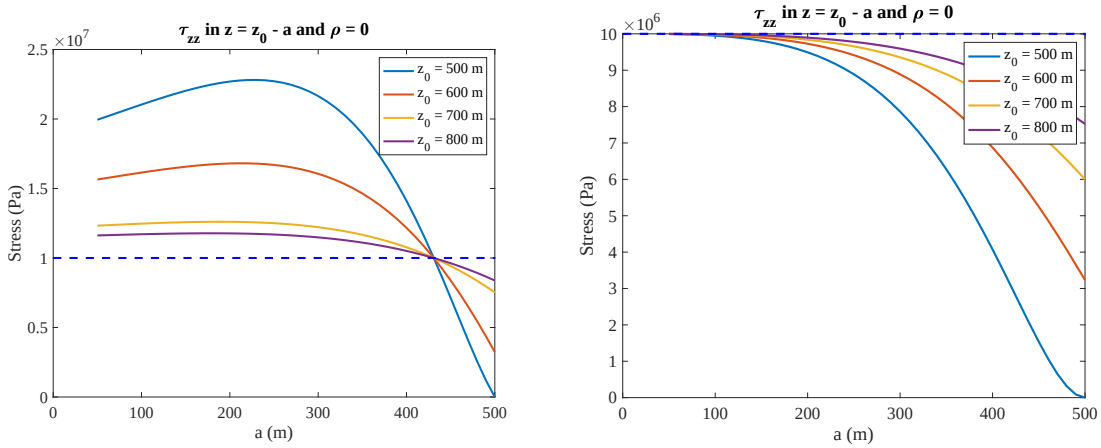

(a) **(b)**

Figure C.6: *Panel (a) shows τ_{rr} generated by a spherical shell TPE inclusion as a function of the inner radius of the shell a for different values of z_0. Panel (b) shows the same plot for the Mogi source. The dashed line indicates the absence of error, i.e., $\tau_{rr} = -P_0$.*

Bibliography

Abramowitz, M. and Stegun, I. A. (1972). *Handbook of mathematical functions*. Dover Pub., New York.

Aiuppa, A., Bitetto, M., Calabrese, S., Delle Donne, D., Lages, J., La Monica, F. P., Chiodini, G., Tamburello, G., Cotterill, A., Fulignati, P., et al. (2022). Mafic magma feeds degassing unrest at vulcano island, italy. *Communications Earth & Environment*, 3(1):255.

Aki, K. and Richards, P. (2002). *Quantitative Seismology*. University Science Books.

Barbano, M. S., Castelli, V., and Pirrotta, C. (2017). Materiali per un catalogo di eruzioni di vulcano e di terremoti delle isole eolie e della sicilia nordorientale (secc. xv-xix). *Quaderni di Geofisica*, 143.

Battaglia, M., Cervelli, P., and Murray, J. (2013). Modeling crustal deformation near active faults and volcanic centers—a catalog of deformation models: U.s. geological survey techniques and methods. 13:175–185.

Belardinelli, M., Bonafede, M., and Nespoli, M. (2019). Stress heterogeneities and failure mechanisms induced by temperature and pore-pressure increase in volcanic regions. *Earth and Planetary Science Letters*, 525:115765.

Belardinelli, M. E., Nespoli, M., and Bonafede, M. (2022). Stress changes caused by exsolution of magmatic fluids within an axisymmetric inclusion. *Geophysical Journal International*, 230(2):870–892.

Biot, M. A. (1941). General theory of three-dimensional consolidation. *Journal of applied physics*, 12(2):155–164.

Bonafede, M. (1990). Axi-symmetric deformation of a thermo-poro-elastic half-space: inflation of a magma chamber. *Geophysical Journal International*, 103(2):289–299.

Chiodini, G., Caliro, S., Avino, R., Bini, G., Giudicepietro, F., De Cesare, W., Ricciolino, P., Aiuppa, A., Cardellini, C., Petrillo, Z., et al. (2021). Hydrothermal pressure-temperature control on co2 emissions and seismicity at campi flegrei (italy). *Journal of Volcanology and Geothermal Research*, 414:107245.

Del Gaudio, C., Aquino, I., Ricciardi, G., Ricco, C., and Scandone, R. (2010). Unrest episodes at campi flegrei: A reconstruction of vertical ground movements during 1905–2009. *Journal of Volcanology and Geothermal Research*, 195(1):48–56.

Edmonds, M. and Woods, A. W. (2018). Exsolved volatiles in magma reservoirs. *Journal of Volcanology and Geothermal Research*, 368:13–30.

Eshelby, J. D. (1957). The determination of the elastic field of an ellipsoidal inclusion, and related problems. *Proceedings of the royal society of London. Series A. Mathematical and physical sciences*, 241(1226):376–396.

Fung, Y.-c. and Drucker, D. (1966). Foundation of solid mechanics. *Journal of Applied Mechanics*, 33(1):238.

Fyfe, W. S. (2012). *Fluids in the earth's crust: Their significance in metamorphic, tectonic and chemical transport process*, volume 1. Elsevier.

Galderisi, A., Bonadonna, C., Delmonaco, G., Ferrara, F. F., Menoni, S., Ceudech, A., Biass, S., Frischknecht, C., Manzella, I., Minucci, G., et al. (2013). Vulnerability assessment and risk mitigation: the case of vulcano island, italy. *Landslide Science and Practice: Volume 7: Social and Economic Impact and Policies*, pages 55–64.

Gradshteyn, I. and Ryzhik, I. (2014). *Table of Integrals, Series, and Products*. Academic Press.

Gratier, J.-P., Dysthe, D., and Renard, F. (2012). The role of pressure solution creep in the ductility of the earth's upper crust. *Advances in Geophysics*, in press.

Inguaggiato, S., Vita, F., Diliberto, I. S., Mazot, A., Calderone, L., Mastrolia, A., and Corrao, M. (2022). The extensive parameters as a tool to monitoring the volcanic activity: The case study of vulcano island (italy). *Remote Sensing*, 14(5).

Karato, S.-i., Karki, B., and Park, J. (2020). Deep mantle melting, global water circulation and its implications for the stability of the ocean mass. *Progress in Earth and Planetary Science*, 7:1–25.

Kobayashi, T., Morishita, Y., and Munekane, H. (2018). First detection of precursory ground inflation of a small phreatic eruption by insar. *Earth and Planetary Science Letters*, 491:244–254.

Manga, M. and Wang, C.-Y. (2015). 4.12 - earthquake hydrology. In Schubert, G., editor, *Treatise on Geophysics (Second Edition)*, pages 305–328. Elsevier, Oxford, second edition edition.

Mantiloni, L., Nespoli, M., Belardinelli, M. E., and Bonafede, M. (2020). Deformation and stress in hydrothermal regions: The case of a disk-shaped inclusion in a half-space. *Journal of Volcanology and Geothermal Research*, 403:107011.

Markovich, K. H., Manning, A. H., Condon, L. E., and McIntosh, J. C. (2019). Mountain-block recharge: A review of current understanding. *Water Resources Research*, 55(11):8278–8304.

McTigue, D. F. (1986). Thermoelastic response of fluid-saturated porous rock. *Journal of Geophysical Research: Solid Earth*, 91(B9):9533–9542.

Mogi, K. (1958). Relations between the eruptions of various volcanoes and the deformation of the ground surfaces around them: Bulletin of the earthquake research institute, v. 36.

Nespoli, M., Belardinelli, M. E., and Bonafede, M. (2021). Stress and deformation induced in layered media by cylindrical thermo-poro-elastic sources: An application to campi flegrei (italy). *Journal of Volcanology and Geothermal Research*, 415:107269.

Nespoli, M., Belardinelli, M. E., and Bonafede, M. (2023a). Thermo-poro-viscoelastic response of a disc-shaped inclusion. *Geophysical Journal International*, 235(1):135–149.

Nespoli, M., Belardinelli, M. E., Calò, M., Tramelli, A., and Bonafede, M. (2022). Deformation induced by distributions of single forces in a layered half-space: Efgrn/efcmp. *Computers Geosciences*, 164:105136.

Nespoli, M., Tramelli, A., Belardinelli, M. E., and Bonafede, M. (2023b). The effects of hot and pressurized fluid flow across a brittle layer on the recent seismicity and deformation in the campi flegrei caldera (italy). *Journal of Volcanology and Geothermal Research*, 443:107930.

Nespoli, M., Yu, H., Rinaldi, A. P., Harrington, R., Belardinelli, M. E., Martinelli, G., and Piombo, A. (2025). Applications and future developments of the (thermo-) poro-elastic theory in geophysics. *Earth-Science Reviews*, 260:104996.

Nikkhoo, M. and Rivalta, E. (2022). Analytical solutions for gravity changes caused by triaxial volumetric sources. *Geophysical Research Letters*, 49(8):e2021GL095442. e2021GL095442 2021GL095442.

Piombo, A., Martinelli, G., and Dragoni, M. (2005). Post-seismic fluid flow and coulomb stress changes in a poroelastic medium. *Geophysical Journal International*, 162(2):507–515.

Rice, J. R. and Cleary, M. P. (1976). Some basic stress diffusion solutions for fluid-saturated elastic porous media with compressible constituents. *Reviews of Geophysics*, 14(2):227–241.

Rinaldi, A., Todesco, M., and Bonafede, M. (2010). Hydrothermal instability and ground displacement at the campi flegrei caldera. *Physics of the Earth and Planetary Interiors*, 178(3):155–161.

Schoell, M. (1988). Multiple origins of methane in the earth. *Chemical geology*, 71(1-3):1–10.

Segall, P. (1992). Induced stresses due to fluid extraction from axisymmetric reservoirs. *pure and applied geophysics*, 139(3):535–560.

Segall, P. and Fitzgerald, S. D. (1998). A note on induced stress changes in hydrocarbon and geothermal reservoirs. *Tectonophysics*, 289(1-3):117–128.

Selva, J., Bonadonna, C., Branca, S., De Astis, G., Gambino, S., Paonita, A., Pistolesi, M., Ricci, T., Sulpizio, R., Tibaldi, A., and Ricciardi, A. (2020). Multiple hazards and paths to eruptions: A review of the volcanic system of vulcano (aeolian islands, italy). *Earth-Science Reviews*, 207:103186.

Stissi, S. C., Currenti, G., Cannavò, F., and Napoli, R. (2023). Evidence of poro-elastic inflation at the onset of the 2021 vulcano island (italy) unrest. *Frontiers in Earth Science*, Volume 11 - 2023.

Todesco, M. (2021). Caldera's breathing: poroelastic ground deformation at campi flegrei (italy). *Frontiers in Earth Science*, 9:702665.

Tramelli, A., Godano, C., Ricciolino, P., Giudicepietro, F., Caliro, S., Orazi, M., De Martino, P., and Chiodini, G. (2021). Statistics of seismicity to investigate the campi flegrei caldera unrest. *Scientific reports*, 11(1):7211.

Trasatti, E., Bonafede, M., Ferrari, C., Giunchi, C., and Berrino, G. (2011). On deformation sources in volcanic areas: Modeling the campi flegrei (italy) 1982–84 unrest. *Earth and Planetary Science Letters*, 306(3):175–185.

Walter, M. J. (2021). Water transport to the core–mantle boundary. *National Science Review*, 8(4):nwab007.

Wang, C.-Y. and Manga, M. (2021). *Water and earthquakes*. Springer Nature.